CHEMILUMINESCENCE AND IGNITION DELAY TIME MEASUREMENTS OF C_9H_{20} OXIDATION IN O_2-Ar BEHIND REFLECTED SHOCK WAVES

A Thesis

by

BRANDON MICHAEL ROTAVERA

Submitted to the Office of Graduate Studies of
Texas A&M University
in partial fulfillment of the requirements for the degree of

MASTER OF SCIENCE

December 2009

Major Subject: Mechanical Engineering

CHEMILUMINESCENCE AND IGNITION DELAY TIME MEASUREMENTS OF C_9H_{20} OXIDATION IN O_2-Ar BEHIND REFLECTED SHOCK WAVES

A Thesis

by

BRANDON MICHAEL ROTAVERA

Submitted to the Office of Graduate Studies of
Texas A&M University
in partial fulfillment of the requirements for the degree of

MASTER OF SCIENCE

Approved by:

Chair of Committee,	Eric L. Petersen
Committee Members,	Kalyan Annamalai
	William H. Marlow
	Bing Guo
Head of Department,	Dennis O'Neal

December 2009

Major Subject: Mechanical Engineering

ABSTRACT

Chemiluminescence and Ignition Delay Time Measurements of C_9H_{20} Oxidation in O_2-Ar behind Reflected Shock Waves. (December 2009)

Brandon Michael Rotavera, B.S., University of Central Florida

Chair of Advisory Committee: Dr. Eric L. Petersen

Stemming from a continuing demand for fuel surrogates, composed of only a few species, combustion of high-molecular-weight hydrocarbons ($>C_5$) is of scientific interest due to their abundance in petroleum-based fuels, which contain hundreds of different hydrocarbon species, used for military, aviation, and transportation applications. Fuel surrogate development involves the use of a few hydrocarbon species to replicate the physical, chemical, combustion, and ignition properties of multi-component petroleum-based fuels, enabling fundamental studies to be performed in a more controlled manner. Of particular interest are straight-chained, saturated hydrocarbons (n-alkanes) due to the high concentration of these species in diesel and jet fuels. Prior to integrating a particular hydrocarbon into a surrogate fuel formulation, its individual properties are to be precisely known. n-Nonane (n-C_9H_{20}) is found in diesel and aviation fuels, and its combustion properties have received only minimal consideration.

The present work involves first measurements of n-C_9H_{20} oxidation in oxygen (O_2) and argon (Ar), which were performed under dilute conditions at three levels of equivalence ratio (ϕ = 0.5, 1.0, and 2.0) and fixed pressure near 1.5 atm using a shock tube. Utilizing shock waves, high-temperature, fixed-pressure conditions are created within which the fuel reacts, where temperature and pressure are calculated using 1D shock theory and measurement of shock velocity. Of interest were measurements of ignition times and species time-histories of the hydroxyl (OH*) radical intermediate.

A salient pre-ignition feature was observed in fuel-lean, stoichiometric, and fuel-rich OH* species profiles. The feature at each equivalence ratio was observed above 1400 K with the time-of-initiation (post reflected-shock) showing dependence on ϕ as the initiation time shortened with increasing ϕ. Relative percentage calculations reveal that the fuel-rich condition produces the largest quantity of pre-ignition OH*. Ignition delay time measurements and corresponding activation energy calculations show that the ϕ = 1.0 mixture was the most reactive, while the ϕ = 0.5 condition was least reactive.

NOMENCLATURE

Abbreviations	*Definition*
FT	Fischer-Tropsch
FWHM	Full-Width Half-Maximum
GTL	Gas-to-Liquid
HC	Hydrocarbon
H/C	Hydrogen-to-Carbon Ratio
ISW	Incident Shock Wave
L/D	Length-to-Diameter Ratio
LVP	Low Vapor Pressure
NTC	Negative Temperature Coefficient
RSW	Reflected Shock Wave
STP	(101325 Pa, 295 K)
UHCs	Unburned Hydrocarbons
UV	Ultraviolet
VIS	Visible

Symbols	*Definition*	*Units*
A	Arrhenius Pre-Exponential, Frequency Factor	
a	Local Acoustic Speed	m /s
c	Speed of Light (in Vacuum)	m /s ($3 \cdot 10^8$ m /s)
c_P	Constant-Pressure Specific Heat	J /kg · K, kJ /kg · K
c_V	Constant-Volume Specific Heat	J /kg · K, kJ /kg · K
d	Diameter	m, cm, mm, μm
h	Planck Constant	J·s ($6.626 \cdot 10^{-34}$ J·s)
M	Mach Number	(Dimensionless)
M_W	Molecular Weight	kg /kmol
n	Arrhenius Non-Linearity Factor	(Dimensionless)
P	Pressure	torr, Pa, atm
R_u	Universal Gas Constant	J /mol · K, kJ /kmol · K
s	Entropy	J /kg · K, kJ /kg · K
T	Temperature	K
$\mathcal{V}$	Velocity	m /s, μm /ms

Greek Symbols

Δ	Change (Final – Initial)	(Dimensionless)
γ	Specific Heat Ratio (c_P /c_V)	(Dimensionless)
λ	Wavelength	nm
ν	Frequency	s^{-1}
ρ	Density	kg /m^3
$\tau_{Ignition}$	Ignition Delay Time	μs

Subscripts	*Definition*
1	Initial State within Low-Pressure Section of Shock Tube
2	Conditions within Incident Shock Wave
3	Conditions within Expansion Fan
4	Initial State within High-Pressure Section of Shock Tube
5	Conditions behind Reflected Shock Wave
∞	Free-Stream Condition
R	Reflected

TABLE OF CONTENTS

Page

LIST OF FIGURES

Page

Page

Page

LIST OF TABLES

1. INTRODUCTION: THE ROLE OF COMBUSTION SCIENCE IN AN ALTERNATIVE ENERGY ENVIRONMENT

1.1 Motivation

With a replacement for energy production from hydrocarbons well into the future, there remains strong interest in arriving at a temporary solution to mitigate some of the main concerns involved with hydrocarbon combustion: depleting availability of natural resources, pollutant emissions, and fuel efficiency. Given the continuing interest in alternative transportation, power generation, military and aviation fuels, most of which possess a low vapor pressure, an approach to examine the phenomenological combustion behavior of these fuels (reaction pathways, product-species formation, ignition delay, autoignition properties, flame speeds, soot production) to assess their role as replacements for current petroleum-based fuels is needed. Reproducing complex blends of hydrocarbons in laboratory and computational environments can be cumbersome, so replacing them with surrogate fuel blends containing only a few components is attractive. Surrogate fuels consist of a mixture of several species formulated to reproduce the combustion characteristics of the petroleum-based fuel it is intended to model. Each of the constituent species has individual adiabatic flame temperatures, minimum ignition energies, sooting tendencies, product yields, and ignition delay times. As such, there is an ongoing need to examine the cumulative impact of the mixture of several fuels and, more specifically, identify surrogate fuels suitable for the aforementioned applications. Understanding the chemical behavior of individual hydrocarbon species ultimately would benefit the engineering of new fuels that are tailored to specific applications.

Low-vapor-pressure (LVP) fuels are implemented in aviation, military, and transportation applications due to their transportability and high energy density among other reasons. As a result of the wide applicability of fuels with low vapor pressure, experiments that cover a large range of conditions are required to examine such fuels under application-specific pressures and temperatures that span from ~ 10 atm and ~ 800 K (compression-ignition engines) to ~ 50 atm and ~ 1000 K (gas turbine engines) with other applications reaching even higher temperatures and pressures.

Shock tubes provide repeatable and controllable conditions of temperature and pressure using shock waves and gas dynamics. A test region is created by the reflection of a shock wave incident on an endwall, appended to which are numerous possible diagnostics for measurement of pressure, shock velocity, optical spectroscopy, and laser-based diagnostics such as scattering and absorption.

This thesis follows the style of *AIAA Journal*

Shock tubes are ideally suited for fuels with high vapor pressure as these species enter the gas-phase readily under standard conditions of temperature and pressure, however are also well-suited for studying fuels of low vapor pressure with additional precaution. As a result, the shock tube as an experimental device is capable of reaching experimental conditions that are of interest to each of the abovementioned application and conditions.

1.2 Role of surrogate fuels

Transportation and aviation fuels are petroleum based and are comprised organically of hundreds of hydrocarbon species, ranging in class (alkanes, alkenes, alkynes, aromatics, napthenes), molecular size (C_3 – C_{30}), and molecular structure. A surrogate fuel, by definition, is a mixture of hydrocarbons classified by *hydrocarbon family proportioning* or an *averaged molecular weight* (H/C ratio) formulated to represent the physical, chemical, and reactivity properties of the petroleum-based counterpart. The count of constituent species in surrogate fuels can range from one to ten or more, where the utility of a surrogate fuel, in addition to addressing other practical concerns, is the ability to model the ignition and combustion of these fuels in simulated engines using chemical kinetic mechanisms.

A depleting supply of petroleum alone undoubtedly justifies the need for alternative fuel research and development, however the large-scale use of alternative fuel blends has several important issues to contend with if it is to become a replacement for petroleum-based hydrocarbons, namely transportability, economic feasibility, and minimal impact on food supplies as many of the surrogate fuels under development currently utilize ethanol from corn, sugar cane, among others. Principally, aside from the abovementioned issues that any replacement, and in the limit a surrogate, fuel must satisfy, it must fundamentally be able to replicate the ignition and combustion properties that modern internal combustion and gas turbine engines require for generation of power to the respective device: automobile, aircraft, and power generation turbines. One popular category of alternative or replacement fuel is synthetic fuels.

There are technological challenges to also overcome in the production of synthetic fuels. In military /aviation applications, the replacement synthetic fuel must satisfy a wide range of criteria. Physical properties (fluidity, density, lubricity, viscosity) and chemical properties (heat of combustion, energy content, thermal stability, flame temperature, flame speed, corrosiveness) maintain an interplay that is difficult to balance. One example is the requirement of a specific freezing point for high-altitude flight. Changing the fuel composition to meet required product yields (CO_2, H_2O, NO_x, UHCs) alters the freezing point of the fuel which has drastic implications on it usability in military /aviation applications.[1] A survey of surrogate fuel blend compositions, physical property requirements of jet fuels, heats of combustion, and compositional variation of jet fuels is given by Edwards and Maurice.[2] Challenges specific to gas turbine

engine combustion have been described by Gupta and Lilley[3], providing insight to NO_x-related environmental issues, emissions, alternative fuels and other pertinent issues related to combustion. Ghassemi et. al. describe similar issues, yet those related to synthetic fuel use in transportation vehicles.[4] Longwell discusses heats of reaction of common components contained in synthetic fuels, conversion process efficiencies to create synthetic fuels, and an outline of the refining process.[5]

The Fischer-Tropsch (FT) synthetic fuel technique utilizes gas-to-liquid (GTL) conversion of a feedstock (biomass, coal, natural gas) into carbon monoxide (CO) and hydrogen (H_2) to generate liquid high-energy-density fuels that can be further refined and tailored to meet requirements for product yields, ignition characteristics, and other fuel requirements, yet the fundamental issue of experimentation still exists with such fuels. A comprehensive look at the FT process, its applications, history, and trends is given by Schulz.[6] Surveys and experimental examinations into aviation fuels[7–9], synthetically produced jet fuels[10], and automotive synthetics[11–14] are abundant in the literature.

Production and utilization of synthetic fuels have received attention for decades, and with a viable solution still to be attained much work is needed on a number of fronts to meet the challenge of implementing full-scale synthetic fuel use. Although experimentation and modeling of synthetic and surrogate fuels has been ongoing for over a decade[15–25], key issues remain largely unanswered. Addressing such fuel-related issues from a chemistry standpoint necessitates experimental testing and development of new fuels and surrogate models.

The present work involves shock-tube combustion experiments on a single, heavy hydrocarbon (n-nonane, C_9H_{20}) which is a constituent in both aviation and transportation fuels with the ultimate aim of integrating these and additional experimental results into a chemical kinetics model from which a surrogate fuel can be developed and applied to applications such as jet engines and internal combustion engines.

2. BACKGROUND

Studies in chemistry, spectroscopy, and physics require precision and accuracy over experimental pressure and temperature conditions to which a given test variable is subjected, ranging from low, sub-atmospheric pressures to elevated pressures of 100 atm and above and with temperatures exceeding several thousand Kelvins. Shock tubes are experimental devices in which wide-ranging thermodynamic conditions can be covered with high precision and accuracy, and with a high degree of chemical purity. This section serves first to provide a physical interpretation of the shock-tube process as it applies to combustion studies, a description given without mathematics to provide a purely physical expression of the overall process from shock-wave initiation, propagation and reflection, to combustion of a reactive mixture. Not covered are the processes of shock wave formation (a coalescence of acoustic waves as a result of an accelerating medium) and expansion wave formation (the physical consequence of the propagation of a compression wave).

Fundamental concepts of acoustic (sound) speed and Mach number are discussed using thermodynamic concepts for purpose of review. The main components of a shock tube are outlined and detailed, after which a qualitative description of the physics involved in a given shock-tube experiment are presented with supporting figures. The shock tube utilized in the present study invokes one-dimensional (1D) shock equations to determine the test conditions in a given experiment, the *Rankine-Hugoniot equations*. The equations are presented without mathematical formalism, and a historical reference to their development is given, along with some underlying assumptions of their development and implementation as to yielding the thermodynamic conditions (temperature and pressure) behind shock waves.

Lastly, the physics involved in the two main focuses of the present work, OH* species time-histories and ignition delay times, are discussed fundamentally. Supporting shock-tube literature focusing on these aspects and their relation to practical systems is also provided.

2.1 Shock wave and shock-tube physics

The shock tube is an apparatus first brought to light in 1899[26] and since ca. 1950 has become a well-established, reliable means of measuring a wide range of physical phenomena of interest to physics, chemistry, astrophysics, and astronomy.[27,28] The primary attributes that have made the device both useful and versatile are the controllable, repeatable, and wide-ranging conditions of both pressure and temperature that are available. Using thermodynamics and gas dynamics, experimental conditions can be well-predicted to a high degree of accuracy for a given set of initial conditions. The shock tube consists of a long tube of given material (stainless steel, glass) and dimensions (circular, square) which is separated into two main sections: a *driver* and *driven* section or high- and low-pressure sections, respectively. The separation is achieved through the use of a diaphragm of plastic or metallic material and the bursting of the diaphragm resulting from an exerted pressure differential yields the propagation of a strong compression wave (shock wave) in the direction of the low pressure driven section.

A *shock wave* by definition is a strong compression wave which, upon interaction with a given media, induces near instantaneous step changes in thermodynamic conditions (temperature, pressure, entropy). The process is irreversible from significant increases in entropy and adiabatic as there is insufficient time for heat transfer to occur appreciably and due to the diminutive wave area (shock thickness ~ *mean free-molecular path*). The medium with which the shock wave interacts herein will be one in a gaseous state. In a physical sense, the interaction of a shock wave with its medium of propagation can be described as a series of rapid molecular collisions that occur on timescales too small for the surrounding media to respond. The speed at which a given media, of any phase, can respond to a change in surrounding conditions is described by a characteristic sound speed a:

$$a = \left(\frac{dP}{d\rho}\right)_s^{0.5}$$

The sound speed can be described physically as the rate at which particles (molecules or atoms) can respond to upstream (oncoming) disturbances.

Invoking Gibbs' relations, assuming the process is one-dimensional, and the gaseous medium through which a compression wave travels behaves as an ideal-gas, equations of momentum and mass conservation reveal:

$$\left(\frac{dP}{d\rho}\right)_s^{0.5} = \left(\frac{P\gamma}{\rho}\right)^{0.5}$$

or, for an ideal gas

$$\left(\frac{dP}{d\rho}\right)_s^{0.5} = (\gamma RT)^{0.5}$$

The strength of a shock wave is defined by a Mach number, defined as the ratio of the speed of an object (shock wave) relative to the characteristic sound speed of the medium through which the object travels:

$$M = \frac{\mathcal{V}}{a}$$

or,

$$M = \frac{\mathcal{V}_{shock\ wave}}{a_{test\ gas}} = \frac{\mathcal{V}_{shock\ wave}}{(\gamma RT)^{0.5}}$$

A *shock tube* is an apparatus which employs the generation and control of normal (planar) shock waves to create desired conditions of temperature and pressure using physical laws of fluid mechanics and gas dynamics. The simple shock tube consists of two primary sections, a driver (high-pressure) section and driven (low-pressure) section, which are separated by a diaphragm station (Fig. 1). On each side of the diaphragm resides a gaseous mixture, usually differing in composition. Contained within the driver section is a single species or mixture of species that is typically non-reactive and of low molecular weight. In the driven section of the shock tube the reactive mixture is present. The reactive mixture may have several constituents which each belong to one of three categories: (1) fuel, (2) oxidizer, or (3) inert/buffer gas. In combustion work, the fuel and oxidizer are the focus of the given experiment, and the inert/buffer gas serves to control (absorb) the release of energy from the reaction and/or replicate a fuel mixture which would be used in a practical engine (i.e. a fuel-air mixture where the fuel accounts for ~ 3% by volume of the mixture).

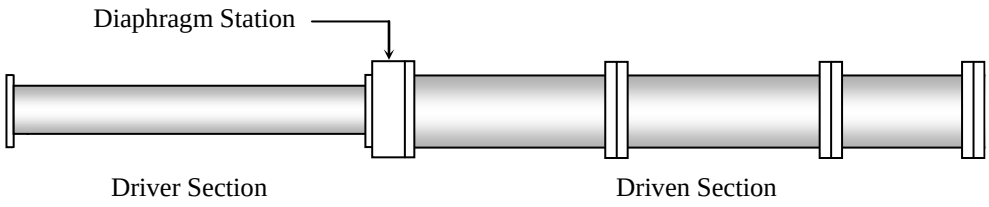

Fig. 1. Primary sections and diaphragm station of a simple shock tube.

The diaphragm station holds in place a diaphragm of given material (aluminum, stainless steel, lexan) and thickness which, for a given combination of the two parameters, possesses a unique and highly repeatable breaking pressure. The (breaking) pressure required for rupturing is surpassed by applying a large pressure differential, on the order of tens to hundreds, across the diaphragm. This implies that the pressure of the non-reactive driver gas is tens or hundreds of times greater than that of the reactive mixture.

The driver section is filled at a constant rate with a gas until a critical pressure differential is reached, after which the diaphragm ruptures resulting in a substantial and instantaneous drop in driver-section pressure as the high-pressure gas is exposed to the low-pressure section which resided on the opposite side of the diaphragm (Fig. 2). Resultingly the pressure energy translates into momentum as, thermodynamically, the system changes from a closed-system to an open-system and the (non-reactive) driver-gas rushes through the diaphragm station into the low-pressure (reactive) test gas present in the driven section. The impetuous nature of the entry causes a sudden impartation of the kinetic energy held by the higher pressure gas flow which then instantaneously elevates the thermodynamic state of the initially stagnant driven gas.

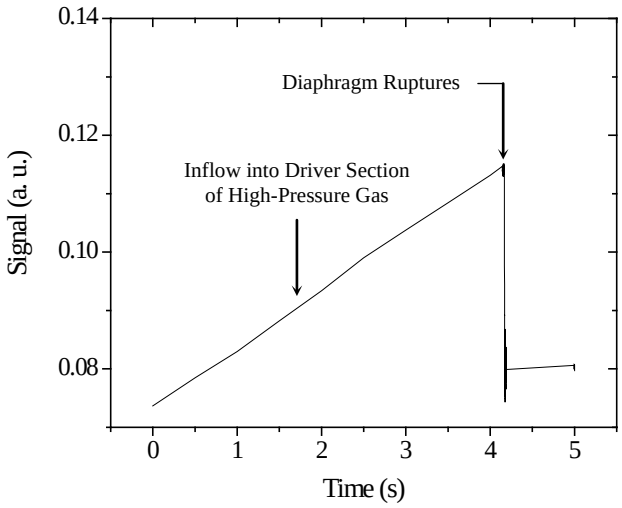

Fig. 2. Driver-pressure time history of 254 μm-thick lexan diaphragm. Pressure ratio across diaphragm → 4140 torr /80 torr ~ 50.

In effect, the velocity of the driver gas is high enough such that the gas molecules (or atoms) existing on the low-pressure side of the shock tube are unable to respond to the rapid change in conditions. The low-pressure gas is unable to give way to the entering higher pressure gas and as a result, a collision front propagates from the plane-of-exit from the diaphragm station through each cross-section of the shock tube.

Shock strength, measured by its Mach number, and test gas composition dictate the degree of elevation of temperature, pressure, density, and thermophysical properties. The propagation of the shock wave itself occurs through a rapid series of molecular collisions. It is these collisions which result in the elevated thermodynamic state as the translational energy converts, partially, into molecular kinetic energy (i.e. an increase in temperature).

After a period of time, the shock wave traverses the length of the tube and reaches the solid boundary at the end of the tube termed the *endwall*. In precisely the same manner, yet to a different degree, the reactive mixture then experiences another shock wave. The second shock wave, termed the reflected shock wave (RSW), is of lesser strength than the initial (*incident*) shock wave and is the product of the reflection of the incident shock wave (ISW) off of the solid boundary (endwall). The result of the interaction with the reflected-shock is the creation region containing stagnant, reactive gas and a further elevation in thermodynamic state–the *test region*. Upon interaction with the reflected shock wave, translational (kinetic) energy that is transferred to the quiescent reactive mixture through the collisions is converted into thermal energy, and the reactive mixture in the test region is nearly instantaneously brought to the reaction temperature and pressure. The timescale on which this (collision) process occurs reveals the primary advantage to using shock waves in kinetics and chemical physics–the reactants are heated on the order of microseconds (μs), avoiding slow heating of the reactants. Considering the converse, where reactants are heated on timescales longer than those of chemical processes (timescales > μs), issues such as thermal cracking of the fuel, slow combustion, temperature uncertainty from heat transfer, and other phenomena complicate the analysis of the reaction chemistry are avoided.

During chemical reaction, the process of redistribution of electrons from the scission of existing and formation of new chemical bonds provides abundant sources of extractable information about the reactive mixture such as pressure rise, light emission, flame temperature, and sooting tendency, and from each of these phenomena further analysis can reveal the physics of fundamental processes including but not limited to ignition delay time, radical species time-histories, activation energy, and chemical reaction rates and pathways. Figures 3.A, 3.B, and 3.C show, pictorially, the process taken to rupture the diaphragm in a simple shock-tube (3.A), the formation of the incident shock wave (3.B), and the formation of the reflected shock wave (RSW) behind which conditions of temperature and pressure are created for experimental initial conditions (3.C). Details on shock wave theory, shock-tube design, boundary layer effects, and uncertainties in shock-tube experiments have been covered to a considerable degree.[27–35]

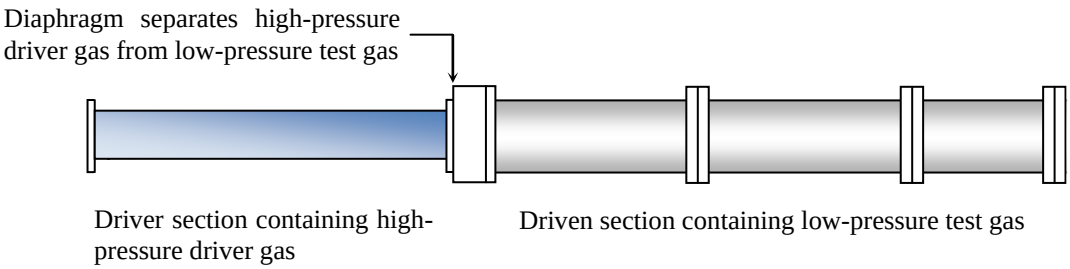

Fig. 3.A. The shock-tube driver section is filled at a constant rate with a high-pressure gas. Helium (M_W = 4 kg /kmol, γ = 1.67) is utilized in the present experiment as driver gas. The driver section of the shock tube is filled to yield pressure set by the diaphragm thickness and material. Diaphragms are specifically chosen to produced desired experimental conditions. For the experiments conducted herein, lexan diaphragms of 254 μm thickness and yield strength of 35 psig were used to produce ~ 1.5 atm in the test region of the shock tube.

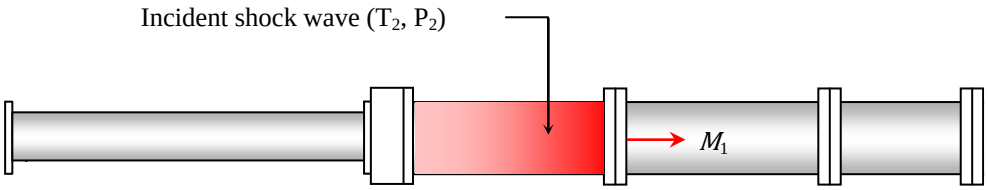

Fig. 3.B. The diaphragm is ruptured after a diaphragm-specific critical pressure is surpassed and a shock wave of Mach number M_1 is formed in and propagates through the low-pressure reactive mixture. Diaphragm-bursting transfers high-pressure gas, initially separated from the low-pressure region, into high-velocity gas exiting the driver section. The test-gas response time (acoustic speed, a_1) is insufficient to react to the change in conditions and collide with the entering, high-velocity gas molecules. Resultingly, a shock wave forms and the passage of the shock wave heats and compresses the test gas to State 2. As the shock wave traverses the tube, attenuation from interaction with the shock tube walls and corresponding viscous force decreases its velocity with increasing distance as it approaches the endwall.

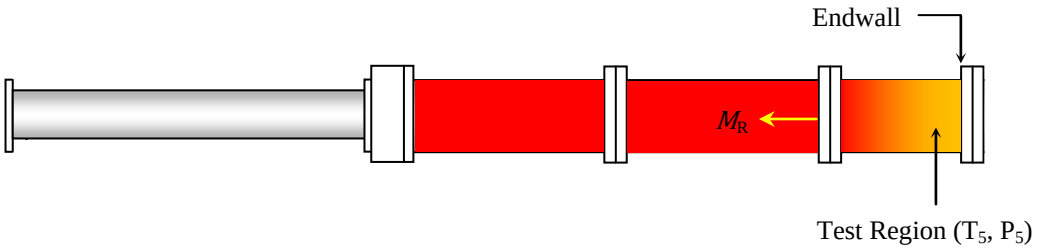

Fig. 3.C. The test region of the shock-tube is formed as a result of the reflection of the incident shock wave off of the endwall. Since the gas near the endwall experiences two shock waves, $T_5 > T_2$ and $P_5 > P_2$. The reflected shock wave passes back through the shock tube where it interacts with expansion waves of lesser strength. Shock waves uniformly bring the test region to elevated temperature and pressure near instantaneously, thus (at short times) heat transfer effects to the gas can be neglected and the temperature of the gas is taken to be that created by the shock wave at the instant it forms.

Driver gas is selected to serve the experimental objectives, namely the length of the time available in the test region of the shock tube required in order to observe the phenomena of interest. Several parameters affect the length of the time available in the test region, specifically shock-tube geometry (length) and physical properties of the gases contained within it. The physical properties which impact the test time are the specific heat ratio γ and molecular weight M_W of the driver gas species. From the definition of sound speed, species with lower γ or higher M_W possess a slower sound speed. This translates to a later time-of-arrival of either the expansion fan, a series of low-pressure waves formed during the diaphragm rupture which initially travel in the opposite direction of the ISW, or the arrival of the contact surface, a less energetic front which separates the driver gas from the driven gas, in meeting the reflected shock wave. Common driver gases are shown in Table 1 with respective thermodynamic properties. Other species may be used to suit specific needs (i.e. combustion driver), as well as mixtures of varying molar proportions of each. Inert gases aside from Helium are not often used due to their rarity and corresponding high cost.

Table 1. Common species used for driver gas.

Species	γ (293 K)	M_W (kg /kmol)
H_2	1.41	2
He	1.67	4
Ne	1.67	20
N_2	1.40	28
O_2	1.40	32
Ar	1.67	40
CO_2	1.29	44
Xe	1.67	131

Geometric implications on test time arise mainly from the respective lengths of the driver and driven section. For contact surface arrival at the test region in an exceedingly long driven section, since the ISW travels significantly faster than the low-energy front, the RSW (formed from the interaction of the ISW with the solid boundary) is allowed more time to travel back toward the diaphragm station from the endwall before meeting the front. Considering now both elongated driver and driven sections and the impact on rarefaction (expansion) waves, an even longer time is required to traverse both the elongated driver and driven sections, again allowing prolonged time for the RSW to pass through the once-shocked reactive mixture.

A limit also exists in consideration of geometric proportioning of each section of the shock tube. The driving force for shock wave propagation in a tube is the expansion of a high-pressure gas. In a shock tube of (hypothetical) infinite length the advantage may be seen that with infinite length comes infinite test time (assuming the ISW is afforded reflection through some means), however finite expansion is present with or without infinite length. Thus, a shock tube of infinite length would not be effective as the driving force for shock propagation would diminish at a given distance from the diaphragm station.

2.2 Rankine-Hugoniot equations

In order to predict the thermodynamic conditions within the shock tube, the waves are assumed planar which is a valid approximation past a distance of several diameters of length after the diaphragm station. From the planar-wave assumption, a one-dimensional (1D) simplification of the equations describing shock-gas interaction is employed: the *Rankine-Hugoniot equations*. From the solution of these equations, one can determine with high accuracy the conditions of temperature and pressure to which the test variable is subjected. These equations require two input variables to reach a characteristic solution, a Mach number and a specific heat ratio. Detailed and highly comprehensive work is performed by M. D. Salas[36] on the history of shock wave theory, dealing with the works of William John Macquorn *Rankine* and Pierre Henri *Hugoniot*.[37–38]

Embedded assumptions include propagation of the shock through an ideal gas with variable specific heats (c_P and c_V). The shock process is considered adiabatic as there is both insufficient time and insufficient area for appreciable quantities of heat to transfer. In terms of incident-shock Mach number M_1, pressure and temperature conditions behind the reflected shock wave (P_5 and T_5, respectively) relative to initial conditions are given:

$$\frac{P_5}{P_1} = \left\{\frac{2\gamma M_1^2 - (\gamma - 1)}{\gamma + 1}\right\}\left\{\frac{(3\gamma - 1)M_1^2 - 2(\gamma - 1)}{(\gamma - 1)M_1^2 + 2}\right\}$$

$$\frac{T_5}{T_1} = \frac{\{2(\gamma - 1)M_1^2 + (3 - \gamma)\}\{(3\gamma - 1)M_1^2 - 2(\gamma - 1)\}}{(\gamma + 1)^2 M_1^2}$$

As observed from the above 1D shock relations, the thermodynamic conditions within the shock tube are dictated strictly by the specific heat ratio γ and the Mach number M. *Bath gases* can range widely in composition to match experimental goals. Table 2 shows several solutions for the Rankine-Hugoniot shock relations for commonly used bath gases and mixtures using helium as a driver gas. The term bath gas implies a nonreactive mixture, differing from test gas which can contain several percent by volume of fuel.

Table 2. Variance of thermodynamic condition for changing bath gas composition using helium as driver gas. Lower acoustic speeds imply that the fluid has a lower response time to react to oncoming pressure perturbations resulting in a larger Mach number (for fixed-velocity shock) and correspondingly larger step-changes in both pressure and temperature.

Species	γ_1	γ_5	P_5/P_1	T_5/T_1	$M_{\text{incident shock}}$	a_1 (m/s)	a_5 (m/s)
Ar	1.67	1.67	29.03	5.15	2.50	320	726
79/21 Ar/O_2	1.58	1.53	30.01	4.53	2.51	318	667
Air	1.40	1.34	24.25	3.00	2.32	345	586
N_2	1.40	1.35	23.05	2.96	2.29	350	593

2.3 Fundamental description and application of measurements

The two principal measurements reported herein, ignition delay times and species time-histories, are obtained from chemiluminescence measurements of excited hydroxyl radicals (OH*). Measurements of rates of change of OH* as well as ignition delay times have utility in the development and refinement of chemical kinetics models and both phenomena have other useful purposes which, along with a description of the underlying physics, are described in the sections below.

2.3.1 OH time-histories using chemiluminescence*

Combustion reactions are driven from the breaking of chemical bonds and formation of new bonds in an array of thousands of elementary reactions for a hydrocarbon fuel. The generation of radicals (short-lived species with unpaired valence electrons) occurs during the initial stages of combustion where such species are created under conditions of high temperature. As a result, energy is absorbed by the radicals, in addition to other species, through collisions with surrounding molecules/atoms (third-body inert species, stable and unstable species). Upon collision, the radicals become excited, increasing in vibrational frequency and reaching a higher electronic state. Shortly after excitation, a relaxation period ensues during which the radical tends toward a lower energy (ground) electronic state and in the process the emission of light (fluorescence) occurs proportional to the product of the Planck constant and frequency of light ($h\nu$). This emission of light, occurring as excited molecules return to their respective ground state, resulting from chemical reaction is *chemiluminescence* (Fig. 4). The oxidation of fuel in the present case, a heavy hydrocarbon (C_9H_{20}) oxidized by molecular oxygen (O_2), involves only two reactants, excluding the nonreactive Ar, yet hundreds of species are formed from ignition and subsequent combustion each of which possess characteristic frequencies of vibration. Two radicals important to combustion chemistry are the hydroxyl (OH) and methylidyne radical (CH), and it is thus of interest to isolate respective characteristic frequencies of excited hydroxyl (OH*) and excited methylidyne (CH*) and measure the time-dependent formation and depletion of these species as a function of temperature, which can provide

insight to the oxidation kinetics. As each of these species vibrate at a characteristic frequency, temporal measurement of species-specific emission of radiation (λ_{OH*}, λ_{CH*}) resulting from relaxation is achieved using a high-sensitivity detector coupled with a filter which excludes wavelengths other than the given wavelength of interest (bandpass filter). Frequencies, related to wavelength according to $\nu = c/\lambda$, emitted during the chemical reaction behind the reflected-shock wave are recorded as time-dependent intensity, yielding species-time histories.

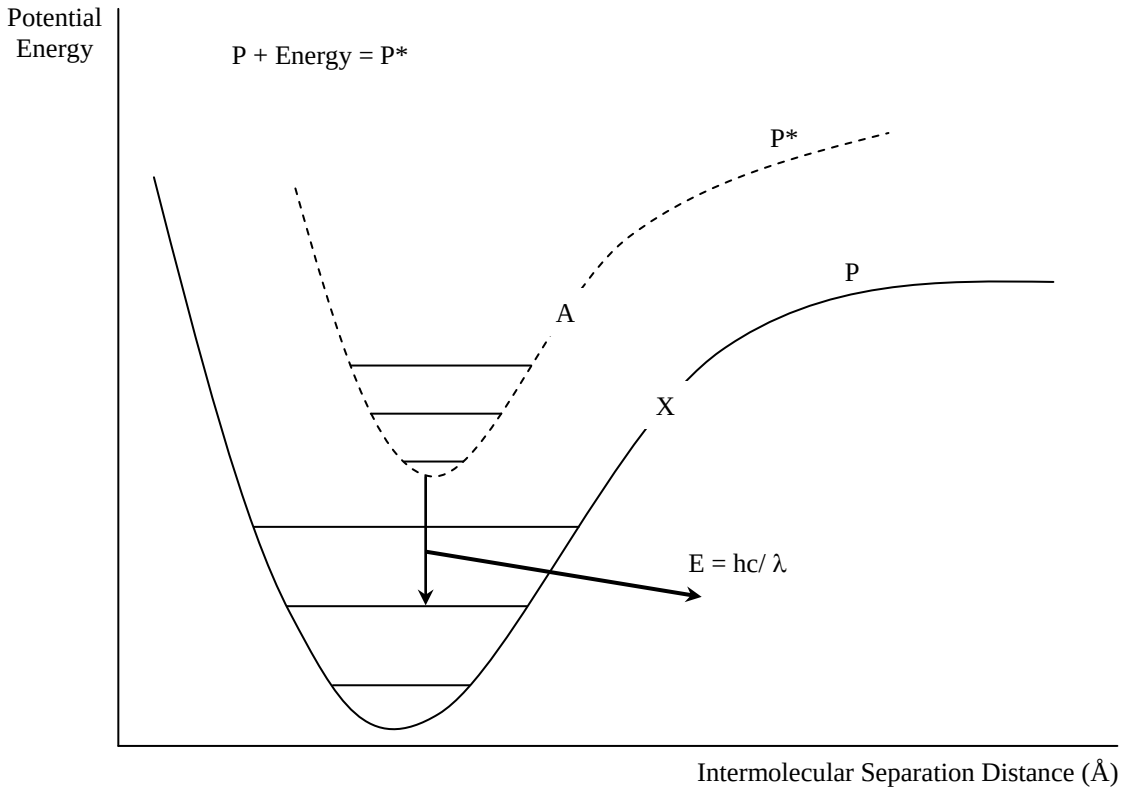

Fig. 4. Morse potential energy curves for excited and equilibrated species as the product (P) of a chemical reaction. Relaxation brings the species from an elevated electronic level (A) to a lower -energy electronic level (X). From the transition of an excited radical (P*) to the ground-state (P), photons of energy $E = hc/\lambda$ are emitted and measured for intensity according to wavelength λ. For OH* and CH*, $\lambda \approx 307.1$ nm and ≈ 430.0 nm, respectively.

Reactions involving OH* and CH* radicals are of well-known significance in hydrocarbon combustion and have received significant experimental focus.[39–55] The hydroxyl radical (OH) in particular has received attention owing to its role in chain propagation reactions, branching reactions in H_2-O_2 systems, and the oxidation of soot and soot precursors.

Xu et al.[39] used transition-state theory to determine expressions for the rate coefficient for H-abstraction and OH-addition kinetics of the OH + CH_2O over a broad temperature range, from 200 K to 3000 K. Each expression showed non-Arrhenius behavior. For H-abstraction, a temperature dependence of n = 2.98 was determined for the temperature range 200 K – 400 K, while for the range 400 K – 3000 K the non-linearity decreased to n = 2.11. The non-linearity of the temperature dependence for the OH-addition expression was characterized to be n = 1.63.

A lean, low-pressure (~ 40 torr) CO-H_2-O_2 flame was employed to investigate the kinetics of CO conversion to CO_2 at low, intermediate, and high temperatures (400 K to 1800 K) using measurements of stable and unstable species in the reaction zone of the flame.[40] Through measurement of the rate coefficient using mass spectrometry, the propagation reaction CO + OH $\rightarrow$ CO_2 + H was shown to be the dominant reaction in the conversion of carbon monoxide to carbon dioxide. The logarithm of the rate coefficient showed non-Arrhenius behavior for temperatures between 600 K – 14500 K, then became linearly dependent on inverse temperature for 400 K – 600 K and 1450 K – 2000 K. Further, from 1000 K to 1800 K, the rate of OH consumption by CO decreases strongly with temperature. From 400 K to 1000 K the decrease was slower. Another study involving the reaction of formation and destruction of OH with CO determined explosion limit parameters in the presence of wet CO combustion.[41]

Flash photolysis using a flashlamp has been utilized to study the reaction of OH with light alkanes, C_2H_6 and C_3H_8, using H_2O as a precursor.[42] Fluorescence by OH provided concentration profiles from which rates of reaction were measured. The study was conducted in pure argon at P = 100 torr and limited to low temperatures (297 K – 800 K). Rate coefficients for reactions with ethane (C_2H_6 + OH $\rightarrow$ Products) showed near-Arrhenius behavior (n = 1.05), while rate coefficients for reactions of hydroxyl with propane (C_3H_8 + OH $\rightarrow$ Products) deviated from inverse-temperature-linearity with n = 1.40. Hydrogen-abstraction channels were also predicted for OH-propane chemistry.

Using a flat-flame burner, the effect of OH concentration on soot formation in premixed atmospheric flames of methane (CH_4), ethane (C_2H_6), propane (C_3H_8), ethylene (C_2H_4), and acetylene (C_2H_2) was quantified over the temperature range 1600 K – 1880 K.[43] Invoking a kinetic model, a correlation dependent on temperature, hydroxyl concentration, and fuel carbon-to-hydrogen ratio was developed. The

correlation was used to investigate the mechanisms by which OH oxidizes soot precursors. Under the theory that soot formation is a competition between production of soot precursors and consumption of these precursors by OH, the authors define an expression for the equivalence ratio using an Arrhenius expression involving rate coefficients of production /consumption of precursors, precursor concentration, fuel concentration, and hydroxyl concentration. Further, it was reported that an increase in OH concentration in the flame results in a decrease in soot concentration.

Laser-induced photolysis (λ = 193.3 nm) applied to $CH_3CHO/N_2O/H_2O$/He mixtures was employed by Taylor et al.[44] over the temperature range 295 K – 900 K in helium at several pressures, although no pressure dependence was observed, hence the study was conducted mostly at a pressure of 740 torr. Time-dependent OH profiles were measured as a function of reactant concentration using laser-induced fluorescence (LIF) measurements from which intensity at λ = 309 nm was recorded using a photomultiplier tube (PMT). From measurements of $\partial[\mathrm{OH}]/\partial t$, two relations expressing rate coefficients for the consumption of acetaldehyde by OH ($CH_3CHO + OH \rightarrow$ Products) were determined according to two temperature regimes. For 295 K – 550 K, the rate coefficient showed a negative temperature dependence, while for 600 K – 900 K a positive dependence on temperature was reported. The authors employed a quantum Rice-Ramsperger-Kassel (QRRK) model to calculated reaction pathways in which it was found that, at low temperature, the dominant reaction pathway was OH-addition followed by methyl (CH_3) elimination, while at higher temperature, H-abstraction from the CH_3 group was prevailing.

Shock tubes have been employed in the study of OH chemistry using high temperatures behind either incident or reflected shock waves[45–53]. Bradley et al., using a shock tube, measured UV absorption by OH from decomposition of hydrogen peroxide (H_2O_2) behind incident shock waves to determine the time rate-of-change of OH concentration. Rate coefficients for OH depletion were measured in the presence of H_2, CO, CF_3H, CH_4, C_2H_6, and C_2H_4 at elevated temperatures (1280 K to 1600 K).[47] The work of Bradley et al. also provides a summary of numerous rates of reaction for important reactions.

OH laser absorption at 306.7 nm behind reflected shock waves has also been utilized to investigate the reaction of CH_3 with OH and the decomposition of methanol (CH_3OH) to produce OH, from which an expression for the overall rate coefficient of CH_3 + OH was formulated from 1081 K – 1426 K.[49] OH radicals were generated by thermal decomposition of tert-butyl hydroperoxide (TBHP), while methyl radicals were generated using azomethane (CH_3-NN-CH_3) or methyl iodide (CH_3I) precursors. A pressure effect was investigated by elevating the reaction pressure to approximately 5 atm, however no significant impact on rate coefficients was noted. Pressure was otherwise maintained near 1.65 atm. The rate coefficient for methyl with hydroxyl was obtained by measurements of OH time histories with those

produced using the GRI 3.0 kinetics model. Vasudevan et al. conducted similar studies on the reaction of OH with formaldehyde (CH_2O).[50] Covering a broad range of high temperatures from 934 K to 1670 K at 1.6 atm, the authors utilized high-temperature data and kinetic theory to extend the temperature range of data available on this reaction. The rate coefficient for OH + CH_2O = HCO + H_2O showed non-Arrhenius behavior (n = 1.63). The reaction OH + CH_2O = HCOOH was also investigated.

Bott and Cohen have performed a series of shock-tube experiments focusing on OH chemistry.[50–53] The reaction of OH with propane was studied under a narrow range of temperature from 1193 K to 1250 K.[50] The temperature range was limited and kept below a certain threshold such that dissociation could be controlled. Strong curvature in the rate coefficient as a function of inverse temperature was noted, indicating non-Arrhenius behavior as has been seen by others. The reaction of hydroxyl with several species (OH + H_2 /+ CH_4 /+ c-C_5H_{10} /+ i-C_4H_{10}) [51], with methyl[52], and with numerous hydrocarbons[54] have also been the subject of experimentation by Bott and Cohen. In each of the works, measured rate coefficients were compared against calculations using transition state theory.

Chemical kinetics calculations coupled with the simultaneous measurement of OH* and CH* in laminar premixed and non-premixed atmospheric CH_4-air flames provided for the determination of equivalence ratio based on the ratio OH*/CH* as these parameters were shown to be monotonically related.[56] Additionally, Panoutsos et. al. provide abundant rate coefficient data for both OH* and CH*. OH and CH concentration profiles were measured in a rich, atmospheric methane-air flame using a flat-flame burner, where radical concentrations were perturbed with an ArF excimer laser.[57] Rates of decay of each species was monitored using fluorescence, the results of which being compared to a kinetics model. A discrepancy in the CH decay rate led to the conclusion by the authors that an improper decay channel had been used in the employed mechanism as the data was over-predicted by the model. Resultingly, the suggestion that an intermediate which impacts the rate of consumption of CH has a higher concentration in rich flames.

2.3.2 Ignition delay times

Shock tubes remove the necessity for physical processes occurring in combustion systems that lead to ignition (fuel injection, mixing) and as such are uniquely apt for fundamental studies on combustion and ignition. The high temperatures behind the reflected shock wave initiate the ignition process by raising the temperature of the gas within a few microseconds. After a period of time, the thermal energy generated by the shock and subsequently absorbed by the atoms and molecules in various energy storage modes (translation, rotation, vibration, electronic) breaks apart certain chemical bonds. Radical species are generated in the process which then cause bond breakage of other species, and the process continues up to

a point where emission and/or pressure have risen rapidly from an abundance of chemical bond breakage and reformation. The period of time over which this process occurs is the *ignition delay time*.

Ignition delay time measurements are utilized as a guide to understanding the reactivity of mixtures under predetermined sets of conditions (temperature, pressure, stoichiometry, dilution level). Routinely, shock-tube measurements of ignition delay times address needs for kinetic model development or experimentation of a specific surrogate fuel blend applicable to jet, internal combustion, or gas turbine engines. Surrogate fuel development has been of considerable interest in recent years due to the needs of both low emissions (NO_x, CO, soot), high fuel efficiency, reducing foreign oil demands, and utilization of fuels produced from natural gas through Fischer-Tropsch synthesis.

Due to concerns over pollution at high elevation, jet fuels have been the subject of research in order to identify a surrogate which can mimic combustion, physical, and chemical properties of petroleum-based fuels, yet with reduced amounts of CO_2, UHC, and soot as products of combustion. Constituents of jet fuel depend on the type (Jet-A, JP-8, JP-10), the refining process, and the source of the petroleum, however the dominant hydrocarbon classes are n- and iso-alkanes, alkenes, aromatics, and napthenes. Dean et al.[58] employed a heated shock tube to study ignition delay times of Jet-A and several blends of benzene (C_6H_6), hexane (C_6H_{14}), and decane ($C_{10}H_{22}$) resulting in an empirical correlation showing a negative dependence on Jet-A concentration. Measurement of Chapman-Jouguet (CJ) detonation velocities as a function of temperature were also reported. Vasu et al. have conducted similar studies using a heated shock tube (required due to the low vapor pressure of heavy hydrocarbons > C_7) where ignition delay times for non-dilute mixtures are reported for Jet-A, JP-8, and two proposed surrogates containing quantities of toluene, benzene, iso-octane, and n-decane, where toluene and iso-octane concentrations are varied.[59–60] Experimental data were compared to several kinetic mechanisms predicting ignition of jet fuel. The results most closely agreed with the model of Ranzi et al., however at lower temperatures model prediction shows NTC behavior where the data do not.

Fuels used in internal combustion (IC) engines are typically comprised of several hydrocarbon families and surrogate replacements have been proposed and studied for several years along with individual fuels used in surrogate fuel blends.[61–67] Fikri et. al. performed a series of shock-tube experiments to measure ignition delay times of two gasoline surrogates for spark-ignition (SI) engines with the purpose of contributing to the refinement of a kinetic model.[66] Stoichiometric blends of [14.5% n-C_7H_{16} /44.5% i-C_8H_{18} /41% C_2H_6O – Surrogate B] and [17.5% n-C_7H_{16} /5.5% C_7H_8 /19.5% i-C_8H_{18} /8% C_8H_{16} (diisobutylene) – Surrogate C], where percentages are molar based, were studied at 10, 30 and 50 bar over a wide range of temperature. As with Surrogate B, Surrogate C exhibited negative temperature coefficient

(NTC) behavior in the 30- and 50-bar cases, while ignition measurements at 10 bar were distributed linearly with inverse temperature. An empirical ignition delay time correlation was constructed, however a single equation did not accurately represent the ignition data for both blends. This behavior was ascribed to a difference in pressure exponent, taking on a value of -0.960 for Surrogate B and -0.650 for Surrogate C. A similar ignition delay time study was conducted in a shock tube by Herzler et al. where a 28% n-C_7H_{16} 72% C_7H_8 (mol. %) formulation comprised a gasoline surrogate.[67] Equivalence ratio was varied between fuel-lean (ϕ = 0.3) and stoichiometric (ϕ = 1.0). A pressure dependence of -0.883 was calculated for the empirical correlation describing the ignition delay time.

Diesel engines are composed on average of alkanes, alkenes, and aromatics. Decane ($C_{10}H_{22}$) is commonly used as a reference fuel for petroleum-based diesel fuel and has received recent attention.[68–70] Argon-diluted mixtures of decane and oxygen were ignited behind reflected shock waves in a heated shock tube from 2 to 10 atm over a wide range of temperature.[68] Alkane and alkene combustion products were also characterized, relative to [$C_{10}H_{22}$], as a function of temperature. A kinetic model was constructed around the experimentally measured ignition and product data, and an empirical ignition correlation as a function of mixture concentration and temperature was calculated.

Homogeneous charge compression ignition (HCCI) engines employ the advantages of both SI and CI engines, acting as a hybrid, to partially address pollution and fuel efficiency issues through mechanical means. HCCI engines utilize a homogeneous mixture of fuel and oxidizer (as in SI engines) and induce combustion through auto-ignition by achieving high engine pressures (as in CI engines). Since ignition occurs simultaneously at multiple locations within the reactive homogeneous mixture as the fuel and oxidizer are brought to elevated pressure, a more complete burn is achieved. The process has advantages in that reduced quantities of soot and NO_x are produced, relative to conventional CI engines.[71] Issues remain to be addressed, however, specifically in regards to the higher levels of UHCs and CO which are being attempted by chemical means. Several experimental and modeling works have contributed to the plausibility of an HCCI fuel.[72]

Gas turbine applications have a particularly important use for ignition delay time data due to concerns of adverse combustion phenomena (flashback, blow-off, instabilities). Owing to its abundance in North America as a natural resource, combustion of natural gas and synthetic formulations of natural gas have been studied under high-pressure conditions commonly used in gas turbine engines for power generation.[73–77] Ignition delay times of hydrocarbon mixtures have also been investigated for associated effects on explosion parameters (explosion pressure, maximum rate of pressure rise).[78]

3. COMBUSTION STUDIES INVOLVING n-NONANE

Nonane (C_9H_{20}) is a higher-order hydrocarbon which is a constituent in diesel and jet fuels and yet has received only limited experimental and modeling attention. Conversely, numerous combustion experiments have been performed on octane[79–80] (C_8H_{18}) and decane[81–83] ($C_{10}H_{22}$), and chemical kinetic mechanisms have been developed for both.[84–89] Recently, Westbrook et al. constructed a detailed mechanism for high-order n-alkanes from C_8 to C_{16}.[90] In the comprehensive work, ignition delay times at 13.5 bar and ϕ = 1.0 were gathered from the literature for n-heptane (C_7H_{16}) and n-decane (n-$C_{10}H_{22}$), which show overlap. An extension is then made, from the observation of overlap, in which the model is used to calculated ignition delay times for similar heavy hydrocarbons from C_7 – C_{16}. Ignition delay times for n-nonane (C_9H_{20}) are calculated, however are not compared to experimental data for verification. In a separate study, Ji et. al. developed a kinetic model of 188 species and 1446 reactions to compute laminar flame speeds and extinction strain rates of C_5 – C_{12} n-alkane flames as a function of equivalence ratio.[91] The model slightly under-predicted measured fuel-lean and stoichiometric flame speeds of n-nonane.

Fundamental combustion studies on C_9H_{20} ignition, temperature- and pressure-dependent reactivity, and oxidation pathways are not available in the literature. A detailed chemical kinetic study on hydroxyl reactions with linear hydrocarbons[92] focused mainly on OH rate coefficient measurement with ethane (C_2H_6), hexane (C_6H_{14}), heptanes (C_7H_{14}), octane (C_8H_{18}), nonane (C_9H_{20}), and decane ($C_{10}H_{22}$), however, rate coefficients were measured for C_9H_{20} + OH $\rightarrow$ Products by the authors near 1 atm over a temperature range of 1010 K – 1131 K. A pyrolysis study was conducted in a downflow reactor for C_9, C_{12}, C_{13}, C_{16}, and C_{22} straight-chain alkanes to determine the major yield products using gas chromatography.[93] Nonane was observed to have decomposed into the following, predominantly 1-alkene species (in descending weight percentage of combustion products): heptene (1-C_7H_{14}), hexane (1-C_6H_{12}), pentene (1-C_5H_{10}), butane (1-C_4H_8), ethylene (C_2H_4). Rate coefficients were also measured for thermal decomposition of nonane. Kunzru et al.[94] performed a detailed study on the thermal decomposition of pure n-nonane using a flow reactor with pressure maintained at 1 atm and temperature varied from 920 K – 1020 K, reporting the frequency factor (Arrhenius pre-exponential, *A*), order of reaction, and activation energy for the decomposition reaction. In agreement with the work of Zhou et. al.[93], ethylene was again observed in the measurements as the dominant product of pyrolysis, a result which additionally agreed with a model proposed by Rice.

Nonane served as a fuel for investigating the sooting dynamics and droplet morphology of single-droplet combustion where, using a low-gravity approach, spherical gas-phase combustion is promoted around 600 μm droplets of nonane.[95] The paper investigates the effect of pressure (10 atm – 30 atm) on the growth of

soot clouds from combustion of the droplet and droplet morphology after ignition. A similar series of independent experiments was conducted wherein the droplet combustion dynamics of JP-8 jet fuel were compared against those of nonane.[96,97]

Shock tubes provide a means by which uniform, rapid compression and subsequent near-instantaneous heating of reactive mixtures is achieved, and are thereby ideally suited for controlled, fundamental studies of combustion chemistry, as discussed in Section 2. Presented herein is the first detailed series of experiments on n-nonane combustion using a shock tube with emphasis on measurements of highly-dilute ignition delay times and resulting features of OH* and CH* species profiles obtained through chemiluminescence measurements.

4. EXPERIMENTAL METHODOLOGY

The approach to measure both OH* and CH* time-histories using chemiluminescence and corresponding ignition delay times involves the use of a shock tube. A detailed description of the shock-tube facility is provided, covering the main components, geometric configuration, measurement equipment, facility-specific attenuation rates and corresponding temperature uncertainty, optical diagnostics, and data acquisition system. The present work involves only high-dilution mixtures, however diagnostics for analyzing combustion phenomena from both dilute and non-dilute mixtures are discussed. Test times for the shock-tube configuration are shown through pressure traces obtained at several different conditions, depending on experimental temperature goals and driver/driven gas composition. An experimental series of data was measured to validate the use of the present facility in reporting chemical kinetic and ignition data. The series comparison uses ignition delay time data from four different shock-tube facilities: a high-pressure shock-tube at Texas A&M University (TAMU), a shock-tube facility at The Aerospace Corporation[98], and a correlation constructed from shock-tube data taken at Stanford University[99]. Details of the experimental objectives undertaken are also discussed.

4.1 Description of facility

The low-pressure shock-tube facility at TAMU utilized for combustion experiments, hosts a 6.1-m long stainless steel shock tube (Fig. 5). The internal dimensions for the circular driver and square driven sections are 7.6 cm and 10.8 cm, respectively. The driver section (L /D = 23.6) is supplied driver gas (typically helium) either through an electronically enhanced solenoid valve employed to control the time taken to rupture the diaphragm or a system of manual valves used for experiments where control over the rupture-time for the diaphragm is not important. Reflected-shock pressures and temperatures up to 10 atm and 5000 K, respectively, are safely obtainable in the low-pressure facility.

The leak rate of the shock tube was characterized to provide a measure of purity to be expected for each experiment. From high-vacuum conditions ($P \sim 10^{-6}$ torr $\sim 10^{-9}$ atm) a rate of 4.18 mtorr /min. of ambient air leaked in to the shock tube vessel. A second measurement was taken under conditions commonly used in the shock-tube experiments where initial pressures of the reactive mixture (test gas) are much higher than 10^{-6} torr; a lower rate is thus expected since the ΔP across the shock tube is much lower. A reduced rate of 7.44 μtorr /min. was measured when a typical low initial pressure of 32.0 torr was used as the initial pressure. Since experiments are typically run within 1 min., impurities are negligible (32.0 torr of test gas, 7.44 μtorr of impurity /ambient air).

Shock-front velocity is precisely measured through the use of four high-frequency piezoelectric pressure transducers (PCB 113A) mounted atop the driven section at locations toward the end of the shock tube in conjunction with 120-MHz counters /timers (Phillips P6666), using respective distances between pressure sensors and the recorded time intervals. For a given measurement of shock speed, two pressure transducers are employed to report an initial time and final time where the initial time indicates the arrival of the (incident) shock at the first transducer, and the final time indicates the arrival at the second. The 120-MHz sampling rate allows the timers to provide shock velocities on microsecond (10^{-6} s) timescales. In total, the four pressure sensors make up a three-interval field within which velocities is measured. A linear extrapolation of the measured velocities is used to calculate the shock speed at the plane of the endwall where the reflected shock forms. An extrapolation is required due to physical limitations in positioning the pressure transducer directly at the endwall. Three measurements of shock speed are made, and a linear trend of the three data points is then calculated from which then the velocity of the shock at the arrival of the endwall is extracted (Fig. 6).

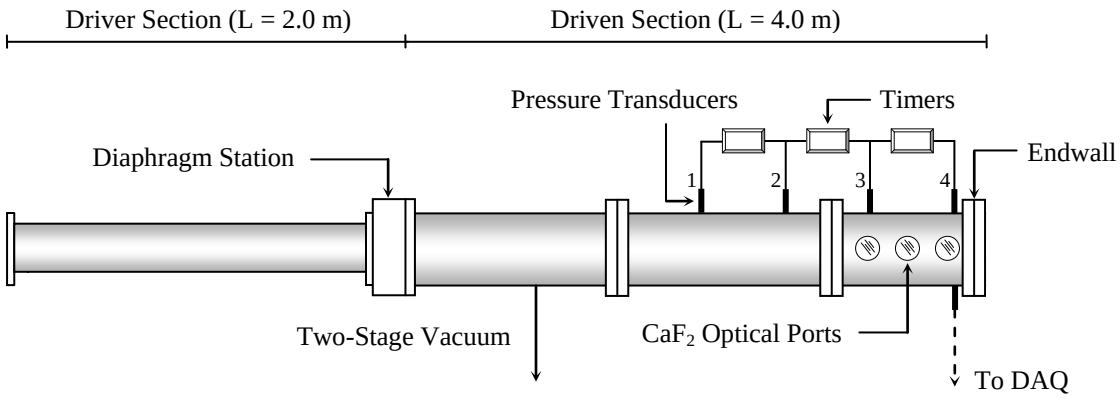

Fig. 5. Chemical Kinetics and Gas Dynamics low-pressure shock-tube facility at Texas A&M University. High-purity conditions are ensured by the two-stage vacuum system. An incident shock wave is formed upon diaphragm rupture. Four high-frequency pressure transducers provide shock speed measurement. The incident wave reflects from the endwall and creates the test region. An upper limit of 1.5 ms within the test region is available. Calcium-Fluoride optical ports allow non-intrusive probing of chemically reacting fuel and oxidizer for spectroscopic measurements of electromagnetic radiation, temperature, and species concentration. Measurements are made at MHz frequencies to resolve data on chemical timescales.

Due to contact between fluid moving behind the incident shock wave and the internal, solid walls of the shock tube attenuation is present as the wave loses energy during propagation. The degradation of this energy (shock strength) translates to a decrease in momentum, and in turn an uncertainty in reflected-

shock temperature, a physical consequence shown in Fig. 6 (velocity decreases with increasing distance). Attenuation is quantified by considering the change in shock front velocity over a given distance:

$$Percent\ Attenuation\ per\ Meter = \frac{\left(\frac{\mathcal{V}_{Final} - \mathcal{V}_{Initial}}{\mathcal{V}_{Initial}}\right) \cdot 100}{Length\ of\ Measurement\ Region\ (m)}$$

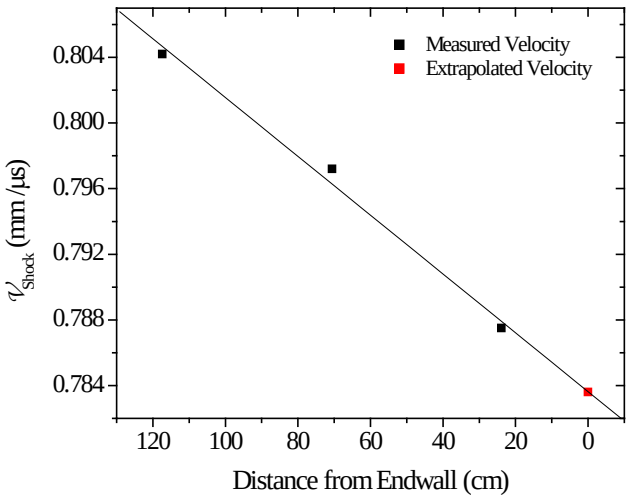

Fig. 6. Incident-shock velocity measurements. Linear extrapolation is used to calculate velocity at the endwall. $R^2 = 0.99$. Attenuation rate = $0.015\mathcal{V}_{Initial}$ /m. Solid line indicates experimental linear fit.

Computation of shock velocity serves as one of two input variables, the other of which being the initial pressure of the driven gas (P_1), to arrive at a characteristic solution of the Rankine-Hugoniot shock relations. The shock relations are solved iteratively using real-gas thermodynamics, employing $c_P(T)$, $c_V(T)$, s(T), and h(T) data from Sandia National Laboratories to define conditions within the reflected-shock region pertinent to a given experiment.

The loss in energy poses an uncertainty since the last point where velocity is determined is the linearly extrapolated value at the endwall. Once the reflected-shock wave forms and begins travelling back toward the diaphragm station, its velocity at the sidewall station (1 cm from the endwall) is assumed to be equivalent to that which was present at the endwall. The source of uncertainty arises from the reliance on numerical solution of conservation equations to yield experimental conditions of temperature and pressure, which require two inputs: velocity and initial pressure. Since the reflected-shock inherits further attenuation once it departs the endwall plane, the velocity is known within the bounds of the calculated

rate of attenuation. Rates of attenuation increase as the reflected-shock passes through a higher-temperature gas and has to interact with the boundary layer formed by the flow behind the incident shock wave.[27] Attenuation rates from hydrodynamic implications are on the order of 1.0 – 1.5% per meter imposing a maximum uncertainty in the calculation of temperature of approximately ± 10 K.

After the attenuating shock wave passes over the surface of the pressure transducers (d = 5.54 mm) used to measure velocity, the shock front continues its path and approaches the endwall, where two distinct diagnostic stations for measurement of (1) pressure and (2) optical/spectroscopic phenomena are met – sidewall and endwall stations. The two stations provide similar measurements, yet possess different vantage points. The use of sidewall diagnostics provides valuable time-dependent species-specific chemistry, however measurements made in this plane suffer from effects of boundary layer formation, shock bifurcation, and, for non-dilute mixtures, accelerated shock speeds which add additional uncertainty to the accuracy of temperature calculations. Usage of endwall diagnostics avoid boundary layer-related issues and as a result provide pressure measurement without the potential for bifurcation intervention. Further, test gas closest to the endwall incurs less heat transfer from otherwise prolonged exposure to the incident shock wave. Test-gas further from the endwall experiences the temperature and pressure created by the incident shock wave for longer periods of time, between incident-shock departure from the given plane of interaction between the incident shock and the test gas and reflected-shock arrival at the same cross-section of test gas. Thus, chemistry measurements, which are highly temperature-dependent, can be recorded with higher certainty with diagnostics located closer to the endwall. Hence, positioning the sidewall diagnostic station as close to the endwall as possible mitigates both boundary layer issues as well as reduces temperature uncertainties arising from pre-heating within the incident shock wave.

Optical and spectroscopic measurements frequently involve differential laser diagnostic techniques whereby a single laser beam of certain wavelength or multiplexed array of wavelengths is passed through the shock tube to interrogate the formation/depletion of certain species, probe for temperature, or to measure velocities. Additionally, emission spectroscopy measured from the exiting of electromagnetic radiation from the reacting fuel and oxidizer provides pertinent kinetic data. For these and other measurements, optical access is required in shock tubes which are routinely employed for experiments which utilize such techniques. Therefore, for shock tubes in which chemistry and chemical physics are of interest, a sidewall diagnostic station is a necessity and positioning the station close to the endwall is advantageous, as mentioned previously.

Pressure measurements at the sidewall provide time-of-arrival information for both incident and reflected shock waves. Sidewall pressure is recorded using a 500-kHz quartz pressure transducer (Kistler 603B1).

Sidewall emission of photons from excited species during combustion is tracked using a detector which employs a photomultiplier tube (Hamamatsu Type 1P21), the output signal from which undergoes amplification using a low-noise pre-amplifier (SRS SR560). UV-filtering is employed to observe emission at two specific wavelengths, λ_{OH^*} and λ_{CH^*}. One narrowband filter (10 nm FWHM) centered at 430.0 nm is utilized to capture the ultra-violet CH* chemiluminescence while a separate, 10-nm FWHM filter centered at 307.1 nm passes emission only from the OH* species. The sidewall-positioned window and centerline of the sidewall pressure transducer form a diagnostic plane (field of view) which is positioned 1 cm from the endwall. The distance between the sidewall diagnostic plane and the endwall is minimized to reduce the uncertainty in shock speed and resulting uncertainty in thermodynamic state of the reflected-shock gas. Although not used for analysis in the present work, endwall diagnostics are available. Endwall pressure is obtained using a PCB 113 A and a photodiode (New Focus 2032) with a range of wavelengths (190 nm – 1100 nm) monitors emission down the longitudinal axis of the shock tube. Data for each of the four diagnostics (sidewall pressure and emission, and endwall pressure and emission) are recorded using two 16-bit, 25-MHz Gage Applied Sciences data acquisition boards (CS8482).

Careful attention is paid to the set up and optical alignment of the photomultiplier (PMT) detector in order to maximize signal-to-noise (S /N) ratio, force the detector to see a thin plane inside of the test section of the shock tube, and avoid interference emission. A visible Helium-Neon (HeNe) laser (632 nm) is centered with and passed through a window on one side the shock tube directly into a medium placed inside of the test region which causes the light to disperse, simulating the multi-directional emission that occurs during combustion. The dispersed light is then transmitted through an identical window on the opposite side of the shock tube and collected onto a concave mirror of focal length f = 10 cm. The concavity of the mirror reforms the collected, yet still dispersed light emitting from the shock-tube window into a single, focused point positioned directly onto the detector. Minor adjustments are then made to maximize the S/N while monitoring signal output. During alignment, the PMT detector is unfiltered so that it may see the visible 632 nm light. After optimal alignment is achieved, a bandpass filter is appended to the PMT viewport. The window from which emission exits is unobstructed during alignment, however throughout the experiment, emission from combustion exits a single CaF_2 window through the 400 μm slit. The other (opposing) window is covered so that peak intensity is observed through a single window on the side of the shock tube the detector is positioned. Purposely obstructing the window using a 400-μm slit reduces the field of view of the detector, ensuring minimal interference from wall reflections is incurred. The slit also acts to restrict the detector to a (ideally infinitesimally thin) plane which is representative of a chemically reacting cross-section within the volume of the test region.

Optical bandpass filters possesses a specific bandwidth comprised of a center wavelength bound by a minimum wavelength and a maximum wavelength the filter is capable of passing, forming a Gaussian distribution of intensity as a function of wavelength. The bandwidth for the filters used herein is 10 nm, and to eliminate interference from electromagnetic radiation emitted from other species or particles that emit at wavelengths within the spectral band of the filter, the sidewall detector is positioned at an angle approximately 150° from the window (Fig. 7). The converse to this approach, aligning the detector face normal to the window, could result in artificially larger signals as species emitting within the allowable wavelength regime would contribute to the intensity measured by the detector. Emission also exits a calcium-fluoride optical port located inside of the endwall where measurements are made within the UV-VIS spectrum using a photodiode to provide qualitative affirmation of ignition.

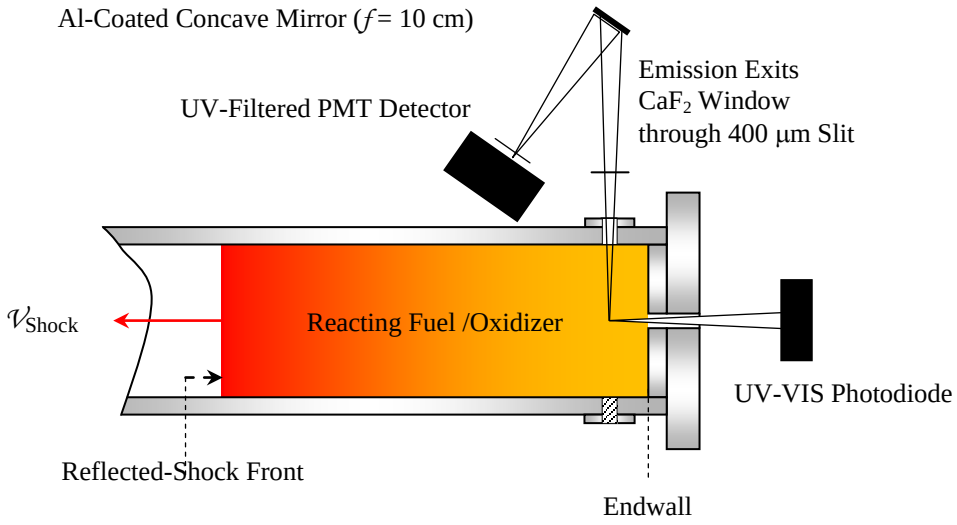

Fig. 7. Emission from reacting fuel and oxidizer behind reflected-shock is measured at a sidewall location 1 cm from the endwall using a UV-filtered photomultiplier tube.

4.2 Corroboration of shock-tube data on methane ignition with established data and correlation

Shock-tube ignition of stoichiometric methane in 99.5% argon data from the literature was employed to compare data measured in the shock-tube facility utilized for the present experiments (Fig. 8). Ignition delay times measured using CH* emission in all cases were conducted near 1 atm or at a slightly different pressure, in which case a pressure-adjusted time is reported using a pressure exponent, n = 0.72. Ignition delay times from the low-pressure shock-tube facility were compared to those measured in shock tubes at The Aerospace Corporation[98], Stanford University[99], and the high-pressure shock-tube facility at Texas A&M University and excellent agreement is observed in the ignition results from the different facilities

and the Stanford ignition delay time correlation. An upper limit on ignition delay time of approximately 1000 μs (1.0 ms) is adhered to for measurements in the low-pressure facility.

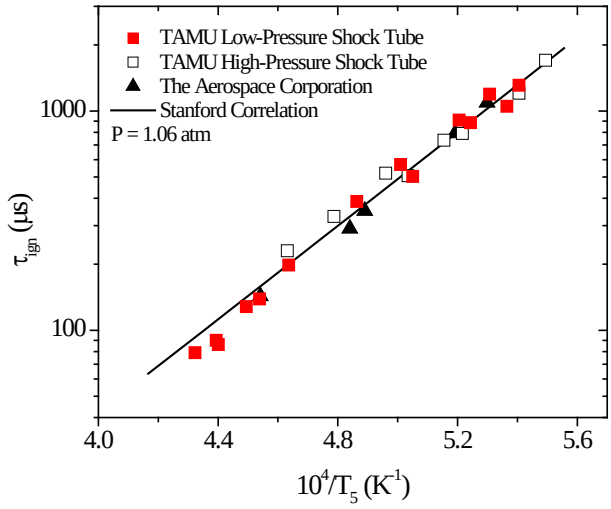

Fig. 8. Comparison of ignition delay times of methane in oxygen ($0.00163CH_4 + 0.00337O_2 + 0.99500Ar$) at 1.06 atm measured in different shock-tube facilities.

4.3 Definition of test time

Test times for the abovementioned shock-tube geometry are within 1.0 – 1.6 ms with extensions up to 5 ms obtainable through driver-gas mixtures. Pressure histories in nonreactive mixtures from both the sidewall and endwall locations (Figs. 9.A and 9.B) reveal the available test times for pure argon at, respectively, the maximum and minimum temperatures employed in the present study. At both extremes, an available test time of 1.6 ms was measured.

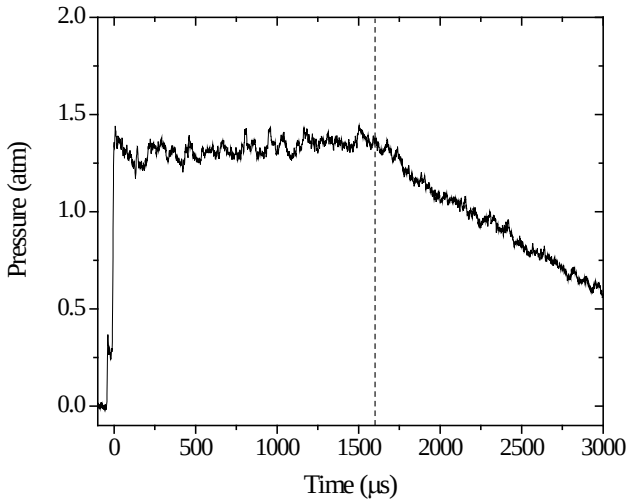

Fig. 9.A. Sidewall pressure in pure argon at 1619 K, P_5 = 1.33 atm. P_1 = 31.7 torr. The first rise in pressure indicates the arrival of the incident shock, while the second rise in pressure is the passing of the reflected shock wave over the sidewall diagnostic station. An expansion wave arrives at t ~ 1.6 ms and the steep pressure decrease indicates change in the thermodynamic conditions and defines available test time (~ 1.6 ms).

Theoretical determination of the length of time available for study behind the reflected-shock wave is presented as a function of shock-tube geometry, initial acoustic speed, incident Mach number, and specific heat ratio[27], yet deviation from that which is experimentally measured is present in the results due to the difficulties in incorporating viscous effects into the fluid dynamic equations. The test time is defined either by the arrival of the contact surface to the test region near the endwall or by the overtaking of the contact surface by the rarefaction tail reflected off of the driver section. The nature of these complex gas dynamic processes, formation and structure of the contact surface, and interaction of the reflected-shock wave with the contact surface are provided in several references[27–35], yet Gaydon and Hurle[27] provide the most elaborate and physically descriptive explanation. The arrival of the contact surface in the test region poses scenarios dictated by thermodynamics (equality of specific heat ratios). For the case where γ is constant across the contact surface, three results are possible, noting that the contact surface separates regions 2 and 3: $a_2 > a_3$, $a_2 < a_3$, and $a_2 = a_3$. In the cases where acoustic inequalities are present, wave reflections result from the interaction of the reflected-shock wave with the contact surface. Under the condition of acoustic speed equality, no reflections occur and the test time is extended as a result (ending by the arrival of the expansion wave from the driver section). In the present experiments, helium was used exclusively as a driver gas, and the acoustic speed in region 3 is high (a_3 ~ 1040 m /s) due to its low molecular weight. In a

typical experiment, with the incident shock wave creating a higher-temperature region 2, the acoustic speed a_2 is approximately 550 m /s, thus for the experiments conducted herein the case $a_2 < a_3$ is described.

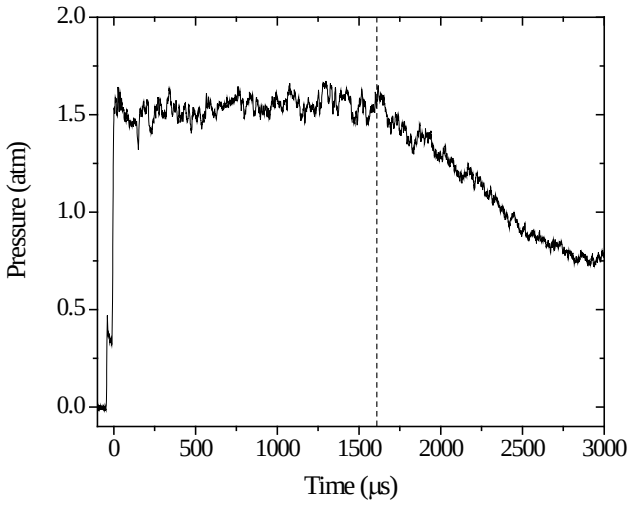

Fig. 9.B. Sidewall pressure in pure argon at 1312 K, P_5 = 1.53 atm. The steep pressure decrease indicates changes the thermodynamic conditions and defines available test time (~ 1.6 ms). P_1 = 50.2 torr. The first rise in pressure indicates the arrival of the incident shock, while the second rise in pressure is the passing of the reflected shock wave over the sidewall diagnostic station. An expansion wave arrives at t ~ 1.6 ms and the steep pressure decrease indicates change in the thermodynamic conditions and defines available test time (~ 1.6 ms).

Upon reflection from the endwall, appending the reference frame onto the shock front, the shock wave takes on a Mach number higher than that of the incident shock due to the higher temperature created in region 2 ($a \propto T^{0.5}$). When the reflected-shock wave meets the contact surface, a rarefaction reflects back toward the endwall through the test section. A change in thermodynamic state is then registered where a decrease in pressure and temperature alters the conditions created by the reflected-shock wave, and the experiment ceases. This behavior is shown above in Figs 9.A and 9.B. Therefore, measurements behind reflected-shock waves were made at times less than 1 ms to remain within the bounds of the shock-tube test time.

4.4 Composition and preparation of mixtures

Highly dilute mixtures of n-C_9H_{20} /O_2 in Ar were prepared at three levels of equivalence ratio (Table 3); fuel-lean (ϕ = 0.5), stoichiometric (ϕ = 1.0), and fuel-rich (ϕ = 2.0). The equivalence ratio is defined herein as:

$$\phi = \left(\frac{x_{Fuel}}{x_{Oxidizer}}\right) \Big/ \left(\frac{x_{Fuel}}{x_{Oxidizer}}\right)_{Stoichiometric}$$

Table 3. Composition and stoichiometry of mixtures.

ϕ	%C_9H_{20}	%O_2	%Ar
0.5	0.1	2.8	97.1
1.0	0.1	1.4	98.5
2.0	0.1	0.7	99.2

The mixtures were prepared in a chamber separate from the shock tube using the partial pressure method. Inside the mixing chamber, turbulent mixing is promoted through an internal multi-hole delivery tube where the holes are out of phase with one another and span the length of the chamber. High-purity research-grade (> 99.9995%) oxygen and argon were employed. Since the vapor pressure of nonane is low at room temperature (~ 3.0 torr), a vacuum-sealed cylinder containing condensed-phase nonane was exposed to the mixing chamber at low-pressure (~ 10^{-6} torr) and allowed to evaporate to a pre-determined partial pressure. Correspondingly, precautions were taken to ensure mixture homogeneity and avoidance of condensation inside of the supply lines and mixing chamber. First, mixtures were made with the partial pressure of the nonane roughly 60% of its room temperature vapor pressure (i.e. < 2.0 torr). During the addition of the other constituents (oxygen and argon), pulses were used to further promote mixing during their individual injection. Antoine[100] extended the Clapyeron equation for vapor-liquid phase equilibrium by adding a third constant:

$$log_{10}\left(P_{vapor}\right) = A - \frac{B}{T + C - 273.15}$$

The values of constants A, B, and C are calculated using regression analysis from experimental data over a prescribed range of temperature. For nonane (C_9H_{20}), the constants A, B, and C are 4.07356, 1438.030, 202.694, respectively.[101] Carrying out the vapor pressure calculation at 293 K yields:

$$P_{vapor\ ,C_9H_{20}}\ (T = 293\ K) = 3.07\ torr$$

The vapor pressure at 293 K for the n-nonane used in the study (Sigma-Aldrich N29406, assay 99%) was verified using a high-sensitivity (0 – 10 torr) MKS dual capacitance manometer. A second precaution was taken whereby a minimum waiting time of 24 hours was adopted prior to using the mixture for experimentation to allow for further mixing through diffusion. A total of six mixtures were made – two identical mixtures of each ϕ – to ensure repeatability of the mixing procedure and measurements. Repeatability is of particular importance due to the low vapor-pressure of the fuel and corresponding concerns over fuel condensation, the issue being the potential for an inhomogeneous mixture.

*4.5 Definition of ignition delay time through measurements of time-histories of OH**

Species profiles provide a means by which kinetics models can be developed from comparison of the time rate of change of a given species measured in an experiment to *ab initio* calculations. Using the convention described by Petersen[102], highly diluted mixtures are best suited for studies of chemical kinetics, where the diluent concentration is sufficiently high (> 95%) such that energy release is limited, rendering temperature and pressure constant throughout the length of the experiment. In many cases, the rise in pressure from combustion of such mixtures is diminutive and does not manifest in the recorded pressure history behind the reflected-shock. Conversely, endwall measurements are preferred for mixtures where diluent concentration is low (< 95%). For this reason, such mixtures are considered highly energetic due to the large quantity of bond breakage and formation during oxidation. Resultingly, pressure and temperature rise during combustion making unfavorable conditions for condition-sensitive chemistry measurements.

Ignition delay times are defined herein using the method of steepest ascent as applied to OH* chemiluminescence measurements (Fig. 10). The method entails constructing a horizontal line representing zero-concentration of the intermediate species being measured. The line is extended from time-zero throughout the length of the profile to establish a reference (zero) concentration from which changes with time are measured. A second line is then drawn along the slope with the steepest ascent in the profile, indicative of rapid population of the intermediate radical pool, to intersect with the reference line. The difference in time between time-zero (arrival of reflected shock wave at sidewall location) and the intersection point is the ignition delay time $\tau_{Ignition}$, measured in microseconds (μs).

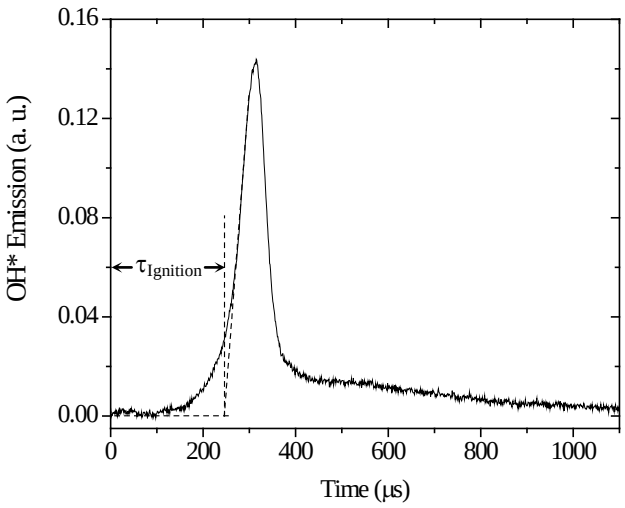

Fig. 10. Definition of ignition delay time using the method of steepest ascent with sidewall OH* emission. $0.001C_9H_{20} + 0.028O_2 + 0.971Ar$ ($\phi = 0.5$). T = 1403 K, P = 1.52 atm, $\tau_{Ignition}$ = 247 μs.

5. EXPERIMENTAL RESULTS OF n-NONANE COMBUSTION

Experimental results for species time-histories of excited hydroxyl (OH*) radicals and ignition delay times for $C_9H_{20}/O_2/Ar$ mixtures were measured behind reflected shock waves for three equivalence ratios (ϕ = 0.5, 1.0, and 2.0) at a fixed pressure near 1.50 atm. OH* formation was measured using emission spectroscopy of the $A^2\Sigma^+ \rightarrow X^2\Pi$ transition. A temperature range of 1268 < T (K) < 1627 was covered by varying the incident-shock speed from 0.736 < v_{Shock} (μm /μs) < 0.831 using initial pressures 50.2 < P_1 (torr) < 31.5. A strong pre-ignition feature was observed in the chemiluminescence of OH* and is described in detail. Ignition delay times, measured from OH* time histories show Arrhenius behavior and are reported along with calculated activation energies.

5.1 Details on the use of sidewall diagnostics for measurements

All measurements reported were obtained from a sidewall location positioned 1 cm from the endwall containing a high-frequency pressure transducer for pressure measurement and a CaF_2 windowed port allowing for emission diagnostics to observe the combustion event. Fig. 11 shows representative sidewall pressure and emission traces and Fig. 12 shows those as observed from the endwall. Time-zero is defined qualitatively as the arrival of the reflected shock which initiates the constancy of thermodynamic conditions (temperature, pressure) and is taken herein at the time of reflected-shock arrival at the sidewall location (Fig. 11).

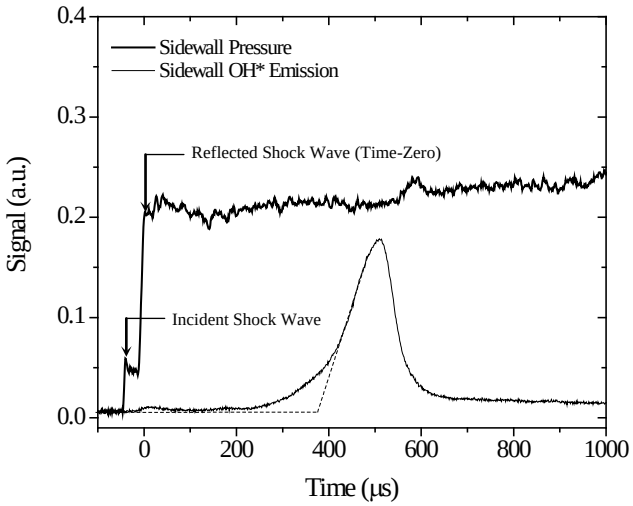

Fig. 11. Typical pressure and OH* emission traces as measured from the sidewall for $0.001C_9H_{20} + 0.014O_2 + 0.985Ar$ (ϕ = 1.0). T = 1447 K, P = 1.57 atm, $\tau_{Ignition}$ = 378 μs. Time-zero defined upon arrival of the reflected-shock at the sidewall location.

Petersen[102] discussed in detail the implications associated with diagnostic location and provides recommendations on reporting ignition delay times in both dilute and non-dilute reactive mixtures. Using an analytical optical model, Petersen showed that the integrative effect of an endwall-positioned emission diagnostic leads to artificially longer ignition delay times for dilute mixtures due to a convolution of initial signal intensity with emission contributions from ignition at points downstream of the endwall. The observation was made in two previous works where OH* chemiluminescence was used to measure ignition delay times under dilute conditions at both sidewall and endwall positions. Discrepancies between sidewall-measured ignition times, which agreed with the kinetics model of Wang and Laskin[103], and endwall-measured ignition times from 10 μs to 60 μs were observed, and relative differences between endwall- or sidewall-defined ignition delay times showed a dependence on temperature with the percentage difference between the two definitions decreasing with decreasing temperature. Thus, for higher temperatures, a larger percentage-discrepancy is observed between definitions of ignition time from the two diagnostic locations. Thus, sidewall measurements are reported herein to avoid such issues and to extract time-dependent species concentrations from conditions ideal for measurements of chemical kinetic phenomena – constant temperature and pressure behind the reflected shock afforded from the high level of dilution and corresponding diminution of energy release. Endwall diagnostics are best suited for experiments which involve larger molar quantities of fuel (> 3% by vol.). In such mixtures, the abovementioned effect is lessened due to an acceleration effect of the shock wave being fed by combustion processes behind it.

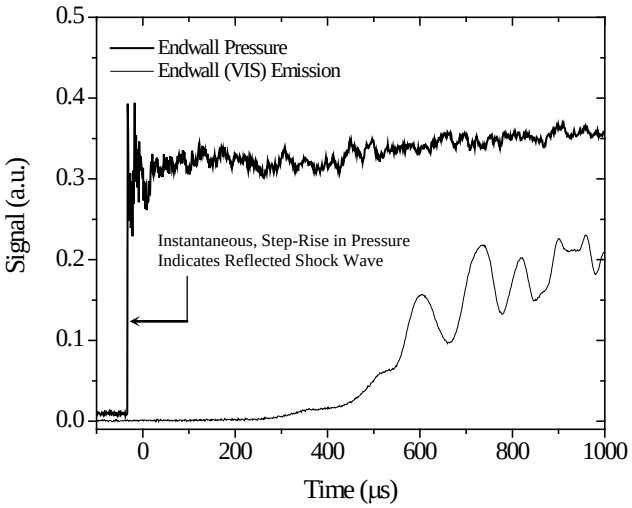

Fig. 12. Typical pressure and OH* emission traces measured from the endwall for $0.001C_9H_{20} + 0.014O_2 + 0.985Ar$ ($\phi = 1.0$). Ignition unable to be defined due to the inherent integrative effect of the endwall emission diagnostic enabling light to be measured axially throughout the shock tube and distort the initial intensity rise.

5.2 OH time histories*

Time-dependent species concentration profiles were measured for OH* under fuel-lean (ϕ = 0.5), stoichiometric (ϕ = 1.0), and fuel-rich (ϕ = 2.0) equivalence ratios. Each equivalence ratio displayed a particular characteristic of interest to the modeling of the chemical kinetics of the combustion process. Features characteristic to each stoichiometry condition and others common to all equivalence ratios are discussed in their respective sections. One such feature is a decrease in peak formation time of OH* post-ignition, defined as the length of time which exists from the point of ignition to the peak of the OH* profile (Fig. 13).

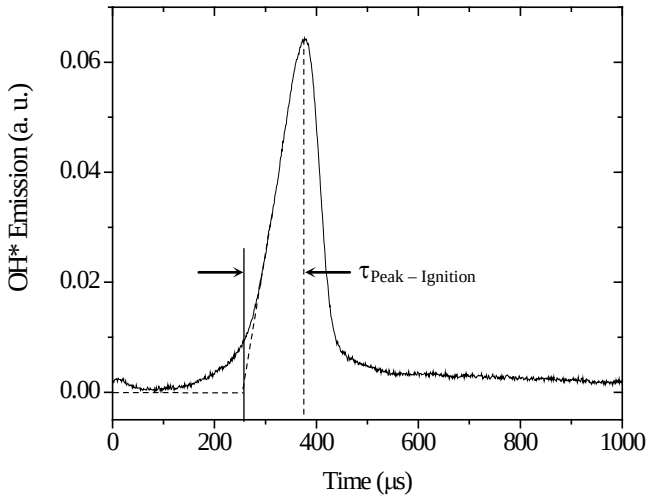

Fig. 13. Definition of post-ignition rise-time, $\tau_{Peak - Ignition}$. $\tau_{Ignition}$ = 254 μs, $\tau_{Peak - Ignition}$ = 168 μs.

5.2.1 Fuel-lean OH behavior*

With the exception of only one case, no presence of a major feature during production or consumption of the species was observed, and the measured profiles exhibited smooth and nearly symmetric behavior. However, it is noteworthy that a slight pre-ignition rise in OH* concentration was detected for temperatures exceeding 1400 K (Fig. 14). In each of the five cases where this phenomenon was observed, ignition delay times were less than 200 μs. Further, within the envelope of T > 1400 K, the height of the peak increased with increasing temperature.

The percentage of the pre-ignition curve height, relative to the main ignition curve height varied from 1.8% to 3.5% of the total rise in OH*, thus the relative amount of pre-ignition OH* is small yet potentially

relevant to the governing kinetics. The time-span over which the pre-ignition phenomenon occurred was measureable in only two of the five cases where the behavior was observed. At T = 1399 K, the duration of the pre-ignition phenomenon was 63 μs, and at an increased temperature of T = 1425 K the duration lasted 80 μs, where the duration is defined as the time interval between a measurable quantity of OH* and the return of the species concentration to the initial level (at time-zero). In the cases where the time interval was immeasurable, the pre-ignition behavior sustained through to the point of ignition. The time at which the pre-ignition phenomenon initiated was consistent, ranging narrowly from 33 μs – 37 μs.

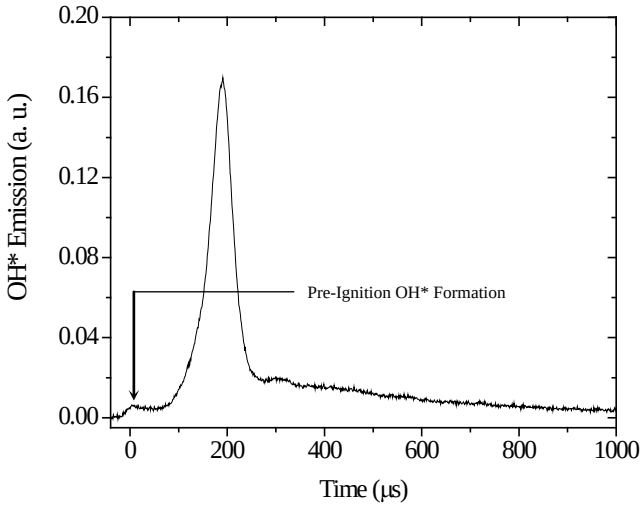

Fig. 14. OH* species profile (ϕ = 0.5). T = 1458 K, P = 1.51 atm, $\tau_{Ignition}$ = 129 μs, $\tau_{Peak - Ignition}$ = 109 μs. A slight pre-ignition formation of OH* is present.

Another characteristic apparent in the fuel-lean species profiles occurred after peak concentration and ensuing rapid (primary) depletion where the majority of the species is consumed. A tendency persisted for secondary consumption, differing from primary consumption by rate, of the remaining OH*, occurring over a period of several hundred microseconds after ignition (Fig. 15). Calculations of emission intensity at t = 1000 μs (1 ms) relative to the zero-concentration (baseline) intensity show that emission from OH* post-ignition varied from 4.8% to 9.0%. The behavior occurred at all temperatures up to 1343 K. The change-in-rate behavior showed no significant dependence on temperature, yet at an upper limit of a 1-ms ignition delay time, the behavior ceased as the OH* concentration re-attained the zero-concentration level. Profile widths, indicative of the amount of time OH* remained present in the reactive system, showed a tendency toward decreasing with increasing temperature.

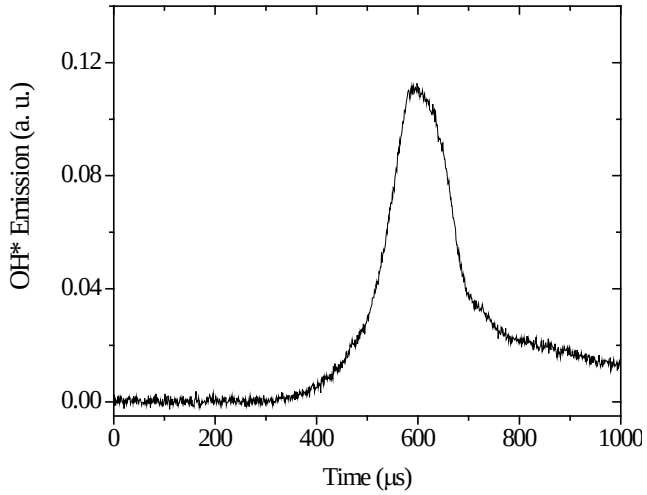

Fig. 15. OH* species profile (ϕ = 0.5). T = 1349 K, P = 1.58 atm, $\tau_{Ignition}$ = 485 μs, $\tau_{Peak - Ignition}$ = 157 μs. Emission (1 ms) = 6.0%.

Post-ignition rise-times required for peak formation of OH* (radical pool population) were recorded as a function of temperature (Fig. 16) relative to the point of ignition and varied over a relatively narrow range of 97 μs showing an expected, albeit slight, temperature dependence where, at 1478 K, 105 μs was required to fully populate the radical pool and at 1309 K, 202 μs elapsed for the population. A statistical outlier of 335 μs measured at 1341 K is present, yet post-ignition rise-times of the species displayed an inverse relationship to temperature.

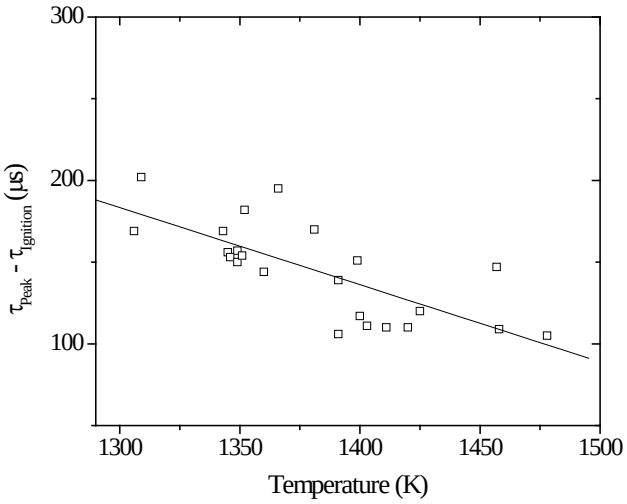

Fig. 16. Post-ignition rise-times to peak OH* yield for $0.001C_9H_{20} + 0.028O_2 + 0.971Ar$ ($\phi = 0.5$) at P = 1.5 atm.

5.2.2 Stoichiometric OH behavior*

Similar to the measurements at the fuel-lean condition, OH* species time-histories were smooth and showed no significant change in behavior during production or consumption. A symmetric trend was observed for higher temperatures up to approximately 1530 K, however with decreasing temperature the profiles became increasingly asymmetric with a steeper slope of consumption compared to that of production. Only slight primary /secondary rate-of-consumption behavior was exhibited under the conditions studied, primarily at lower temperatures (< 1430 K). Pre-ignition OH* formation was present in 13 of the 16 profiles, becoming evident at temperatures greater than 1430 K. For measurements where ignition delay times were less than 100 μs, the pre-ignition OH* profile was sustained to the point of ignition as insufficient time was available for the zero-concentration level to be re-attained (Fig. 17); the result of the pre-ignition behavior having a duration which overlaps ignition. At lower temperatures, below 1400 K, the pre-ignition phenomenon is nonexistent (Fig. 18).

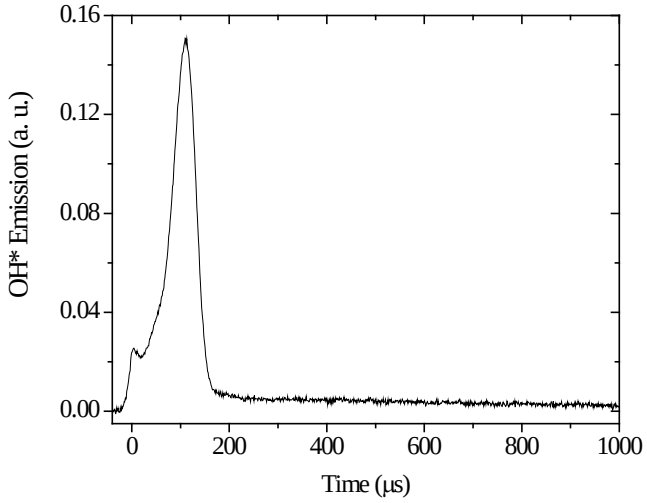

Fig. 17. Pre-ignition OH* formation overlapping with ignition event. $\tau_{Ignition}$ = 54 μs, T = 1591 K, P = 1.37 atm.

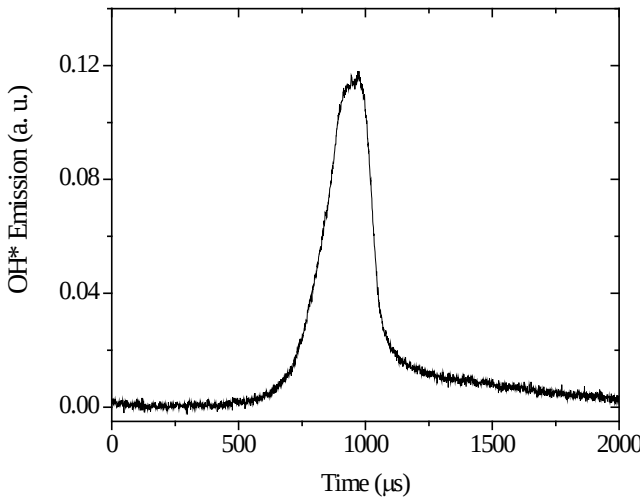

Fig. 18. OH* species time-history. $\tau_{Ignition}$ = 729 μs, T = 1402 K, P = 1.61 atm.

For conditions under which the pre-ignition profile was present, increased temperature was seen to increase the size (peak OH* yield) relative to the main peak resulting from ignition. The relative percentage (pre-ignition peak height relative to peak height resulting from ignition) varied from 2.5% at a temperature of 1434 K to 16.7% at an elevated temperature of 1591 K. The durations of the pre-ignition peaks were similar to those seen in the fuel-lean condition, although different qualitative behavior was observed. Under conditions where the pre-ignition profile was not measurable due to interaction with the ignition event, two behaviors were seen: (1) zero-concentration level of OH* was not reattained, leaving a small, yet measurable quantity of OH* present in the shock tube prior to ignition, (2) pre-ignition OH* concentration was sustained up to the point of ignition. In the latter case, the OH radical pool initiates, reaches a pre-ignition maximum, then begins to decrease where it meets the main ignition event. The time of initiation of the pre-ignition phenomena was shortened, relative to that for the fuel-lean condition and displayed a temperature dependence whereby higher temperature resulted in an earlier initiation of pre-ignition OH* chemistry. Initiation times ranged from 32 μs at a temperature of 1434 K to 24 μs at a temperature of 1591 K. Measurements of post-ignition rise times for ϕ = 1.0 mixtures show a moderate dependence on temperature, ranging from 99 μs at 1591 K to 284 μs at 1402 K (Fig. 19).

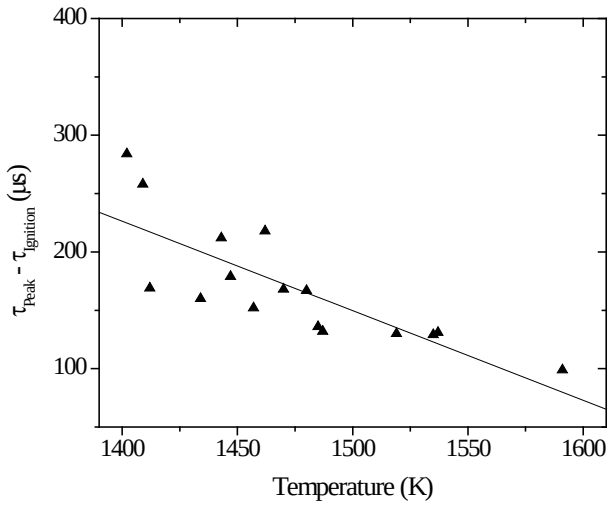

Fig. 19. Post-ignition rise-times to peak concentration for $0.001C_9H_{20} + 0.014O_2 + 0.985Ar$ (ϕ = 1.0) at P = 1.5 atm.

5.2.3 Fuel-rich OH behavior*

Under fuel-rich conditions, no change in rates of consumption was present. Upon ignition and ensuing consumption of OH*, the concentration rapidly approached a zero-level. A prominent distinction in the fuel-rich OH* chemistry is the width of the main OH* profile resulting from ignition. In the previous two conditions, profiles were considerably thinner, particularly at higher temperatures. For ϕ = 2.0, at all temperatures, profile widths exceeded several hundred microseconds. In previous (fuel-lean and stoichiometric) cases, this behavior was displayed at lower temperatures with an upper limit of approximately 300 μs seen in the ϕ = 1.0 condition. At a temperature of 1412 K with an ignition delay of 964 μs, the duration of the main OH* profile from ignition subsisted for a lower limit of approximately 500 μs approaching 900 μs as an upper limit (Fig. 20). Another salient trait to fuel-rich OH* profiles is a substantial increase in pre-ignition phenomena. The behavior was exhibited in 13 of the 14 measurements and achieved a higher level of peak yield relative to both the zero-concentration level and to the maximum OH* yield post-ignition. A temperature dependence was revealed, however the dependence is less than in the previous two equivalence ratios where pronounced pre-ignition peak behavior was shown for ignition delay times less than 200 μs (ϕ = 1.0) or less than 100 μs (ϕ = 0.5). For ϕ = 2.0, a marked increase in pre-ignition behavior measured for ignition delay times as long as 800 μs.

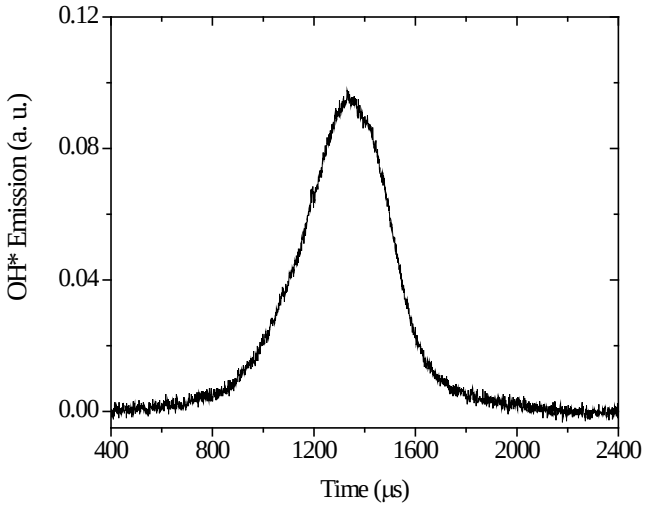

Fig. 20. OH* species time-history. T = 1412 K, P = 1.50 atm, $\tau_{Ignition}$ = 964 μs, $\tau_{Peak-Ignition}$ = 422 μs.

Relative to the main OH* peak, the pre-ignition profile attained higher percentages and showed a strong temperature-dependence. At a lower temperature of 1443 K, the pre-ignition profile reached a maximum value 11.4% of the maximum OH* yield resultant from ignition. At higher temperatures, the value increased dramatically. For a temperature of 1543 K, the pre-ignition peak reached 36.9% of the value of OH* formed by the ignition event. Figure 21 shows OH* formation and consumption at 1555 K where the pre-ignition peak is 28.8% of peak OH* concentration. Durations for pre-ignition profiles were amenable for 12 of the 14 measurements. No significant deviations from previous conditions were noted. The initiation of the pre-ignition events, however, formed a trend: decreasing time-of-initiation with increasing equivalence ratio. A range of times at which pre-ignition behavior is first observable from 33 μs at 1443 K to 22 μs at 1555 K was evidenced. Post-ignition rise-times for the fuel-rich experiments presented substantial scatter (Fig. 22) such that a general behavioral trend was unattainable.

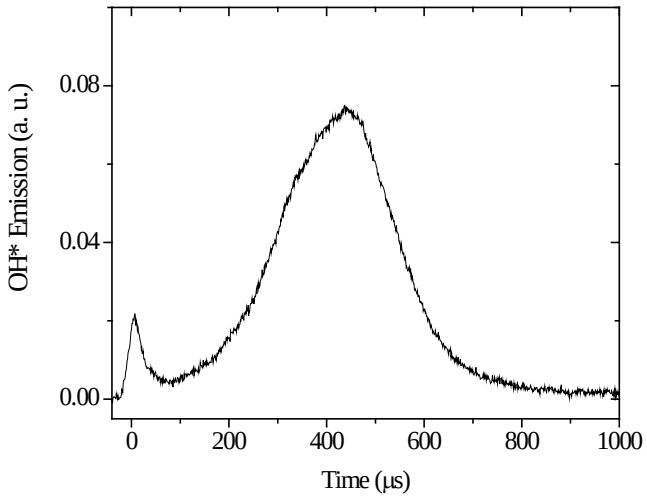

Fig. 21. OH* species time-history. T = 1555 K, P = 1.53 atm, $\tau_{Ignition}$ = 181 μs, $\tau_{Peak - Ignition}$ = 301 μs. Pre-ignition peak measured at 28.8% of the peak OH* formation.

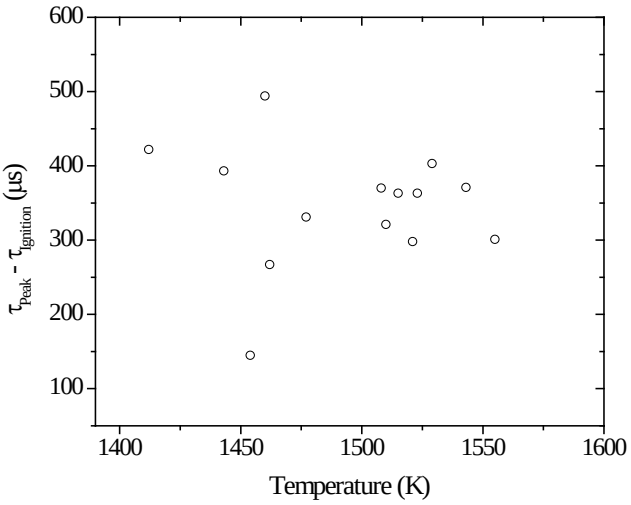

Fig. 22. Post-ignition rise-times to peak concentration for $0.001C_9H_{20} + 0.007O_2 + 0.992Ar$ ($\phi = 2.0$) at P = 1.5 atm.

*5.3 Pre-ignition formation and depletion of OH**

A pre-ignition behavior in OH* profiles was detected under all equivalence ratios studied, at temperatures as low as 1400 K, where a small, yet measurable formation of OH* was present prior to the point of ignition. The profiles took on a parabolic, symmetric shape and characteristics of these pre-ignition peaks include a significant dependence on equivalence ratio – increasing in relative percentage of the total OH* concentration with increasing fuel concentration (equivalence ratio), a dependence on temperature, statistically consistent duration times, and a temperature-dependent time of initiation within the high-temperature, quiescent conditions created by the reflected-shock wave. Each of these phenomena was quantified in order to correlate dependencies and elucidate the chemistry of this behavior. The most significant observation is that of the growth of the pre-ignition peaks with increasing equivalence ratio. Calculations were performed to quantify the percentage of the pre-ignition profile height relative to that of the main peak height resultant from combustion which can provide a metric for kinetic relevance. Signal outputs from the photomultiplier emission detector were plotted, and maximum values of each profile were recorded.

The signal indicating peak OH* production from ignition ($y_{max.}$) is used as the maximum (reference) value, measured relative to the baseline zero-level of concentration. A second value, obtained from the peak of the pre-ignition profile is then determined (y_0). A peak-to-peak percentage was then calculated (Fig. 23) as a measure of the relative production of OH* in both the pre-ignition and main ignition regimes.

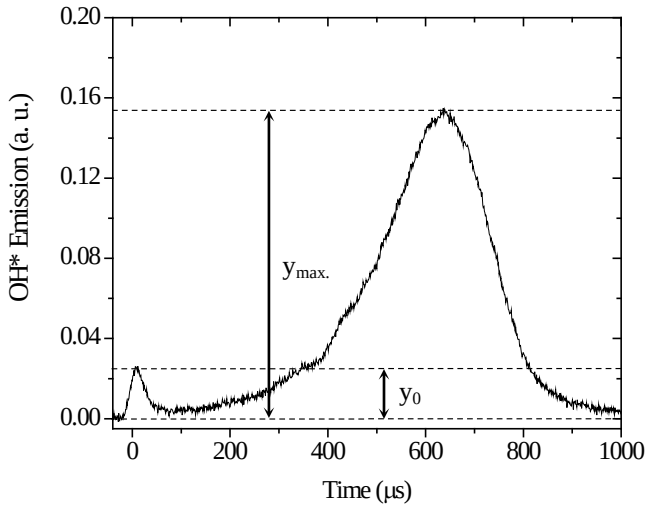

Fig. 23. Terms for definition of signal percentages for pre-ignition peak behavior. OH* measurement for $0.001C_9H_{20} + 0.007O_2 + 0.992Ar$ ($\phi = 2.0$), T = 1521 K, P = 1.49 atm. Pre-ignition peak initiates at 27 μs after reflected-shock formation, 67 μs in duration. The height of the peak is 16.2% of that for the main peak marking ignition.

Percentage of signal measured from pre-ignition peak relative to the peak in the ignition profile is calculated:

$$\%_{Peak-Peak} = \left[1 - \left(\frac{y_{max.} - y_0}{y_{max.}}\right)\right] \cdot 100$$

Results from pre-ignition calculations for each equivalence ratio are shown in Table 4.

Table 4. Relative percentages of peak-to-peak OH* yield. The peak of the pre-ignition profile is shown to take on a larger percentage relative to peak OH* yield from ignition with increasing temperature and equivalence ratio. Initiation times (t) of pre-ignition peaks are defined relative to time-zero (t_0).

Stoichiometry	T (K)	$\%_{Peak\text{-}Peak}$	Pre-Ignition Profile Duration (μs)	t - t_0 (μs)
	1399	3.4	63	36
	1425	1.8	80	37
ϕ = 0.5	1457	2.1	Sustained to ignition	34
	1458	3.5	Sustained to ignition	33
	1478	3.5	Sustained to ignition	35
	1434	2.5	80	32
	1443	3.4	55	31
	1447	2.6	63	37
	1457	4.3	Zero not reattained	28
	1462	6.8	66	28
	1470	3.7	69	29
ϕ = 1.0	1480	4.5	58	30
	1485	5.6	Zero not reattained	28
	1487	5.3	69	29
	1519	5.5	Zero not reattained	26
	1535	8.7	Sustained to ignition	26
	1537	11.3	Sustained to ignition	26
	1591	16.7	Sustained to ignition	24
	1443	11.4	74	33
	1454	25.9	68	24
	1460	15.7	74	27
	1462	11.9	74	27
	1477	15.0	73	27
	1508	20.4	80	22
ϕ = 2.0	1510	17.1	92	23
	1515	28.5	77	25
	1521	16.3	67	27
	1523	22.3	72	21
	1529	30.6	Zero not reattained	26
	1543	36.9	69	30
	1555	28.8	Zero not reattained	22

Aside from a temperature dependence of the pre-ignition peaks, which under each equivalence ratio caused an increase in pre-ignition peak height, the behavior showed a significant dependence on the degree of stoichiometry, detectable in the fuel-lean, stoichiometric, and fuel-rich OH* profiles. In some of the fuel-lean cases, pre-ignition curves show an increased level over those in the stoichiometric cases, which is to be expected due to the higher concentration of O_2 present in the system. However, relative to the main ignition peak a significant dependence on fuel concentration is shown, where peak-to-peak relative percentages increase with increasing equivalence ratio (Fig. 24).

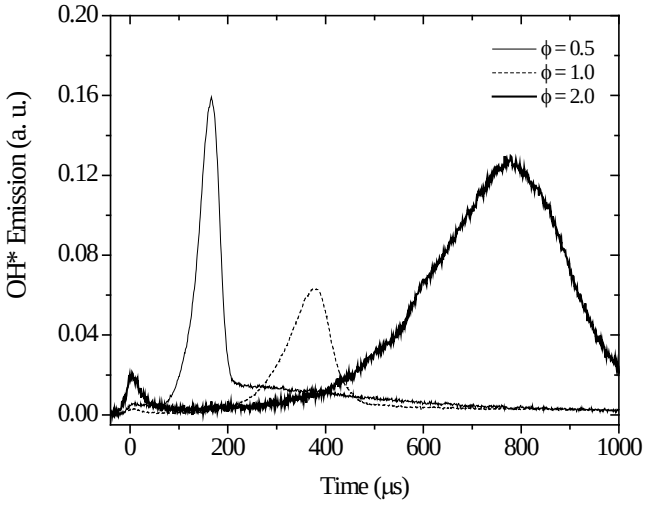

Fig. 24. OH* emission at T = 1478 K, P = 1.52 atm. Pre-ignition peaks show dependence on stoichiometry. Peak-to-peak percentages for ϕ = 0.5, 1.0, and 2.0 are 3.5%, 4.5%, and 15.0%, respectively.

The time interval over which the pre-ignition OH* pool was populated and depleted was measured to infer any dependencies. The behavior showed to be within an interval of time of 37 μs from a lower limit 55 μs to an upper limit of 92 μs, however owing to a large variation with temperature no consistent dependence is noted. Due to the pre-ignition peak formation in only the higher temperature fuel-lean experiments, statistics calculated for the ϕ = 0.5 condition case suffer from a small sample size (N = 2) where peak duration was measurable and a corresponding relative higher standard deviation. Statistical mean and standard deviation for each equivalence ratio are shown in Table 5.

Table 5. Pre-ignition peak duration statistics.

ϕ	Mean Duration Time (μs)	Standard Deviation (μs)
0.5	71	12
1.0	66	8
2.0	74	7

The point in time once the reflected-shock conditions were formed that the pre-ignition OH* initiated displayed both a temperature- and stoichiometry-dependence. For a given equivalence ratio, the parameter decreased with increasing temperature, thus for higher temperature reactions pre-ignition OH* formed earlier than at lower temperatures. Further, the initiation time parameter decreased with increasing equivalence ratio with the longest initiation times existing in the fuel-lean condition and the shortest times occurring in the fuel-rich condition (Table 6).

Table 6. Pre-ignition OH* initiation statistics.

ϕ	Mean Initiation Time (μs)	Standard Deviation (μs)
0.5	35	2
1.0	29	3
2.0	26	3

Pre-ignition peak initiation times were plotted as a function of temperature (Fig. 25). Trend lines calculated for each equivalence ratio show decreasing time-of-initiation with increasing temperature and increasing equivalence ratio. The time of initiation of the pre-ignition phenomenon for the stoichiometric condition was shortened, relative to that for the $\phi = 0.5$ condition and displayed a dependence whereby higher temperature resulted in an earlier initiation of pre-ignition OH* chemistry. Stoichiometric pre-ignition OH* initiation times ranged from 32 μs at a temperature of 1434 K to 24 μs at a temperature of 1591 K. The $\phi = 2.0$ condition, despite an apparent high degree of experimental scatter, yielded initiation times which were slightly lower than for $\phi = 1.0$, thereby possessing the shortest initiation times of the equivalence ratios studied over the entire range of temperature for pre-ignition behavior.

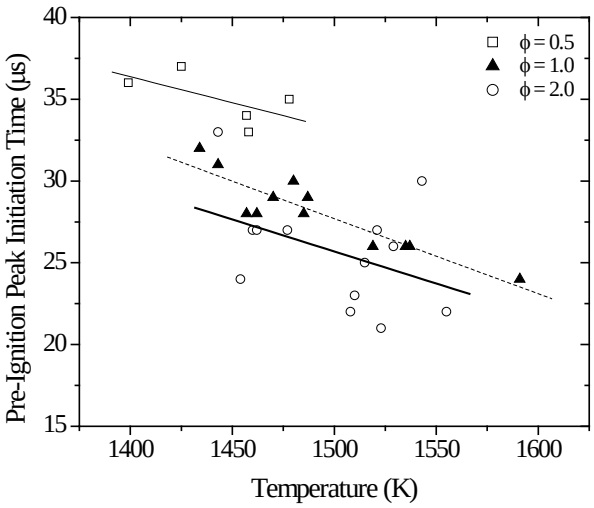

Fig. 25. Pre-ignition peak initiation times. Dependence is observed both on temperature (decreasing with increasing temperature) and equivalence ratio.

5.4 Ignition delay time measurements of n-nonane in O_2-Ar

Upon reflection of the incident shock wave off of the shock-tube endwall, a reflected shock wave forms and passes through the reactive C_9H_{20}-O_2-Ar mixture creating a high-temperature, quiescent (test) region within which the fuel and oxidizer can react. Inside of the test region, thermal energy generated from the shock wave is absorbed by the energy storage modes of each species (translational, rotational, vibrational, electronic) causing chemical bonds to weaken and eventually cause dissociation. The interval of time, unique to the mixture composition, temperature and pressure, existing between the formation of the reflected shock and sharp increase in emission and /or pressure is defined as the ignition delay time of the given mixture under the given set of thermodynamic conditions, the reflected-shock temperature and pressure (Fig. 11). The method of steepest ascent applied to measured sidewall emission profiles of OH* radicals is utilized herein to report ignition delay times.

Ignition delay times are plotted using a logarithmic scale (ordinate) as a function of inverse temperature (abscissa), thus increasing temperature occurs from the right to left. Logarithmic scales are routinely used to report ignition delay time data such that the behavior can be described using a linear relation, constructed using empirical equations of Arrhenius form. In the physical sense, ignition delay times commonly form an exponential dependence on inverse temperature. The activation energy of a mixture is

defined qualitatively as the energy required for chemical reaction to take place or, in a quantum mechanical sense the energy required to bring species in the reactive mixture above respective potential energy barriers. Recall the form of the Arrhenius expression for the temperature dependence of reaction rate constants:

$$k = Aexp\left(\frac{-E_A}{R_u T}\right)$$

or,

$$\ln k = -\frac{E_A}{R_u}\left(\frac{1}{T}\right) + Constant$$

where,

k ≡ Rate constant (s^{-1})

E_A ≡ Activation energy (kcal /mol)

R_u ≡ Universal gas constant (kcal /mol · K)

T ≡ Temperature (K)

In terms of an ignition delay time, noting the inversion of the natural log parameter:

$$\ln \tau = \frac{E_A}{R_u}\left(\frac{1}{T}\right) + Constant$$

Using the distributed ignition data (ln $\tau_{Ignition}$ – 1 /T), the above equation takes on linear form (y = mx + b), where E_A/R_u is the slope and inverse temperature is the abscissa. From this expression, a numeric value for the slope (m) of the linear trend is determined, from which then the activation energy is calculated through multiplication by the universal gas constant R_U = 1986 kcal /mol · K. An increased activation energy implies that a mixture is less reactive at a given temperature than another mixture with lower E_A.

An imposed test time limitation of 1 ms in the shock-tube facility utilized to conduct the species profile measurements coupled with mixture ignitability dictate the range of temperatures covered in the experimental set. Measurements of ignition delay times were made over the temperature range 1285 < T (K) < 1478 for the ϕ = 0.5 condition, 1402 < T (K) < 1591 for the ϕ = 1.0 condition, and 1443 < T (K) < 1555 for the ϕ = 2.0 condition, with each reaction pressure for all equivalence ratios maintained near 1.5 atm. For the ϕ = 0.5 condition (Fig. 26), ignition delay times based on OH* emission ranged from 107 μs at 1478 K to 1104 μs at 1285 K where the data are fit by a linear trend (R^2 = 0.97). Calculations reveal an activation energy for the ϕ = 0.5 mixture E_A of 44.2 kcal /mol (185.0 kJ /mol).

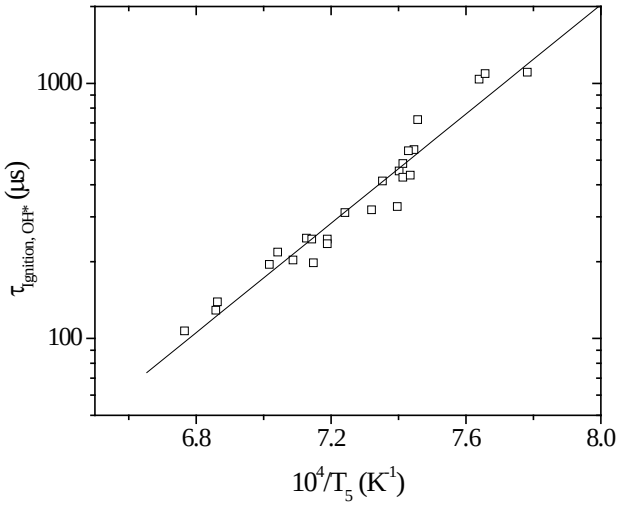

Fig. 26. Ignition delay times for $0.001C_9H_{20} + 0.028O_2 + 0.971Ar$ ($\phi = 0.5$) at P = 1.5 atm.

Measurements of stoichiometric ignition delay times (Fig. 27) spanned from 54 μs at 1591 K to 729 μs at 1402 K where the data are fit by a linear trend ($R^2 = 0.98$). Activation energy calculations were carried out for $\phi = 1.0$ an E_A of 56.0 kcal /mol (234.5 kJ /mol).

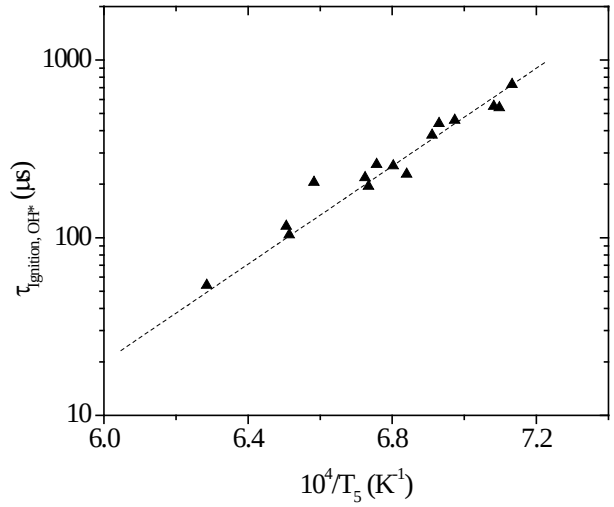

Fig. 27. Ignition delay times for $0.001C_9H_{20} + 0.014O_2 + 0.985Ar$ ($\phi = 1.0$) at P = 1.5 atm.

For the fuel-rich condition, ignition times (Fig. 28) were measured from 1412 K (964 μs) to 1555 K (181 μs) with a linear fit $R^2 = 0.96$. The slope of the linear fit, multiplied by the universal gas constant gives an E_A of 51.1 kcal /mol (213.9 kJ /mol).

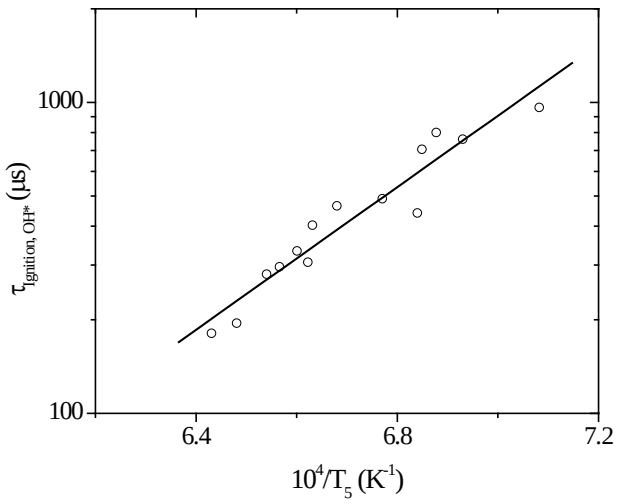

Fig. 28. Ignition delay times for $0.001C_9H_{20} + 0.007O_2 + 0.992Ar$ ($\phi = 2.0$) at P = 1.5 atm.

Combustion and ignition of the fuel-lean condition yielded the shortest ignition times over the entire range of temperature covered, followed by those of the stoichiometric condition, and lastly by the fuel-rich condition which measured the longest ignition times at each temperature. Activation energies were calculated from ignition trends for each mixture and shown in Table 7.

Despite having prolonged time of ignition relative to the $\phi = 1.0$ condition, the fuel-rich trend produced an activation energy 9% lower than that of the $\phi = 1.0$ trend, observable in the trends noting that as colder temperatures are reached, an approach toward intersection becomes apparent due to the steeper $\phi = 1.0$ slope. The behavior may be rationalized by considering the system at high temperatures with less oxygen/more fuel present, lengthening the time for the radical pool to populate. This trend is evidenced in each of the fuel-rich OH* profiles which at all temperatures produced a more moderate rate of hydroxyl radical production. Each equivalence-ratio-based data set contains measurements from two independent mixtures, and excellent repeatability is shown by overlapping ignition times at several temperatures for

each set. Repeatability is of particular importance for the present experiments conducted due to the properties of the n-nonane fuel, namely its low vapor pressure at standard temperature and pressure (STP).

Table 7. Calculated activation energies.

ϕ	Diluent	E_A (kcal /mol)
0.5	97.1% Ar	44.2
1.0	98.5% Ar	56.0
2.0	99.2% Ar	51.1

5.5 Empirical ignition delay time correlation

An empirical correlation for determining ignition delay times for n-C_9H_{20}/O_2/Ar mixtures as a function of molar concentrations and temperature was constructed for the data set totaling 61 measurements. Rates of chemical reaction following Arrhenius behavior can be described using the product of the frequency factor (A) and an exponential term involving the activation energy (E_A) and temperature (T):

$$k = A' exp\left(\frac{-E_A}{R_u T}\right)$$

A similar expression can be formed with ignition delay times plotted in the same manner as reaction rates ($\log_{10} - 1/T$), where $A \neq A'$:

$$\tau = A[Fuel]^x [Oxidizer]^y [Third\ Body\ /Inert]^z exp\left(\frac{E_A}{R_u T}\right)$$

Differing in slope, each set of ignition data (ϕ = 0.5, 1.0, 2.0) varied linearly with inverse temperature when plotted logarithmically. The method of least squares was applied to the complete data set in order to calculate statistics describing a common linear trend. Taking the natural logarithm of the above relation yields an equation describable by a linear function:

$$\ln(\tau) = \ln(A) + xln[Fuel] + yln[Oxidizer] + zln[Third\ Body\ /Inert] + \left(\frac{E_A}{R_u}\right)T$$

The pre-multipliers x, y, z, and E_A/R_u represent respective slopes for each term, and the $\ln(A)$ term represents the constant (y-intercept). Solution of these parameters is reached using the method of least squares and after taking the exponential of the relation, an equation describing the complete ignition data set as a function of species concentration (mol /m^3) and temperature is determined:

$$\tau\ (\mu s) = 4.01789 \cdot 10^{-5}[\mathrm{C_9H_{20}}]^{1.65}[\mathrm{O_2}]^{-4.10}[\mathrm{Ar}]^{3.95} exp\left(\frac{19228.23}{\mathrm{T}}\right)$$

The ignition delay time correlation fit the entire data set well (R^2 = 0.94). Positive exponents (x, z) imply that an increase in concentration of species with such coefficients will lead to an increase in τ_{Ignition}, conversely a negative exponent (y) indicates that the ignition delay time will correspondingly decrease when the concentration is decreased since the parameter is inversely proportional to the species concentration raised to a negative power. Reproduction of the calculated ignition times using the above correlation ($\tau_{\mathrm{Correlation}}$) relative to experimental ignition delay times ($\tau_{\mathrm{Experimental}}$) show good agreement (Fig. 29). A pressure exponent derived from the correlation of n = 1.5 results. Typical for pressure exponents for n-alkanes is a range between –0.50 and –0.90. A second correlation was made in which the inert was removed. The resulting pressure exponent was n = –0.53 and the equation is given:

$$\tau\ (\mu s) = 0.06721[\mathrm{C_9H_{20}}]^{-0.60209}[\mathrm{O_2}]^{0.06721} exp\left(\frac{28219.95}{\mathrm{T}}\right)$$

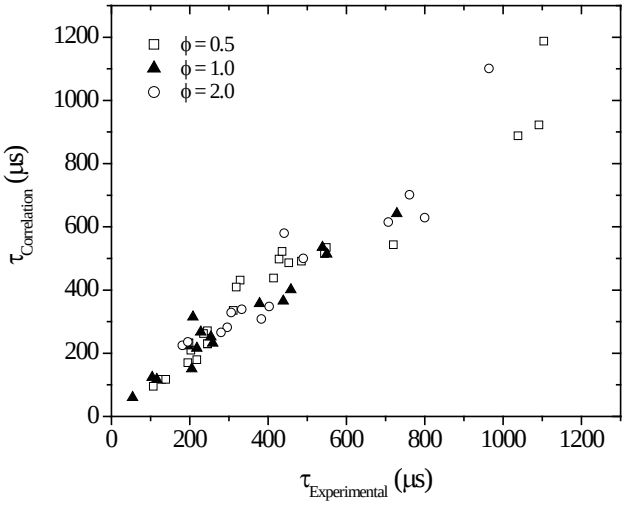

Fig. 29. Ignition delay times for each equivalence ratio calculated using the empirical correlation and compared to experimental ignition times. Ignition times plotted with the correlation were determined using conditions from each experiment.

From the correlation, E_A = 38.2 kcal /mol (159.9 kJ /mol). Experimental ignition data for n-nonane (C_9H_{20}) are not available in the literature, thus a comparison of activation energy is not possible. However, octane (C_8H_{18}) and decane ($C_{10}H_{22}$) ignition data are abundant. Activation energy is a pressure-dependent parameter, and while E_A additionally shows a dependence on the particular type of fuel as well as the fuel concentration, results for activation energy are compared for reference against the two alkanes. For a 0.5% fuel concentration, Davidson et al.[62] report an activation energy for iso-octane of 43.9 kcal /mol for ignition times at 1.3 atm. Oehlschlaeger et al. measured ignition delay times for iso-octane over a range of fuel concentrations (0.01% – 0.50%) at pressures near 1.5 atm and through calculation of an overall ignition correlation recorded an activation energy of 44.8 kcal /mol.[45] Decane is reported to have an activation energy of 34.2 kcal /mol for ignition times measured from 1.8 to 10 atm with fuel concentration ranging from 0.49% – 1.50%.[68] From the observations inferred on alkanes of next higher and lower order relative to nonane (decane and octane, respectively) the calculated activation energy falls in between those values for the higher- and lower-order alkanes.

5.6 Effect on temperature of small rise in pressure during experiment

Resulting from adverse gas dynamic effects in the shock tube, the pressure was observed to rise slightly behind the reflected-shock over the timeframe of the experiment. Considering the most severe case where this behavior was seen, the increase in pressure is small, reaching a maximum deviation of only ~ 0.14 psi (0.0096 atm) at a time of 1018 μs (20 μs prior to ignition), yet its effect on the reaction temperature was taken into account to elucidate the potential for issues with reported ignition data. The rise in pressure is gradual, and in terms of pressure per unit time, the increase was at a typical rate of $1.7 \cdot 10^{-4}$ atm /100 μs. It is important to note that the majority of ignition data was measured well below 1.2 ms, however a few measurements were taken near this value and as such, the case in which one of the longer ignition times is delineated as a worst-case condition.

The compression process behind the reflected-shock wave is approximated as isentropic to calculate the increase in temperature from the associated rise in pressure. The shock process is adiabatic due to small timescales, yet is highly non-isentropic, however the assumption holds as a guide to reporting changes in experimental conditions. Assuming ideal gas,

$$\frac{T_{5,s}}{T_5} = \left(\frac{P_5^{'}}{P_5}\right)^{\frac{\gamma-1}{\gamma}}$$

where,

$T_{5,s}$ ≡ Isentropic temperature behind reflected shock (K)

T_5 ≡ Reflected-shock temperature (K)

$P_5^{'}$ ≡ Pressure at t = $\tau_{Ignition}$ – 20 μs (atm)

P_5 ≡ Reflected-shock pressure (atm)

γ ≡ Specific heat ratio within reflected-shock region

For the ϕ = 0.5 condition, an ignition delay time of 1038 μs was recorded for a reflected-shock temperature and pressure of T_5 = 1309 K and P_5 = 1.62 atm, respectively (Fig. 30). Using thermodynamic conditions calculated for the test region, the temperature is shown to increase isentropically to 1342 K, an increase of 33 K over T_5. Since the process is gradual, the impact on ignition data is taken using an average value of temperature increase. In the present, limiting case the average temperature is 1326 K. The change in temperature slightly impacts the longer ignition delay time (Fig. 31). A time of 20 μs prior to

ignition is taken to be the point at which the increase in temperature is experienced by the reactants to allow time for the vibrational relaxation period of the reactant molecules (n-C_9H_{20} and O_2).

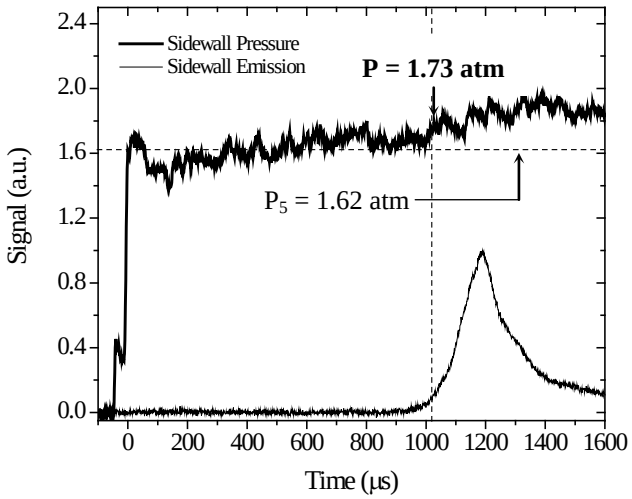

Fig. 30. Pressure-rise occurs due to the interaction of the boundary layer with the gas behind the reflected shock wave. At long ignition times, the pressure effect was calculated to reveal the corresponding rise in temperature using ideal-gas isentropic relations. A calculated reflected-shock pressure of 1.62 atm rose to a peak 1.84 atm at a time shortly after ignition.

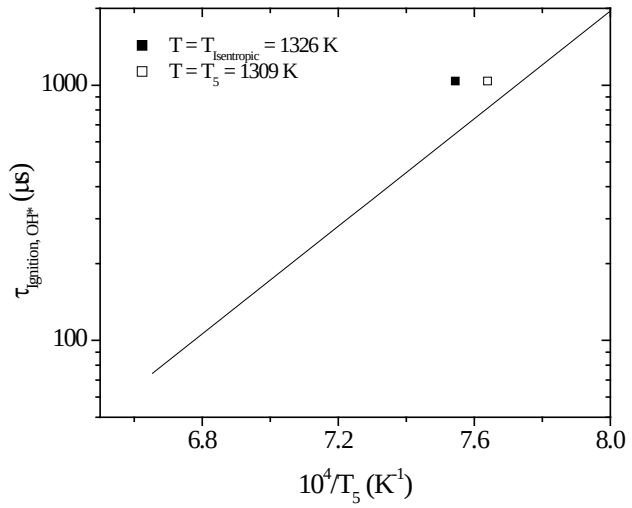

Fig. 31. A deviation results at long ignition delay times due to adverse gas dynamic imposing a gradual rise in pressure behind the reflected-shock with time.

6. SUMMARY

n-Nonane combustion data have been recorded for first time in a shock tube. Fundamental combustion measurements of n-nonane highly diluted in argon were made at three levels of equivalence ratio (ϕ = 0.5, 1.0, 2.0) behind reflected shock waves where the level of argon dilution varied from 97.1% Ar (ϕ = 0.5) to 98.5% Ar (ϕ = 1.0) to 99.2% Ar (ϕ = 2.0). Species time-histories of excited hydroxyl (OH*) radicals were measured using chemiluminescence and recorded on μs timescales over a wide range of temperature, 1285 < T (K) < 1627, using shock speeds from 0.736 mm/μs to 0.831 mm /μs. To attain the experimental conditions behind the reflected-shock wave, initial pressures of the reactive mixture were varied from 50.2 torr to 31.5 torr, resulting in reaction pressures near 1.5 atm.

Due to the diminutive amount of energy release in dilute mixtures, ignition delay times were extracted from sidewall-measured species time-histories using the method of steepest ascent. Ignition data plotted on a logarithmic-linear scale ($\tau_{Ignition}$ – 1/T) provided for calculation of activation energies for each equivalence ratio as the data took on Arrhenius form. The stoichiometric condition (ϕ = 1.0) had ignition times ranging from 729 μs (1402 K) to 54 μs (1591 K) and yielded the highest activation energy of 56.0 kcal/mol (234.5 kJ/mol). The fuel-rich condition (ϕ = 2.0) recorded the second highest activation energy with E_A = 51.1 kcal/mol (213.9 kJ /mol) resulting from ignition times ranging from 964 μs (1412 K) to 181 μs (1555 K), and the fuel-lean (ϕ = 0.5) condition measured the lowest activation energy at E_A = 44.2 kcal /mol (185.0 kJ /mol) resulting from ignition times ranging from 1104 μs (1285 K) to 107 μs (1478 K).

Pre-ignition formation of OH* existed at higher temperatures (T > 1400 K) in each equivalence ratio. Equivalence ratio influenced the time at which pre-ignition occurred and also displayed a temperature-dependence, occurring earlier at higher temperatures and higher fuel-to-oxygen concentrations. The profile of pre-ignition appeared parabolic in shape, lasting several tens of microseconds in duration, and the peak level of pre-ignition OH* also showed a strong dependence on both temperature and equivalence ratio. Beyond 1400 K, the peak of the pre-ignition OH* profile significantly increased in relative percentage to that of the main peak OH* formation resulting from ignition. Further, extending to higher equivalence ratios showed that the pre-ignition behavior is strongly influenced by ϕ. Pre-ignition OH* peaks measured 16.7% of maximum OH* yield for the ϕ = 1.0 condition and a higher 36.9% for the ϕ = 2.0 condition. Early radical-pool population to this extent could have an impact on incipient chemical kinetic processes which further dictate ignition and other combustion phenomena.

REFERENCES

[1]Lamprecht, D., "Fischer-Tropsch Fuel for Use by the U.S. Military as Battlefield-Use Fuel of the Future," *Energy & Fuels*, Vol. 21, 2007, pp. 1448-1453.

[2] Edwards, T. and Maurice, L., "Surrogate Mixtures to Represent Complex Aviation and Rocket Fuels," *35th AIAA /ASME /SAE /ASEE Joint Propulsion Conference and Exhibit*, AIAA Paper 1999-2217, 1999, pp. 1-11.

[3]Gupta, A. K. and Lilley, D. G., "Combustion and Environmental Challenges for Gas Turbines in the 1990's," *Journal of Propulsion and Power*, Vol. 10, No. 2, 1994, pp. 137-147.

[4]Ghassemi, M., Iyer, R., Scofield, R., and McSorley, J., "Effects of Synfuel Use," *Engineering Science & Technology*, Vol. 15, No. 8, 1981, pp. 866-873.

[5]Longwell, J. P., "Synthetic Fuels and Combustion," *Progress in Energy and Combustion Science*, Vol. 3, 1977, pp. 127-138.

[6]Schulz, H., "Short History and Present Trends of Fischer-Tropsch Synthesis," *Applied Catalysis A: General*, Vol. 186, 1999, pp. 3-12.

[7]Maurice, L. Q., Lander, H., Edwards, T., and Harrison, W. E., "Advanced Aviation Fuels: A Look Ahead via a Historical Perspective," *Fuel*, Vol. 80, 2001, pp. 747-756.

[8]Bacha, J., Barnes, F., Franklin, M., Gibbs, L., Hemighaus, G., Hogue, N., Lesnini, D., Lind, J., Maybury, J., and Morris, J., "Aviation Fuels," *Chevron Products Company Technical Review*, 2000, pp. 1-87.

[9]Witcofski, R. D., "Alternate Aircraft Fuels – Prospects and Operational Implications," NASA Langley Research Center, TM-X-7403C, May, 1977, pp. 1-39.

[10]Edwards, T., Minus, D., Harrions, W., Corporan, E., DeWitt, M., Zabarnick, S., and Balster, L., "Fischer-Tropsch Jet Fuels – Characterization for Advanced Aerospace Applications," AIAA Paper 2004-3885, *40th AIAA /ASME /SAE /ASEE Joint Propulsion Conference and Exhibit*, 2004, pp. 1-13.

[11]Johnson, J. W., Berlowitz, P. J., Ryan, D. F., Wittenbrink, R. J., Genetti, W. B., Ansell, L. L., Kwon, Y., and Rickeard, D. J., "Emissions from Fischer-Tropsch Diesel Fuels," SAE Technical Paper 2001, pp. 1675-1685.

[12]Lapuerta, M., Armas, O., and Rodríguez-Fernández, J., "Effect of Biodiesel Fuels on Diesel Engine Emissions," *Progress in Energy and Combustion Science*, Vol. 34, 2008, pp. 198-223.

[13]Leckel, D., "Diesel Production from Fischer-Tropsch: The Past, the Present, and New Concepts," *Energy & Fuels*, Vol. 23, 2009, pp. 2342-2358.

[14]Cooney, C. P., Yeliana, Worm, J. J., and Naber, J. D., "Combustion Characterization in an Internal Combustion Engine with Ethanol – Gasoline Blended Fuels Varying Compression Ratios and Ignition Timing," *Energy & Fuels*, Vol. 23, 2009, pp. 2319-2324.

[15]Zhang, H. R., Eddings, E. G., and Sarofim, A. F., "Criteria for Selection of Components for Surrogates of Natural Gas and Transportation Fuels," *Proceedings of the Combustion Institute*, Vol. 31, 2007, pp. 401-409.

[16]Andrae, J.C.G., "Development of a Detailed Kinetic Model for Gasoline Surrogate Fuels," *Fuel*, Vol. 87, 2008, pp. 2013-2022.

[17]Lenhert, D. B., Miller, D. L., and Cernansky, N. P., "The Oxidation of JP-8, Jet-A, and Their Surrogates in the Low and Intermediate Temperature Regime at Elevated Pressures," *Combustion Science and Technology*, Vol. 179, 2007, pp. 845-861.

[18]Violi, A., Yan, S., Eddings, E. G., Sarofim, A. F., Granata, S., Faravelli, T., and Ranzi, E., "Experimental Formulation and Kinetic Model for JP-8 Surrogate Mixtures," *Mediterranean Combustion Symposium*, Sharm El Sheik, Egypt, January 2002.

[19]Dagaut, P., Bakali, A., and Ristori, A., "The Combustion of Kerosene: Experimental Results and Kinetic Modeling Using 1- to 3-Component Surrogate Model Fuels," *Fuel*, Vol. 85, 2006, pp. 944-956.

[20]Colket, M., Edwards, T., Williams, S., Cemansky, N. P., Miller, D. L., Egolfopoulos, F., Lindstedt, P., Seshadri, K., Dryer, F. L., Law, C. K., Friend, D., Lenhert, D. B., Pitsch, H., Sarofim, A., Smooke, M., and Tsang, W., "Development of an Experimental Database and Kinetic Models for Surrogate Jet Fuels," AIAA Paper, Aerospace Sciences Meeting, 2007, pp. 1-21.

[21]Hamosfakidis, V. and Reitz, R.D., "Optimization of a Hydrocarbon Fuel Ignition Model for Two Single Component Surrogates of Diesel Fuel," *Combustion and Flame*, Vol. 132, 2003, pp. 433-450.

[22]Humer, S., Frassoldati, A., Granata, S., Faravelli, T., Ranzi, E., Seiser, R., and Seshadri, K., "Experimental and Kinetic Modeling Study of Combustion of JP-8, Its Surrogates and Reference Components in Laminar Nonpremixed Flows," *Proceedings of the Combustion Institute*, Vol. 31, 2007, pp. 393-400.

[23]Aksit, I. M. and Moss, J. B., "Model Fuels to Reproduce the Sooting Behaviour of Aviation Kerosene," *Fuel*, Vol. 84, 2005, pp. 239-245.

[24]Kopasz, J. P., Applegate, D., Miller, L., Liao, H. K., and Ahmed, S., "Unraveling the Maze: Understanding of Diesel Reforming through the Use of Simplified Fuel Blends," *International Journal of Hydrogen Energy*, Vol. 30, 2005, pp. 1243-1250.

[25]Antoine, A. C., "Use of Petroleum-Based Correlations and Estimation Methods for Synthetic Fuels," NASA TM-81533, 1980, pp. 1-23.

[26]Vielle, P., "Sur les Discontinuity's Produites par la Detente Brusque de Gaz Comprimes," Comptes *Rendus Hebdomadaires des Séances de l'Académie des Sciences*, Vol. 129, 1899, pp. 1228-1230.

[27]Gaydon, A. G. and Hurle, I. R., *The Shock Tube in High-Temperature Chemical Physics*, Chapman and Hall, London, 1963.

[28]Bradley, J. N. B., *Shock Waves in Chemistry and Physics*, Methuen, London, 1962.

[29]Wright, J. K., *Shock Tubes (Methuen's Monographs on Physical Subjects)*, Methuen, London, 1961.

[30]John, J. E. and Keith, T. G., *Gas Dynamics*, Pearson / Prentice Hall, Upper Saddle River, NJ, 2006, 3rd Edition.

[31]Zel´dovich, Ya. B., and Raizer, Yu. P., and Hayes, W. D. and Probstein, R. F. (Eds.), *Physics of Shock Waves and High-Temperature Hydrodynamic Phenomena*, Dover Publications, New York, 2002.

[32]Glass, I. I., Martin, W. A., and Patterson, G. N., "A Theoretical and Experimental Study of the Shock Tube," *University of Toronto Institute for Aerospace Studies Report*, November, 1953, pp. 1-45.

[33]Glass, I. I., Sislian, J. P., *Nonstationary Flows and Shock Waves*, *Oxford Engineering Science Series*, Vol. 39, 1994, pp. 10-23.

[34]Bitondo, D. and Lobb, R. K., "Design and Construction of a Shock Tube," *University of Toronto Institute for Aerospace Studies Report*, May, 1950, pp. 1-19.

[35]Lobb, R. K, "On the Length of a Shock Tube," *University of Toronto Institute for Aerospace Studies Report*, July, 1950, pp. 1-31.

[36]Salas, M.D. "On the Thermodynamic Theory of Waves of Finite Longitudinal Disturbance," *17th Shock Interaction Symposium*, September, 2006, Rome, Italy, pp. 1-20.

[37]Rankine, W. J. M. "On the Thermodynamic Theory of Waves of Finite Longitudinal Disturbances," *Philosophical Transactions of the Royal Society*, Vol. 160, 1870, pp. 277-288.

[38]Hugoniot, H., "Propagation des Mouvements dans les Corps et Spécialement dans les Gaz Parfaits," *Journal de l'Ecole Polytechnique*, 1887, Vol. 57.

[39]Xu, S., Zhu, R. S., and Lin, M. C., "Ab Initio Study of the OH + CH_2O Reaction: The Effect of the OH··OCH_2 Complex on the H-Abstraction Kinetics," *International Journal of Chemical Kinetics*, Vol. 38, 2006, pp. 322-326.

[40]Vandooren, J., Peeters, J., and Van Tiggelen, P. J., "Rate Constant of the Elementary Reaction of Carbon Monoxide with Hydroxyl Radical," *International Symposium on Combustion*, 1975, Vol. 15, pp. 745-753.

[41]Laffitte, P., Cusin, F., and James, H., "On the Influence of Hydroxyl Radicals on the Kinetics of the Combustion Reaction of Carbon Monoxide," *Combustion and Flame*, Vol. 7, 1963, pp. 101-104.

[42]Tully, F. P., Ravishankara, A. R., and Carr, K., "Kinetic Study of the Reactions of the Hydroxyl Radical with Ethane and Propane," *International Journal of Chemical Kinetics*, Vol. 15, 1983, pp. 1111-1118.

[43]Harris, M. M., King, G. B., and Laurendeau, N. M., "Influence of Temperature and Hydroxyl Concentration on Incipient Soot Formation in Premixed Flames," *Combustion and Flame*, Vol. 64, 1986, pp. 99-112.

[44]Taylor, P. H., Rahman, M. S., Arif, M., Dellinger, B., and Marshall, P., "Kinetic and Mechanistic Studies of the Reaction of Hydroxyl Radicals with Acetaldehyde over an Extended Temperature Range," *Proceedings of the 26th International Symposium on Combustion*, 1996, pp. 497-504.

[45]Oehlschlaeger, M. A., Davidson, D. F., Herbon, J. T., and Hanson, R. K., "Shock Tube Measurements of Branched Alkane Ignition Times and OH Concentration Time Histories," *International Journal of Chemical Kinetics*, Vol. 36, 2004, pp. 67-78.

[46]Markus, M. W. and Roth, P., "On the Reaction of CH with CO Studied with High Temperature CH_4/Ar + CO Mixtures," *International Journal of Chemical Kinetics*, Vol. 24, 1992, pp. 433-445.

[47]Bradley, J. N., Capey, W. D., Fair, R. W., and Pritchard, D. K., "A Shock-Tube Study of the Kinetics of Reaction of Hdyroxyl Radicals with H_2, CO, CH_4, CF_3H, C_2H_4, and C_2H_6," *International Journal of Chemical Kinetics*, Vol. 8, 1976, pp. 549-561.

[48]Vasudevan, V., Davidson, D. F., and Hanson, R. K., "Direct Measurements of the Reaction OH + CH_2O $\leftrightarrow$ HCO + H_2O at High Temperatures," *International Journal of Chemical Kinetics*, Vol. 37, 2005, pp. 98-109.

[49]Vasudevan, V., Cook, R. D., Hanson, R. K., Bowman, C. T., and Golden, D. M., "High-Temperature Shock Tube Study of the Reactions CH_3 + OH $\rightarrow$ Products and CH_3OH + Ar $\rightarrow$ Products," *International Journal of Chemical Kinetics*, Vol. 40, 2008, pp. 488-495.

[50]Bott, J. F. and Cohen, N., "A Shock Tube Study of the Reaction of Hydroxyl Radical with Propane," *International Journal of Chemical Kinetics*, Vol. 16, 1984, pp. 1557-1566.

[51]Bott, J. F. and Cohen, N., "A Shock Tube Study of the Reaction of Methyl Radicals with Hydroxyl Radicals," *International Journal of Chemical Kinetics*, Vol. 23, 1991, pp. 1017-1033.

[52]Bott, J. F. and Cohen, N., "A Shock Tube Study of the Reactions of Hydroxyl Radical with Several Combustion Species," *International Journal of Chemical Kinetics*, Vol. 23, 1991, pp. 1075-1094.

[53]Bott, J. F. and Cohen, N., "A Shock Tube Study of the Reaction of the Hydroxyl Radical with H_2, CH_4, c-C_5H_{10}, and i-C_4H_{10}," *International Journal of Chemical Kinetics*, Vol. 21, 1989, pp. 485-498.

[54]Miller, J. A. and Melius, C. F., "A Theoretical Analysis of the Reaction Between Hydroxyl and Acetylene," *Proceedings of the 22nd International Symposium on Combustion*, 1988, pp. 1031-1019.

[55]Su, J. Z. and Teitelbaum, H., "The Rate of Methyl Radical Decomposition at High Temperatures and Pressures," *International Journal of Chemical Kinetics*, Vol. 26, 1994, pp. 159-169.

[56]Panoutsos, C. S., Hardalupas, Y., and Taylor, A. M. K. P., "Numerical Evaluation of Equivalence Ratio Measurement Using OH* and CH* Chemiluminescence in Premixed and Non-Premixed Methane-Air Flames," *Combustion and Flame*, Vol. 156, 2009, pp. 273-291.

[57]Chou, M.-S. and Dean, A. M., "Excimer Laser Perturbations of Methane Flames: High Temperature Reactions of OH and CH," *International Journal of Chemical Kinetics*, Vol. 17, 1985, pp. 1103-1118.

[58]Dean, A. J., Penyazkov, O. G., Sevruk, K. L., and Varatharajan, B., "Autoignition of Surrogate Fuels at Elevated Temperatures and Pressures," *Proceedings of the Combustion Institute*, Vol. 31, 2007, pp. 2481-2488.

[59]Vasu, S. S., Davidson, D. F., and Hanson, R. K., "Shock Tube Ignition Delay Times and Modeling of Jet Fuel Mixtures," AIAA Paper 2006-4402, 2006, pp. 1-10.

[60]Vasu, S. S., Davidson, D. F., and Hanson, R. K., "Jet Fuel Ignition Delay Times: Shock Tube Experiments Over Wide Conditions and Surrogate Model Predictions," *Combustion and Flame*, Vol. 152, 2008, pp. 125-143.

[61]Bradley, D. and Head, R. A., "Engine Autoignition: The Relationship between Octane Numbers and Autoignition Delay Times," *Combustion and Flame*, Vol. 147, 2006, pp. 171-184.

[62]Davidson, D. F., Oehlschlaeger, M. A., Herbon, J. T., and Hanson, R. K., "Shock Tube Measurements of Iso-Octane Ignition Times and OH Concentration Time Histories," *Proceedings of the Combustion Institute*, Vol. 29, 2002, pp. 1295-1301.

[63]Davidson, D. F.,Gauthier, B. M. and Hanson, R. K., "Shock Tube Ignition Measurements of iso-Octane/Air and Toluene/Air at High Pressures," *Proceedings of the Combustion Institute*, Vol. 30, 2005, pp. 1175-1182.

[64]Davidson, D. F., Oehlschlaeger, M. A., and Hanson, R. K., "Methyl Concentration Time-Histories during iso-Octane and n-Heptane Oxidation and Pyrolysis," *Proceedings of the Combustion Institute*, Vol. 31, 2007, pp. 321-328.

[65]Gauthier, B. M., Davidson, D. F., and Hanson, R. K., "Shock Tube Determination of Ignition Delay Times in Full-Blend and Surrogate Fuel Mixtures," *Combustion and Flame*, Vol. 139, 2004, pp. 300-311.

[66]Fikri, M., Herzler, J., Starke, R., Schulz, C., Roth, P., and Kalghatigi, G. T., "Autoignition of Gasoline Surrogates Mixtures at Intermediate Temperatures and High Pressures," *Combustion and Flame*, Vol. 152, 2008, pp. 276-281.

[67]Herzler, J., Fikri, M., Hitzbleck, K., Starke, R., Schulz, C., Roth, P., and Kalghatgi, G. T., "Shock-Tube Study of the Autoignition of n-Heptane/Toluene/Air Mixtures at Intermediate Temperatures and High Pressures," *Combustion and Flame*, Vol. 149, 2007, pp. 25-31.

[68]Olchanski, E. and Burcat, A., "Decane Oxidation in a Shock Tube," *International Journal of Chemical Kinetics*, Vol. 38, 2006, pp. 703-713.

[69]Pfahl, U., Fieweger, K., and Adomeit, G., "Self-Ignition of Diesel-Relevant Hydrocarbon-Air Mixtures Under Engine Conditions," *Twenty-Sixth International Symposium on Combustion*, 1996, pp. 781-789.

[70]Zhukov, V. P., Sechenov, V. A., Starikovskii, and A. Yu., "Autoignition of n-Decane at High Pressure," *Combustion and Flame*, Vol. 153, 2008, pp. 130-136.

[71]Maigaard, P., Mauss, F., and Kraft, M., "Homogeneous Charge Compression Ignition Engine: A Simulation Study on the Effects of Inhomogeneities," ASME Paper 2000-ICE-275, 2000, pp. 63-70.

[72]Hernandez, J. J., Sanz-Argent, J., Benajes, J., and Molina, S., "Selection of a Diesel Fuel Surrogate for the Prediction of Auto-Ignition under HCCI Engine Conditions," *Fuel*, Vol. 87, 2008, pp. 655-665.

[73]Kalitan, D. M. and Petersen, E. L., "Ignition and Oxidation of Lean CO/H_2 Fuel Blends in Air," AIAA Paper 2005-3767, pp. 1-8.

[74]Petersen, E. L., Davidson, D. F., and Hanson, R. K., "Kinetics Modeling of Shock-Induced Ignition in Low-Dilution CH_4/O_2 Mixtures at High Pressures and Intermediate Temperatures," *Combustion and Flame*, Vol. 117, 1999, pp. 272-290.

[75]de Vries, J. and Petersen, E. L., "Autoignition of Methane-Based Fuel Blends under Gas Turbine Conditions," *Proceedings of the Combustion Institute*, Vol. 31, 2007, pp. 3163-3171.

[76]Spadaccini, L. J. and Colkett III, M. B., "Ignition Delay Characteristics of Methane Fuels," *Progress Energy and Combustion Science*, Vol. 20, 1994, pp. 431-460.

[77]Petersen, E. L., Hall, J. M., Smith, S. D., de Vries, J., Amadio, A. R., and Crofton, M. W., "Ignition of Lean Methane-Based Fuel Blends at Gas Turbine Pressures," *Journal of Engineering for Gas Turbines and Power*, Vol. 129, 2007, pp. 937-944.

[78]Pekalski, A. A., Terli, E., Zevenbergen, J. F., Lemkowitz, S. M., and Pasman, H. J., "Influence of the Ignition Delay Time on the Explosion Parameters of Hydrocarbon-Air-Oxygen Mixtures at Elevated Pressure and Temperature," *Proceedings of the Combustion Institute*, Vol. 30, 2005, pp. 1933-1939.

[79]Shen, H.-P. S., Vanderover, J., and Oehlschlaeger, M. A., "A Shock Tube Study of iso-Octane Ignition at Elevated Pressures: The Influence of Diluent Gases," *Combustion and Flame*, Vol. 155, 2008, pp. 739-755.

[80]Oehlschlaeger, M. A., Davidson, D. F., Herbon, J. T., and Hanson, R. K., "Shock Tube Measurements of Branched Alkane Ignition Times and OH Concentration Time Histories," *International Journal of Chemical Kinetics*, Vol. 36, 2004, pp. 67-78.

[81]Olchanski, E. and Burcat, A., "Decane Oxidation in a Shock Tube," *International Journal of Chemical Kinetics*, Vol. 38, 2006, pp. 703-713.

[82]Zhukov, V. P., Sechenov, V. A., Starikovskii, and A. Yu., "Autoignition of n-Decane at High Pressure," *Combustion and Flame*, Vol. 153, 2008, pp. 130-136.

[83]Kumar, K., Mittal, G., and Sung, C.-J., "Autoignition of n-Decane under Elevated Pressure and Low-to-Intermediate Temperature Conditions," *Combustion and Flame*, Vol. 156, 2009, pp. 1278-1288.

[84]Axelsson, E. I., Brezinsky, K., Dryer, F. L., Pitz, W. J., and Westbrook, C. K., "Chemical Kinetic Modeling of the Oxidation of Large Alkane Fuels: n-Octane and iso-Octane," *Proceedings of the Combustion Institute*, Vol. 21, 1986, pp. 783-793.

[85]Westbrook, C. K., Warnatz, J., and Pitz, W. J., "A Detailed Chemical Kinetic Reaction Mechanism for the Oxidation of iso-Octane and n-Heptane over an Extended Temperature Range and Its Application to Analysis of Engine Knock," *Proceedings of the Combustion Institute*, Vol. 22, 1988, pp. 893-901.

[86]Bikas, G. and Peters, N., "Kinetic Modelling of n-Decane Combustion and Autoignition: Modeling Combustion of n-Decane," *Combustion and Flame*, Vol. 126, 2001, pp. 1456-1475.

[87]Warnatz, J., "Chemistry of High Temperature Combustion of Alkanes up to Octane," *Proceedings of the Combustion Institute*, Vol. 20, 1984, pp. 845-856.

[88]Zeppieri, S. P., Klotz, S. D., and Dryer, F. L., "Modeling Concepts for Larger Carbon Number Alkanes: A Partially Reduced Skeletal Mechanism for n-Decane Oxidation and Pyrolysis," *Proceedings of the Combustion Institute*, Vol. 28, 2000, pp. 1587-1595.

[89]Simmie, J. M., "Detailed Chemical Kinetic Models for the Combustion of Hydrocarbon Fuels," *Progress in Energy and Combustion Science*, Vol. 29, 2003, pp. 599-634.

[90]Westbrook, C. K., Pitz, W. J., Herbinet, O., Curran, H. J., and Silke, E. J., "A Comprehensive Detailed Chemical Kinetic Reaction Mechanism for Combustion of n-Alkane Hydrocarbons from n-Octane to n-Hexadecane," *Combustion and Flame*, Vol. 156, 2009, pp. 181-199.

[91]Ji, C., Dames, E., Wang, Y. L., Wang, H., and Egolfopoulos, F. N., "Propagation and Extinction of Premixed C5–C12 n-Alkane Flames," *Combustion and Flame*, In Press, Corrected Proof, 2009.

[92]Koffend, J., B. and Cohen, N., "Shock Tube Study of OH Reactions with Linear Hydrocarbons near 1100 K," *International Journal of Chemical Kinetics*, Vol. 28, 1996, pp. 79-87.

[93]Zhou, P., Hollis, O. L., and Crynes, B. L., "Thermolysis of Higher Molecular Weight Straight-Chain Alkanes (C_9-C_{22})," *Industrial and Engineering Chemistry Research*, Vol. 26, 1987, pp. 846-852.

[94]Kunzru, D., Shah, Y. T., and Stuart, E. B., "Thermal Cracking of n-Nonane," *Industrial and Engineering Chemistry Process Design and Development*, Vol. 11, 1972, pp. 605-612.

[95]Bae, J. H. and Avedisian, C. T., "High-Pressure Combustion of Submillimeter-Sized Nonane Droplets in a Low Convection Environment," *Combustion and Flame*, Vol. 145, 2006, pp. 607-620.

[96]Bae, J. H. and Avedisian, C. T., "Experimental Study of the Combustion Dynamics of Jet Fuel Droplets with Additives in the Absence of Convection," *Combustion and Flame*, Vol. 137, 2004, pp. 148-162.

[97]Callahan, B. J. and Avedisian, C. T., "Combustion of Nonane Fuel Droplets in Microgravity," AIAA Paper 99-1077, 1999, pp. 1-6.

[98]Petersen, E. L., Rickard, M. J. A., Crofton, M. W., Abbey, E. D., Traum, M. J., and Kalitan, D. M., "A Facility for Gas- and Condensed-Phase Measurements behind Shock Waves," *Measurement Science and Technology*, Vol. 16, 2005, pp. 1716-1729.

[99]Petersen, E. L., *A Shock Tube and Diagnostics for Chemistry Measurements at Elevated Pressures with Application to Methane Ignition*," Ph.D. Dissertation, Stanford University, 1999.

[100]Dykyj, J., Svoboda, J., Wilhoit, R. C., and Frenkel, M., *Vapor Pressure and Antoine Constants for Hydrocarbons, and Sulfur, Selenium, Tellurium, and Halogen Containing Organic Compounds*, Springer, Berlin, Hall, K. R. (Ed.), 1999, 1st Edition.

[101]Poling, B. E., Prausnitz, J. M., and O'Connell, J. P., *Properties of Liquids and Gases*, McGraw-Hill Professional, New York, 2001, 5th Edition.

[102]Petersen, E. L., "Interpreting Endwall and Sidewall Measurements in Shock-Tube Ignition Studies," *Combustion Science and Technology*, Vol. 181, 2009, pp. 1123-1144.

[103]Wang, H. and Laskin, A., "On Initiation Reactions of Acetylene Oxidation in Shock Tubes: A Quantum Mechanical and Kinetic Modeling Study," *Chemical Physics Letters*, Vol. 303, 1999, pp. 43-49.

APPENDIX A

ACTIVATION ENERGY RESULTS

Table A–1: Activation Energy Results for Fuel-Rich C_9H_{20}/O_2 in Ar

$\phi = 0.5$

τ (μs)	T_5 (K)	ln τ	1 /T (K^{-1})	Run
329	1352	5.80	0.00074	1414
453	1351	6.12	0.00074	1415
247	1403	5.51	0.00071	1418
245	1391	5.50	0.00072	1419
203	1411	5.31	0.00071	1420
198	1399	5.29	0.00071	1421
319	1366	5.77	0.00073	1422
235	1391	5.46	0.00072	1442
549	1343	6.31	0.00074	1444
428	1349	6.06	0.00074	1445
414	1360	6.03	0.00074	1446
436	1345	6.08	0.00074	1447
544	1346	6.30	0.00074	1448
245	1400	5.50	0.00071	1449
311	1381	5.74	0.00072	1450
485	1349	6.18	0.00074	1451
107	1478	4.68	0.00068	1452
218	1420	5.39	0.00070	1453
195	1425	5.27	0.00070	1454
1038	1309	6.94	0.00076	1455
129	1458	4.86	0.00069	1456
139	1457	4.93	0.00069	1457
1092	1306	7.00	0.00077	1458
1104	1285	7.01	0.00078	1459
720	1341	6.58	0.00075	1460
468	1399	6.15	0.00071	1462
259	1465	5.56	0.00068	1463

E_A /R (1 /K)
22267.2

E_A (cal /mol)
44217.5

E_A (kcal /mol)
44.2

Table A–2: Activation Energy Results for Stoichiometric C_9H_{20}/O_2 in Ar

$\phi = 1.0$

τ (μs)	T_5 (K)	ln τ	1 /T (K^{-1})	Run
54	1591	3.98	0.00063	1399
116	1537	4.75	0.00065	1400
104	1535	4.64	0.00065	1406
378	1447	5.94	0.00069	1407
729	1402	6.59	0.00071	1408
259	1480	5.56	0.00068	1409
205	1519	5.32	0.00066	1410
195	1485	5.28	0.00067	1432
208	1457	5.34	0.00069	1433
254	1470	5.54	0.00068	1434
228	1462	5.43	0.00068	1435
218	1487	5.38	0.00067	1436
550	1412	6.31	0.00071	1437
539	1409	6.29	0.00071	1438
439	1443	6.09	0.00069	1439
458	1434	6.13	0.00070	1440

E_A /R (1 /K)
28197.1

E_A (cal /mol)
55992.7

E_A (kcal /mol)
56.0

Table A–3: Activation Energy Results for Fuel-Rich C_9H_{20}/O_2 in Ar

$\phi = 2.0$

τ (μs)	T_5 (K)	ln τ	1 /T (K^{-1})	Run
964	1412	6.87	0.00071	1423
383	1521	5.95	0.00066	1424
306	1510	5.72	0.00066	1425
181	1555	5.20	0.00064	1426
707	1460	6.56	0.00068	1427
403	1508	6.00	0.00066	1428
195	1543	5.27	0.00065	1429
333	1515	5.81	0.00066	1430
441	1462	6.09	0.00068	1464
490	1477	6.19	0.00068	1465
761	1443	6.63	0.00069	1466
296	1523	5.69	0.00066	1467
280	1529	5.63	0.00065	1468
465	1497	6.14	0.00067	1469
800	1454	6.68	0.00069	1470

E_A /R (1 /K)
25726.5

E_A (cal /mol)
51086.8

E_A (kcal /mol)
51.1

APPENDIX B

TABULATION OF OH*-BASED IGNITION DELAY TIMES

Table B–1: Ignition and Peak Concentration Times (Post-Ignition) for Fuel-Lean C_9H_{20}/O_2 in Ar

T (K)	P (atm)	τ (μs)	τ_{peak} - $\tau_{ignition}$ (μs)	Diagnostic
		$0.001n\text{-}C_9H_{20} + 0.028O_2 + 0.971Ar$ ($\phi = 0.5$)		
1285	1.56	1104	-	
1306	1.62	1092	169	
1309	1.62	1038	202	
1341	1.57	720	335	
1343	1.58	549	169	
1345	1.59	436	156	
1346	1.59	544	153	
1349	1.60	428	150	
1349	1.58	485	157	
1351	1.60	453	154	
1352	1.49	329	182	
1360	1.62	414	144	
1366	1.63	319	195	OH*
1381	1.63	311	170	
1391	1.54	245	106	
1391	1.50	235	139	
1399	1.49	198	151	
1400	1.48	245	117	
1403	1.52	247	111	
1411	1.53	203	110	
1420	1.48	218	110	
1425	1.49	195	120	
1457	1.51	139	147	
1458	1.51	129	109	
1478	1.54	107	105	

Table B–2: Ignition and Peak Concentration Times (Post-Ignition) for Stoichiometric C_9H_{20}/O_2 in Ar

T (K)	P (atm)	τ (μs)	τ_{peak} - $\tau_{ignition}$ (μs)	Diagnostic
		0.001n-C_9H_{20} + 0.014O_2 + 0.985Ar (ϕ = 1.0)		
1402	1.610	729	284	OH*
1409	1.510	539	258	
1412	1.509	550	169	
1434	1.529	458	160	
1443	1.543	439	212	
1447	1.569	378	179	
1457	1.564	208	152	
1462	1.454	228	218	
1470	1.490	254	168	
1480	1.521	259	167	
1485	1.538	195	136	
1487	1.529	218	132	
1519	1.528	205	130	
1535	1.496	104	129	
1537	1.466	116	131	
1591	1.365	54	99	

Table B–3: Ignition and Peak Concentration Times (Post-Ignition) for Fuel-Rich C_9H_{20}/O_2 in Ar

T (K)	P (atm)	τ (μs)	τ_{peak} - $\tau_{ignition}$ (μs)	Diagnostic
		0.001n-C_9H_{20} + 0.007O_2 + 0.992Ar (ϕ = 2.0)		
1412	1.50	964	422	OH*
1443	1.43	761	393	
1454	1.47	800	145	
1460	1.49	707	494	
1462	1.47	441	267	
1477	1.49	490	331	
1508	1.47	403	370	
1510	1.43	306	321	
1515	1.52	333	363	
1521	1.49	383	298	
1523	1.43	296	363	
1529	1.44	280	403	
1543	1.46	195	371	
1555	1.53	181	301	

APPENDIX C

CALCULATION OF IGNITION DELAY TIME CORRELATION

Table C–1: Parameters and Results of Ignition Delay Time Correlation.

τ (μs) = $4.02 \cdot 10^{-5}[C_9H_{20}]^{1.65072}[O_2]^{-4.09886}[Ar]^{3.94694}\exp(19228.23/T)$

m_4	b
19228.23	-10.12216
m_3	exp(b)
3.94694	4.02E-05
m_2	
-4.09886	
m_1	
1.65072	

E_A (kJ /mol)	159.9
E_A (kcal /mol)	38.2

Pressure Exponent (n)
1.50

$n = \sum_i m_i$

ϕ = 0.5			ϕ = 1.0			ϕ = 2.0		
$\tau_{Ignition.}$ (μs)	$\tau_{Corr.}$ (μs)	T (K)	$\tau_{Ignition.}$ (μs)	$\tau_{Corr.}$ (μs)	T (K)	$\tau_{Ignition.}$ (μs)	$\tau_{Corr.}$ (μs)	T (K)
329	431	1352	54	60	1591	964	1101	1412
453	486	1351	116	117	1537	383	308	1521
246	229	1403	104	124	1535	306	329	1510
245	271	1391	378	357	1447	181	225	1555
203	209	1411	729	642	1402	707	615	1460
198	233	1399	259	232	1480	403	348	1508
319	409	1366	205	151	1519	195	236	1543
235	262	1391	195	223	1485	333	339	1515
549	534	1343	208	315	1457	441	580	1462
428	498	1349	254	252	1470	490	500	1477
414	438	1360	228	267	1462	761	701	1443
436	522	1345	218	216	1487	296	282	1523
544	515	1346	550	514	1412	280	266	1529
245	230	1400	539	535	1409	800	629	1454
311	335	1381	439	365	1443			
485	491	1349	458	401	1434			
107	95	1478						
218	179	1420						
195	170	1425						
1038	888	1309						
129	117	1458						
139	117	1457						
1092	922	1306						
1104	1187	1285						
720	543	1341						

APPENDIX D

OH* SPECIES TIME-HISTORIES

Fuel-Lean (ϕ = 0.5) Profiles

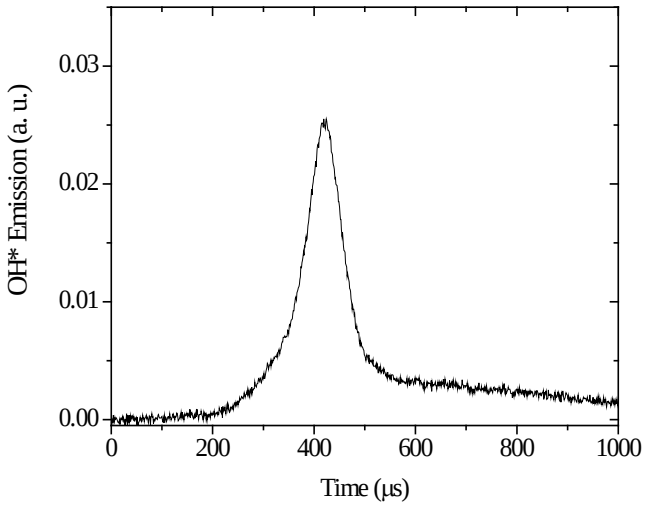

Run 1414: T = 1352 K, P = 1.49 atm, $\tau_{Ignition}$ = 329 μs, $\tau_{Peak - Ignition}$ = 182 μs.

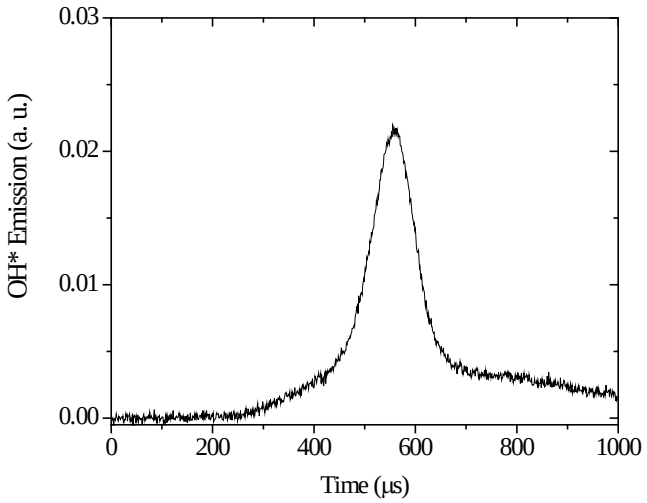

1415: T = 1351 K, P = 1.60 atm, $\tau_{Ignition}$ = 453 μs, $\tau_{Peak - Ignition}$ = 154 μs.

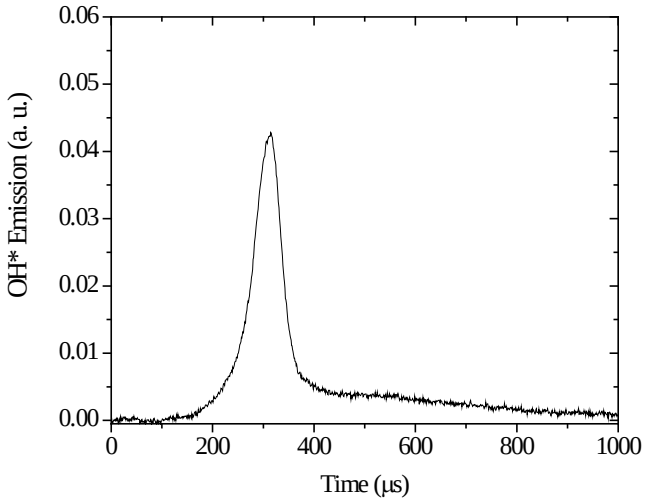

1418: T = 1403 K, P = 1.52 atm, $\tau_{Ignition}$ = 247 μs, $\tau_{Peak - Ignition}$ = 111 μs.

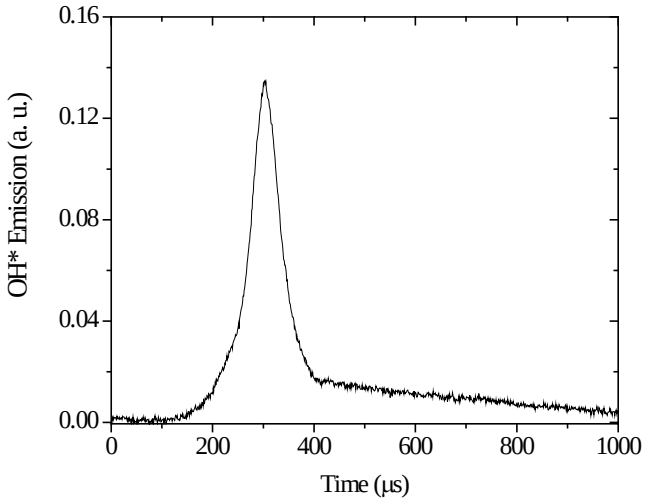

1419: T = 1391 K, P = 1.54 atm, $\tau_{Ignition}$ = 245 μs, $\tau_{Peak - Ignition}$ = 106 μs.

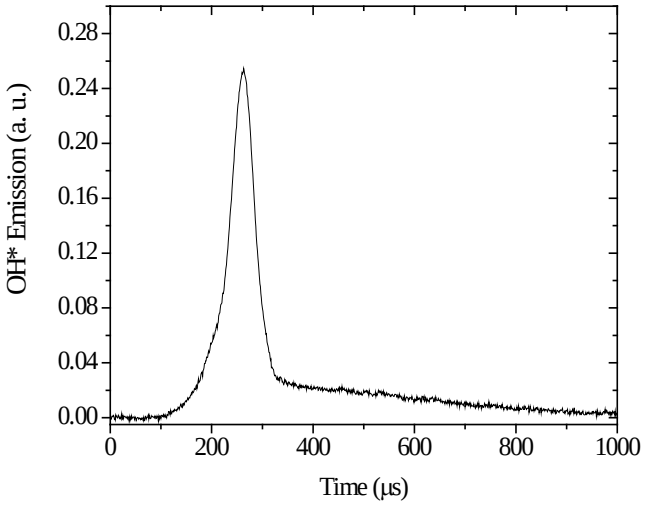

1420: T = 1411 K, P = 1.53 atm, $\tau_{Ignition}$ = 203 μs, $\tau_{Peak - Ignition}$ = 110 μs.

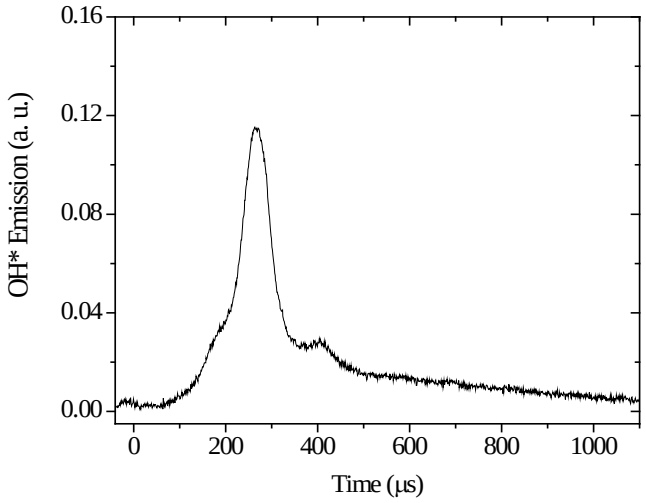

1421: T = 1399 K, P = 1.49 atm, $\tau_{Ignition}$ = 198 μs, $\tau_{Peak - Ignition}$ = 151 μs.

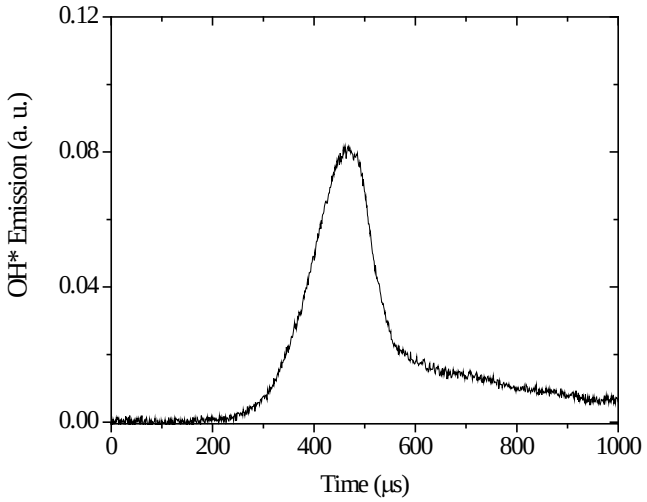

1422: T = 1366 K, P = 1.63 atm, $\tau_{Ignition}$ = 319 μs, $\tau_{Peak - Ignition}$ = 195 μs.

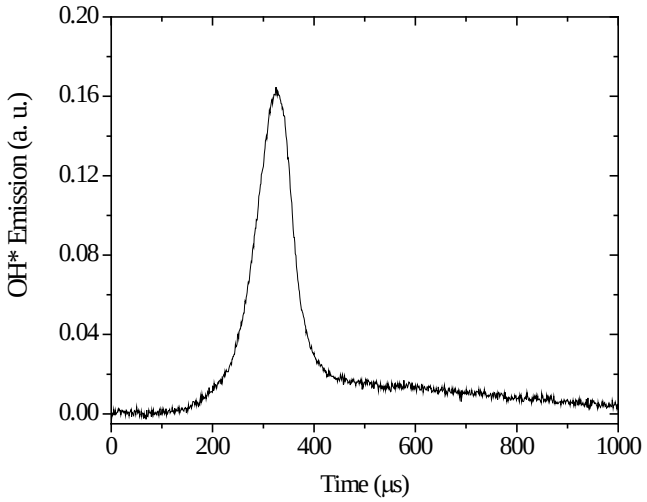

1442: T = 1391 K, P = 1.50 atm, $\tau_{Ignition}$ = 235 μs, $\tau_{Peak - Ignition}$ = 139 μs.

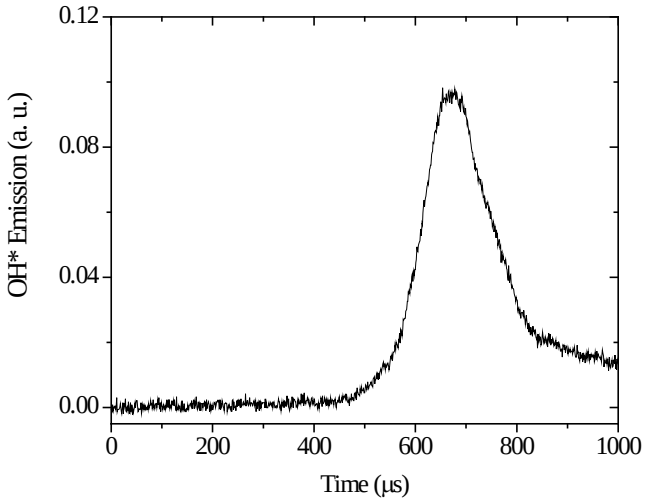

1444: T = 1343 K, P = 1.58 atm, $\tau_{Ignition}$ = 549 μs, $\tau_{Peak-Ignition}$ = 169 μs.

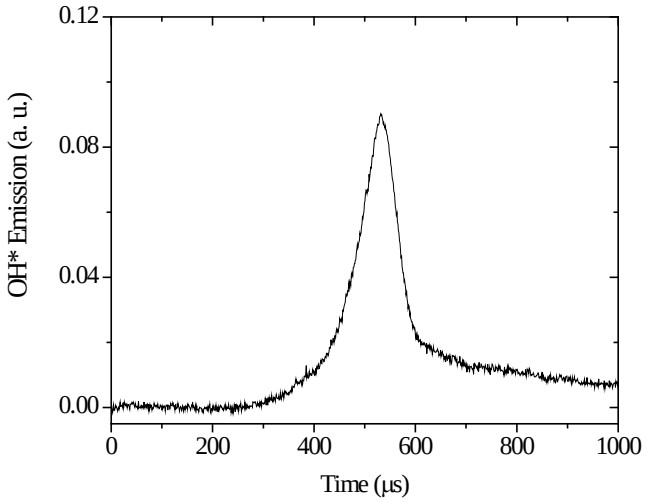

1445: T = 1349 K, P = 1.60 atm, $\tau_{Ignition}$ = 428 μs, $\tau_{Peak-Ignition}$ = 150 μs.

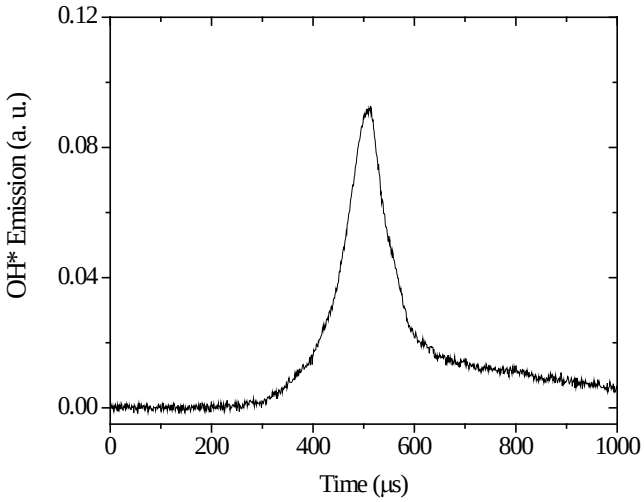

1446: T = 1360 K, P = 1.62 atm, $\tau_{Ignition}$ = 414 μs, $\tau_{Peak - Ignition}$ = 144 μs.

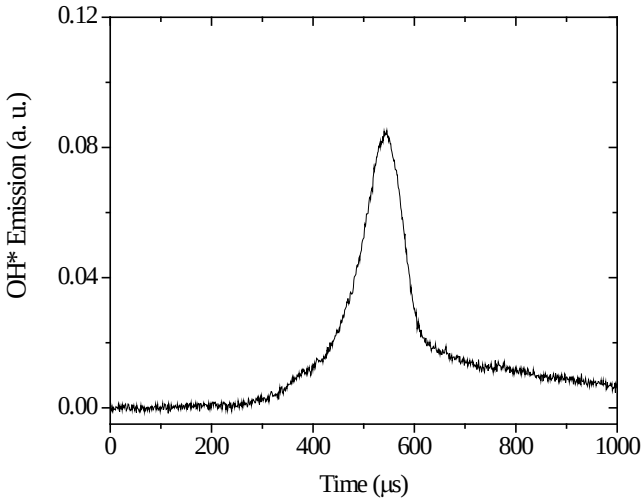

1447: T = 1345 K, P = 1.59 atm, $\tau_{Ignition}$ = 436 μs, $\tau_{Peak - Ignition}$ = 156 μs.

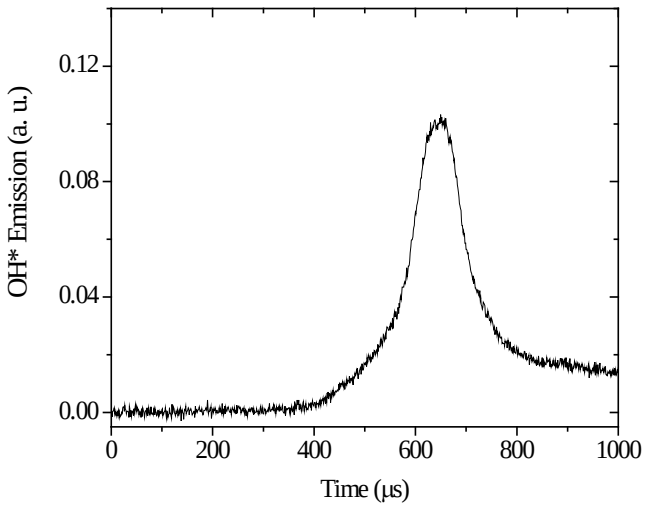

1448: T = 1346 K, P = 1.59 atm, $\tau_{Ignition}$ = 544 μs, $\tau_{Peak-Ignition}$ = 153 μs.

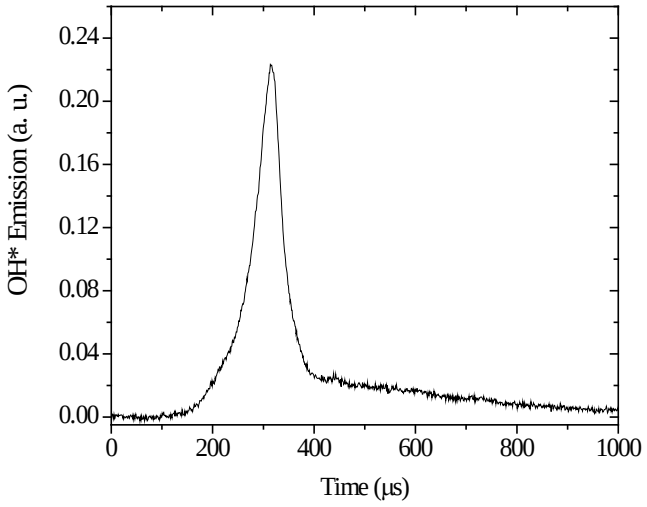

1449: T = 1400 K, P = 1.48 atm, $\tau_{Ignition}$ = 245 μs, $\tau_{Peak-Ignition}$ = 117 μs.

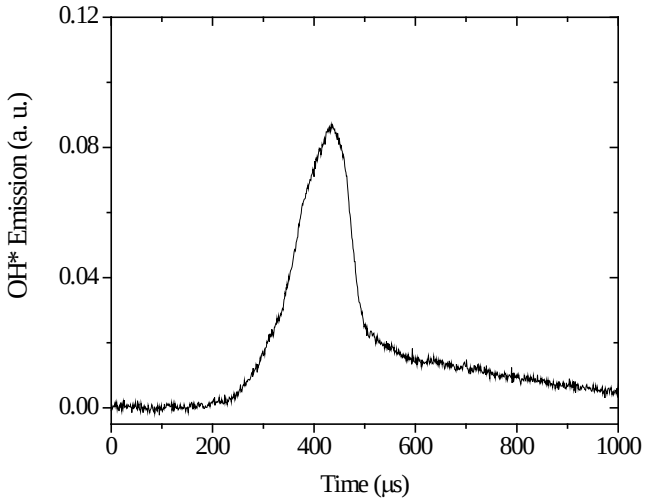

1450: T = 1381 K, P = 1.63 atm, $\tau_{Ignition}$ = 311 μs, $\tau_{Peak - Ignition}$ = 170 μs.

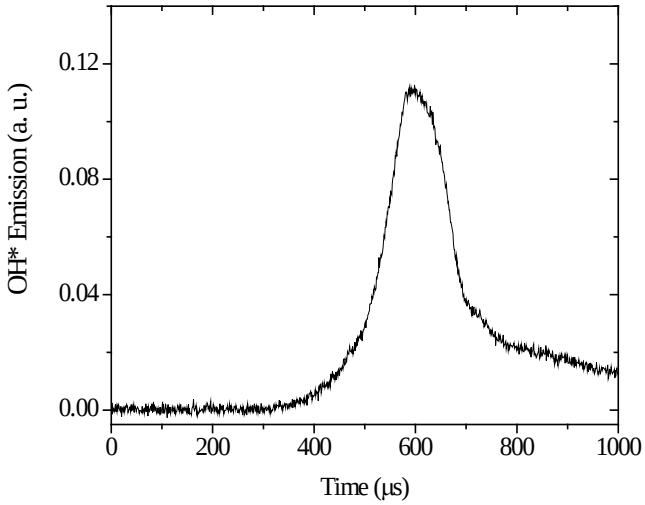

1451: T = 1349 K, P = 1.58 atm, $\tau_{Ignition}$ = 485 μs, $\tau_{Peak - Ignition}$ = 157 μs.

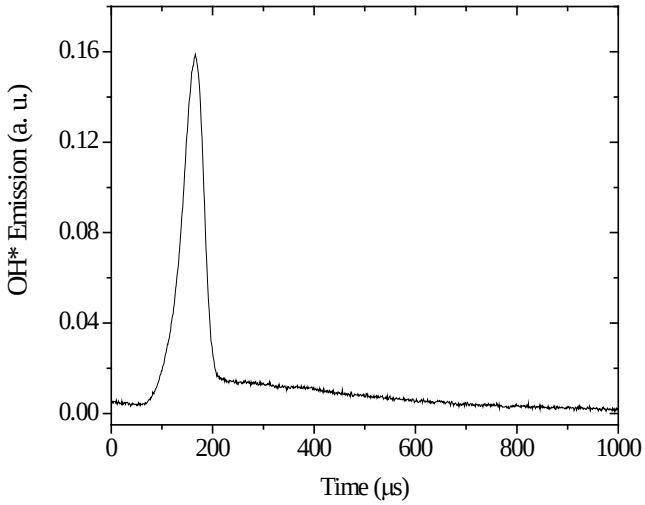

1452: T = 1478 K, P = 1.54 atm, $\tau_{Ignition}$ = 107 μs, $\tau_{Peak - Ignition}$ = 105 μs.

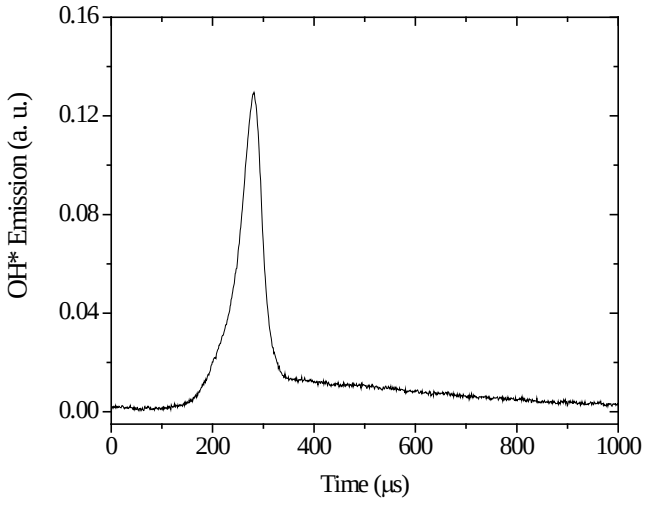

1453: T = 1420 K, P = 1.48 atm, $\tau_{Ignition}$ = 218 μs, $\tau_{Peak - Ignition}$ = 110 μs.

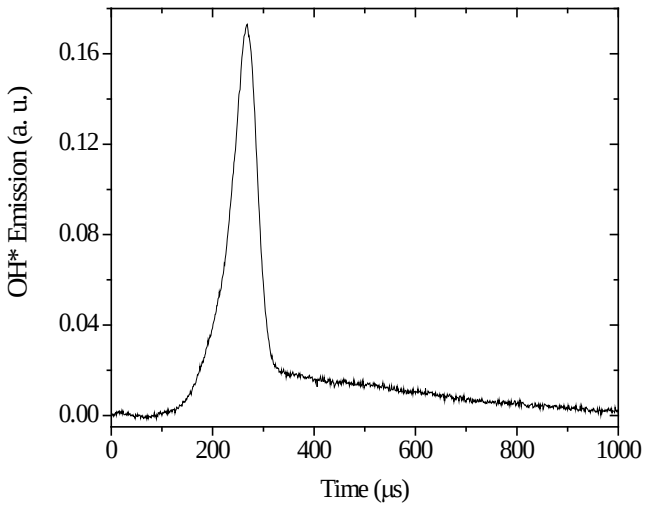

1454: T = 1425 K, P = 1.49 atm, $\tau_{Ignition}$ = 195 μs, $\tau_{Peak - Ignition}$ = 120 μs.

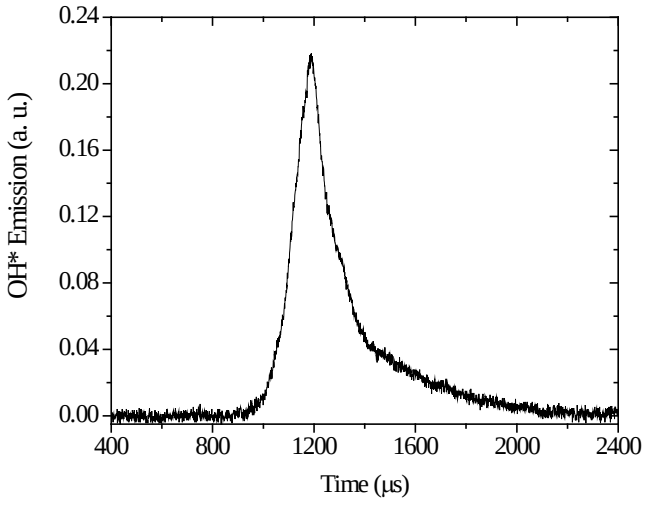

1455: T = 1309 K, P = 1.62 atm, $\tau_{Ignition}$ = 1038 μs, $\tau_{Peak - Ignition}$ = 202 μs.

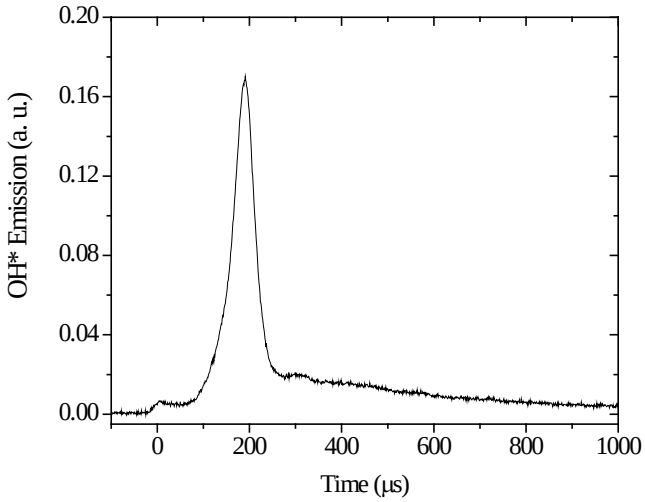

1456: T = 1458 K, P = 1.51 atm, $\tau_{Ignition}$ = 129 μs, $\tau_{Peak - Ignition}$ = 109 μs.

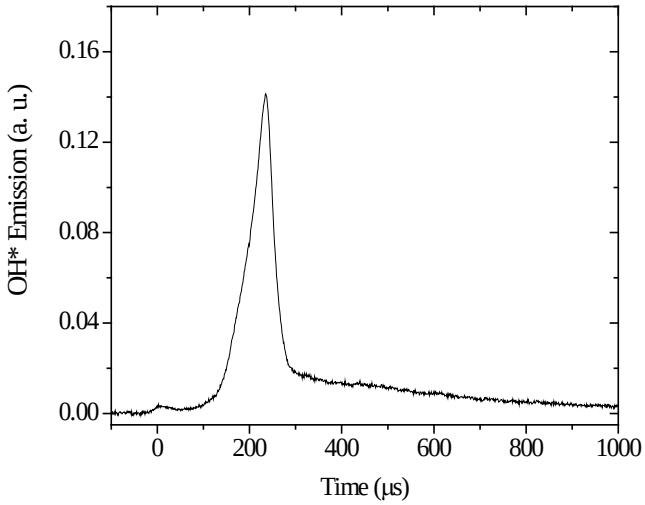

1457: T = 1457 K, P = 1.51 atm, $\tau_{Ignition}$ = 139 μs, $\tau_{Peak - Ignition}$ = 147 μs.

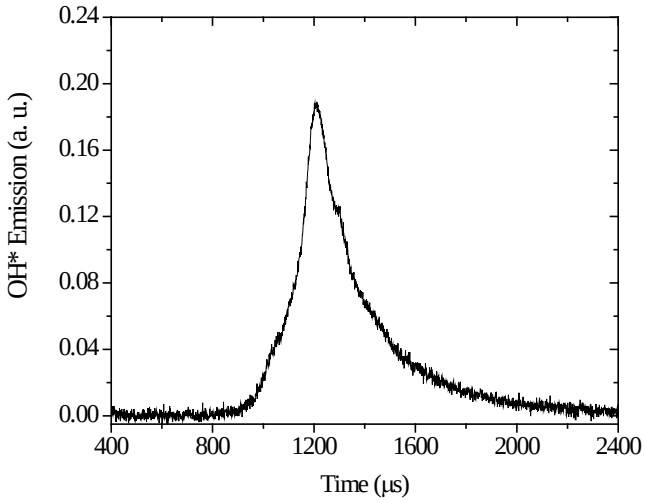

1458: T = 1306 K, P = 1.62 atm, $\tau_{Ignition}$ = 1092 μs, $\tau_{Peak - Ignition}$ = 169 μs.

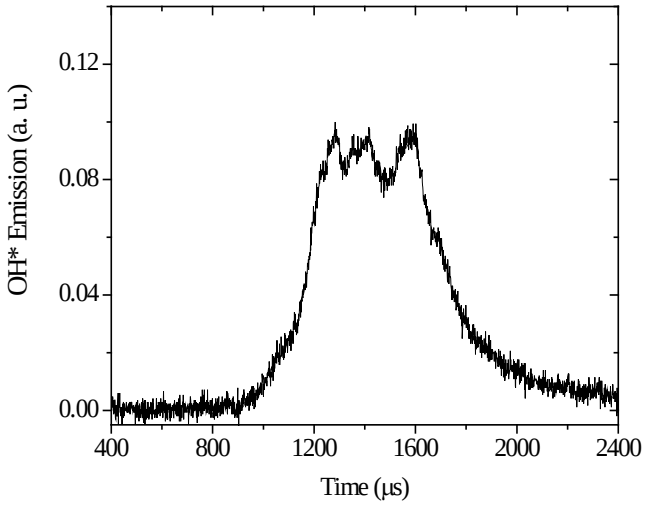

1459: T = 1285 K, P = 1.56 atm, $\tau_{Ignition}$ = 1104 μs.

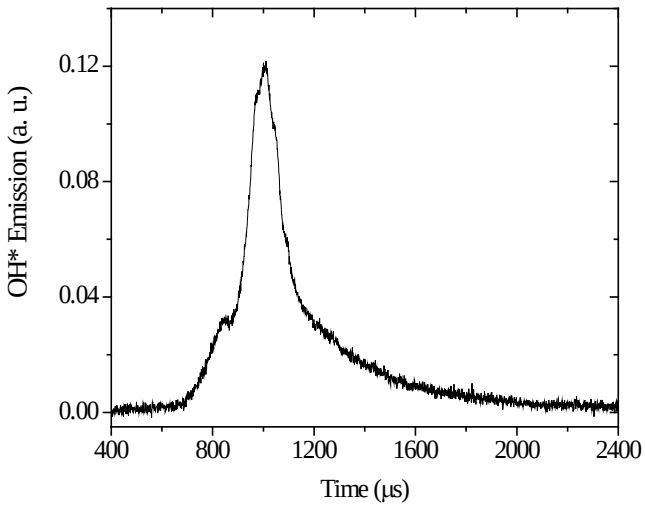

1460: T = 1341 K, P = 1.57 atm, $\tau_{Ignition}$ = 720 μs, $\tau_{Peak - Ignition}$ = 335 μs.

Stoichiometric (ϕ = 1.0) Profiles

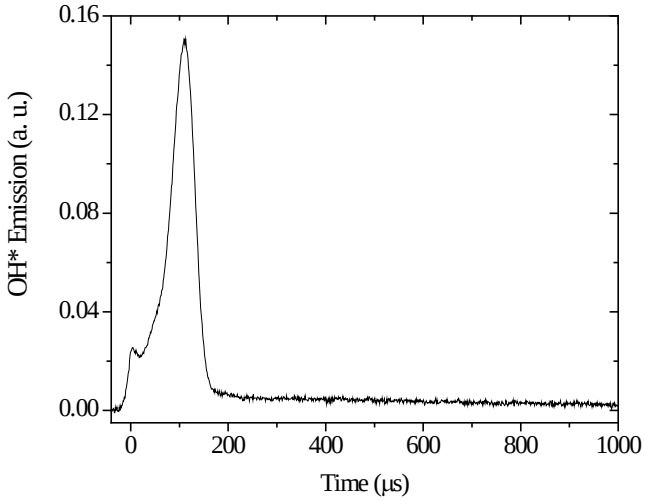

1399: T = 1591 K, P = 1.37 atm, $\tau_{Ignition}$ = 54 μs, $\tau_{Peak - Ignition}$ = 99 μs.

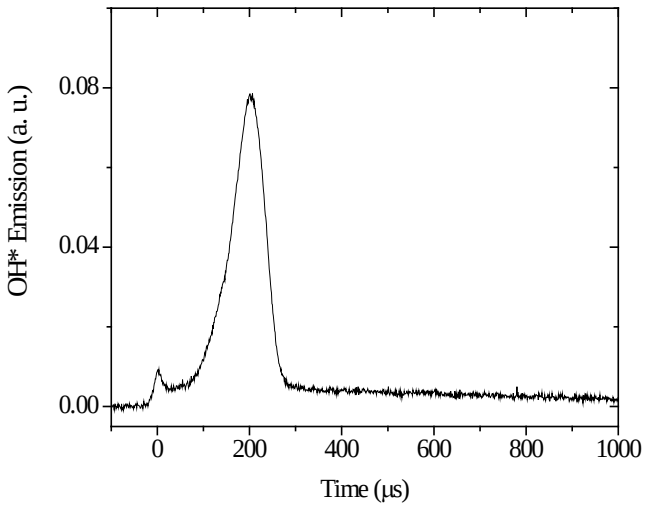

1400: T = 1537 K, P = 1.47 atm, $\tau_{Ignition}$ = 116 μs, $\tau_{Peak - Ignition}$ = 131 μs.

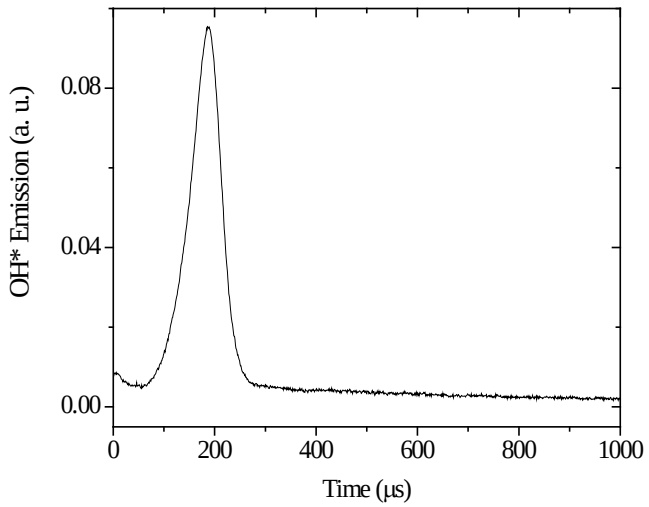

1406: T = 1535 K, P = 1.50 atm, $\tau_{Ignition}$ = 104 μs, $\tau_{Peak - Ignition}$ = 129 μs.

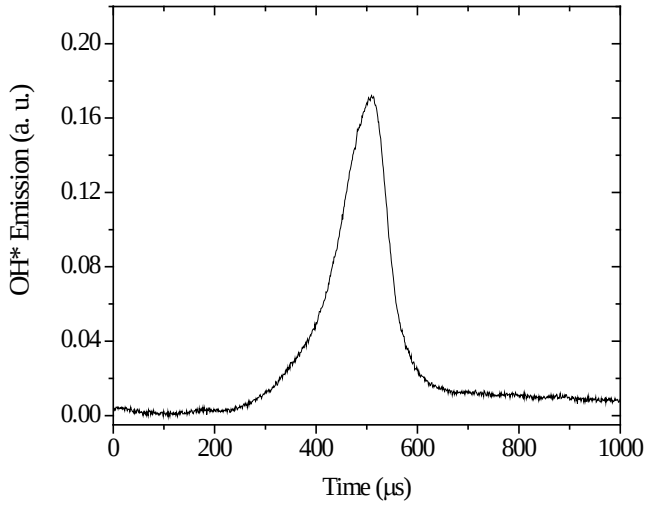

1407: T = 1447 K, P = 1.57 atm, $\tau_{Ignition}$ = 378 μs, $\tau_{Peak - Ignition}$ = 179 μs.

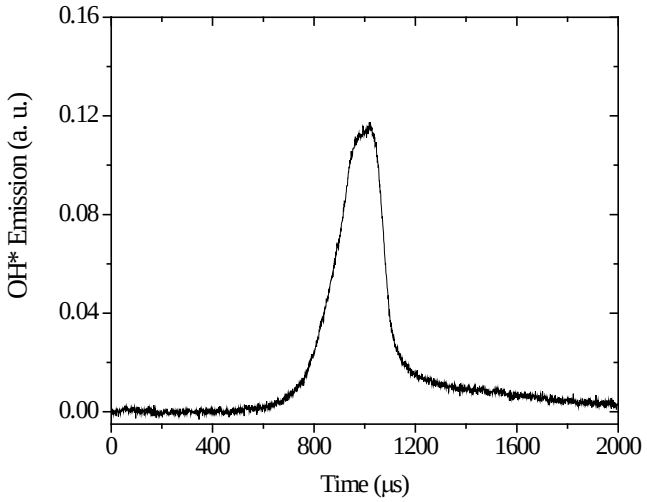

1408: T = 1402 K, P = 1.61 atm, $\tau_{Ignition}$ = 729 μs, $\tau_{Peak - Ignition}$ = 284 μs.

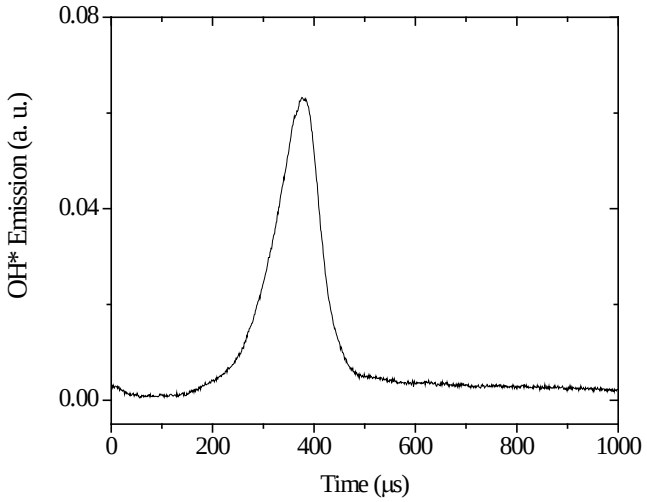

1409: T = 1480 K, P = 1.52 atm, $\tau_{Ignition}$ = 259 μs, $\tau_{Peak - Ignition}$ = 167 μs.

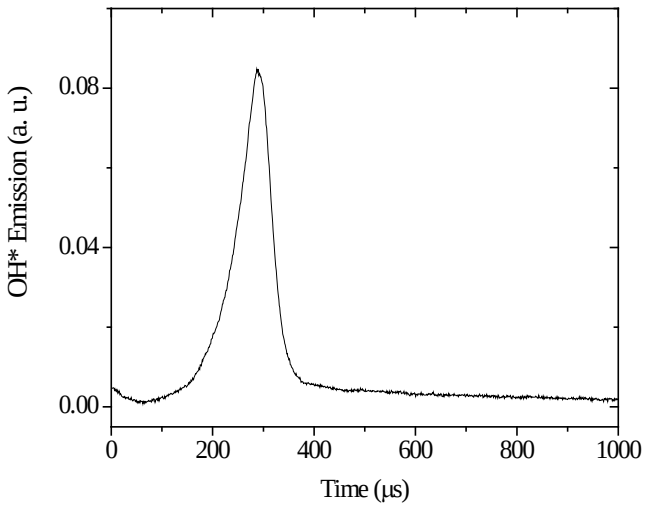

1410: T = 1519 K, P = 1.53 atm, $\tau_{Ignition}$ = 205 μs, $\tau_{Peak - Ignition}$ = 130 μs.

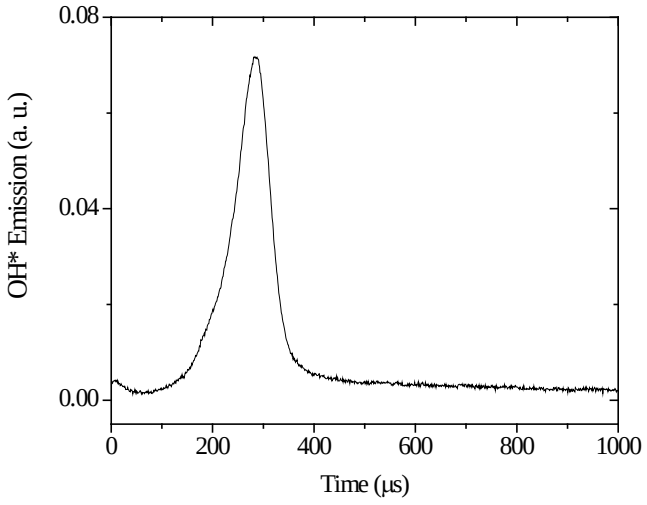

1432: T = 1485 K, P = 1.54 atm, $\tau_{Ignition}$ = 195 μs, $\tau_{Peak - Ignition}$ = 136 μs.

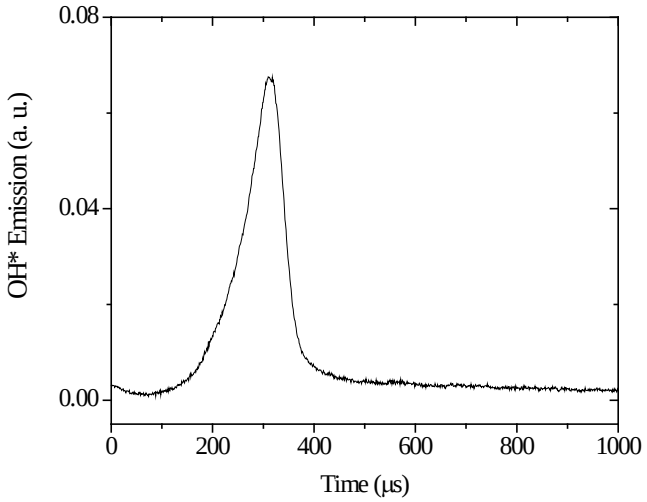

1433: T = 1457 K, P = 1.56 atm, $\tau_{Ignition}$ = 208 μs, $\tau_{Peak-Ignition}$ = 152 μs.

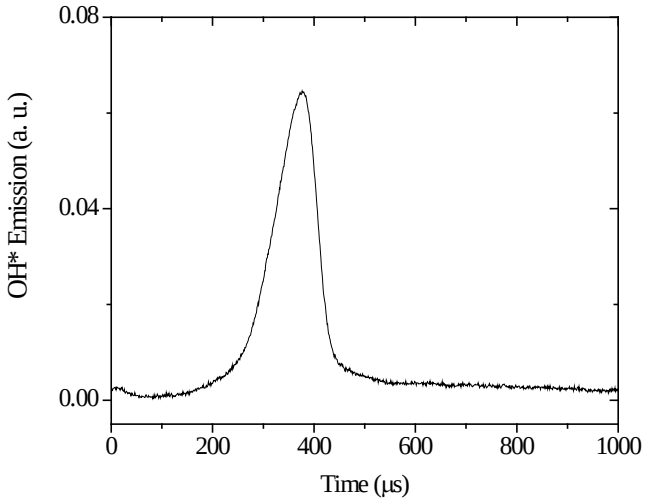

1434: T = 1470 K, P = 1.49 atm, $\tau_{Ignition}$ = 254 μs, $\tau_{Peak-Ignition}$ = 168 μs.

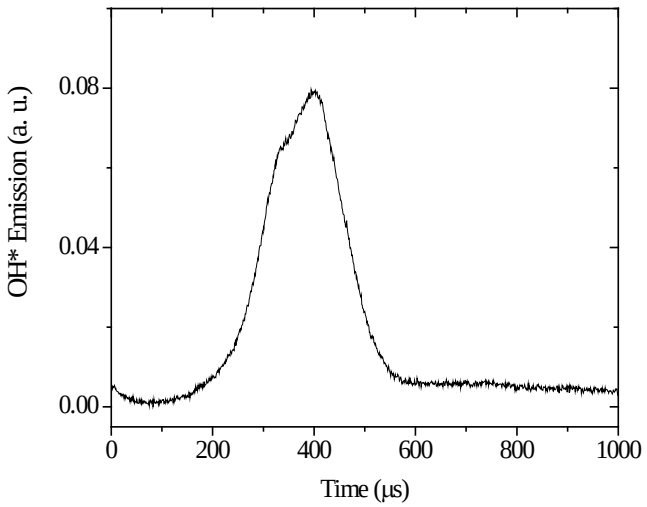

1435: T = 1462 K, P = 1.45 atm, $\tau_{Ignition}$ = 228 μs, $\tau_{Peak - Ignition}$ = 218 μs.

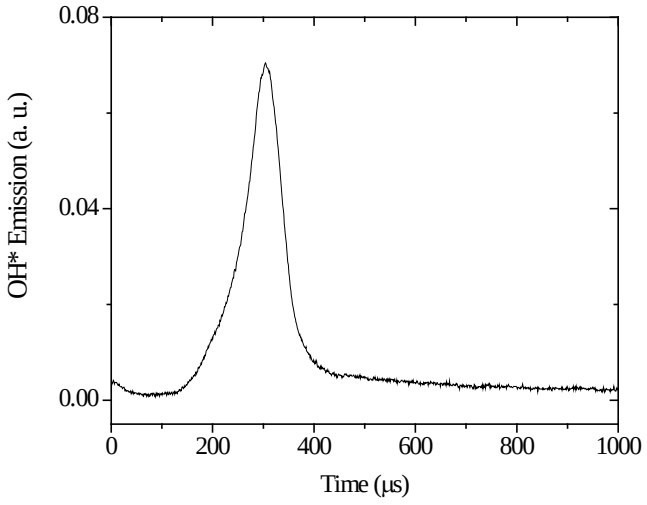

1436: T = 1487 K, P = 1.53 atm, $\tau_{Ignition}$ = 218 μs, $\tau_{Peak - Ignition}$ = 132 μs.

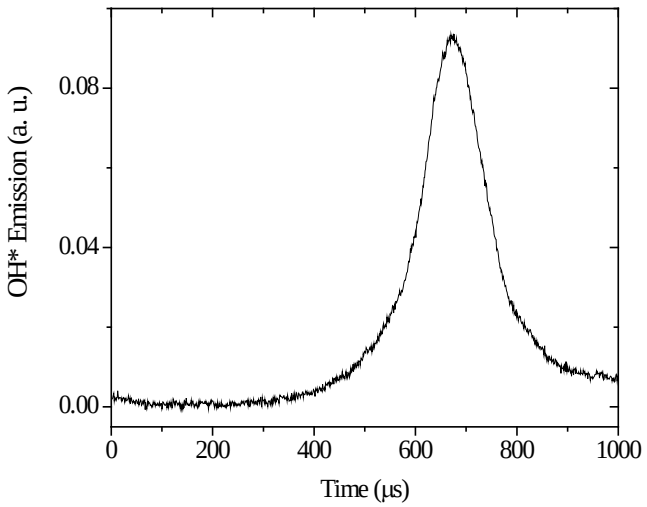

1437: T = 1412 K, P = 1.51 atm, $\tau_{Ignition}$ = 550 μs, $\tau_{Peak-Ignition}$ = 169 μs.

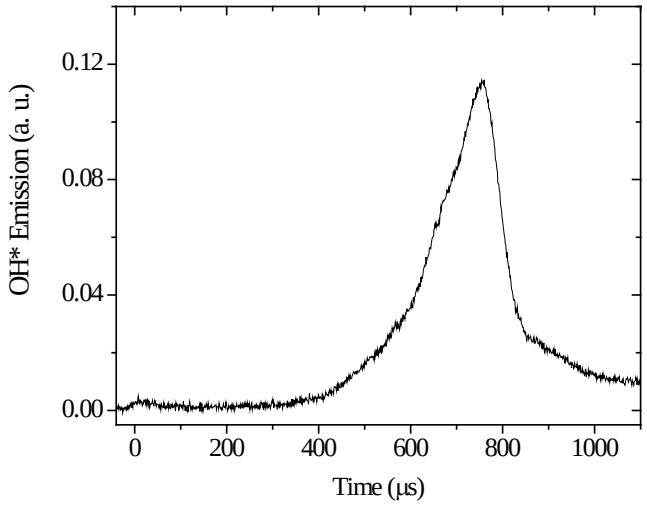

1438: T = 1409 K, P = 1.51 atm, $\tau_{Ignition}$ = 539 μs, $\tau_{Peak-Ignition}$ = 258 μs.

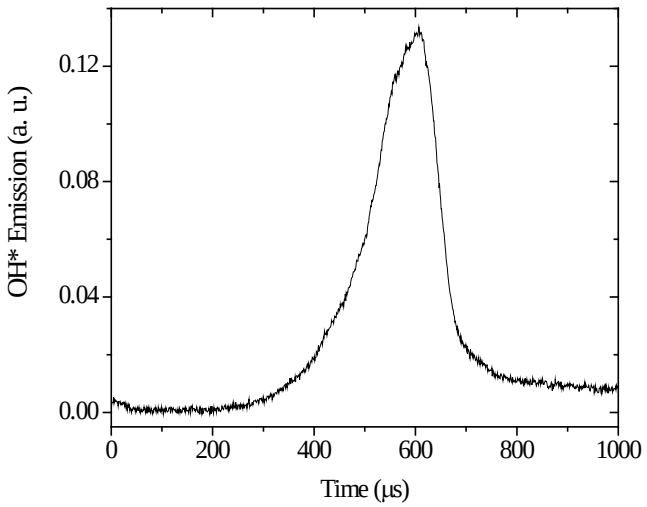

1439: T = 1443 K, P = 1.54 atm, $\tau_{Ignition}$ = 439 μs, $\tau_{Peak-Ignition}$ = 212 μs.

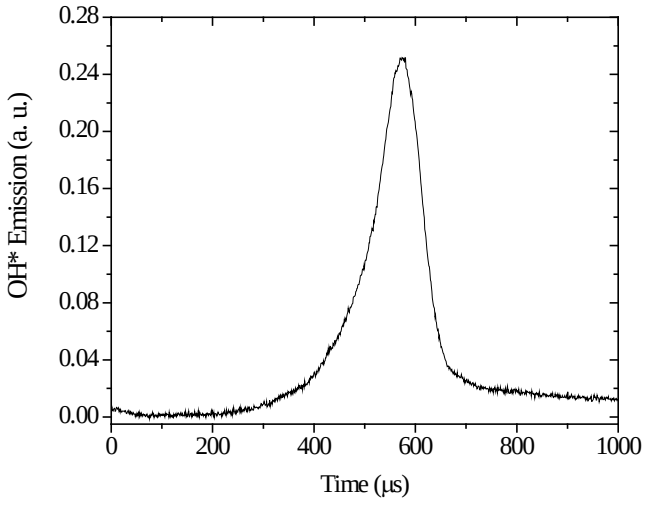

1440: T = 1434 K, P = 1.53 atm, $\tau_{Ignition}$ = 458 μs, $\tau_{Peak-Ignition}$ = 160 μs.

Fuel-Rich (ϕ = 2.0) Profiles

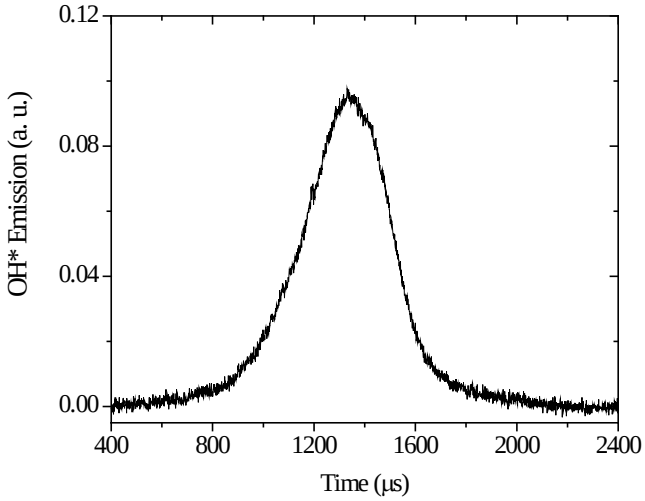

1423: T = 1412 K, P = 1.50 atm, $\tau_{Ignition}$ = 964 μs, $\tau_{Peak - Ignition}$ = 422 μs.

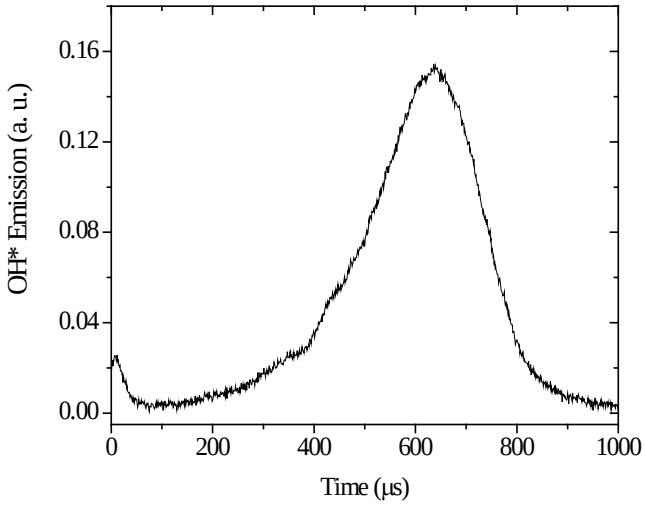

1424: T = 1521 K, P = 1.49 atm, $\tau_{Ignition}$ = 383 μs, $\tau_{Peak - Ignition}$ = 298 μs.

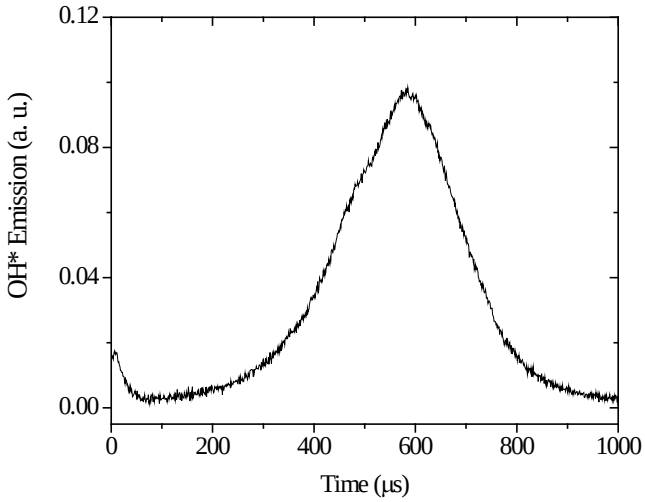

1425: T = 1510 K, P = 1.43 atm, $\tau_{Ignition}$ = 306 μs, $\tau_{Peak - Ignition}$ = 321 μs.

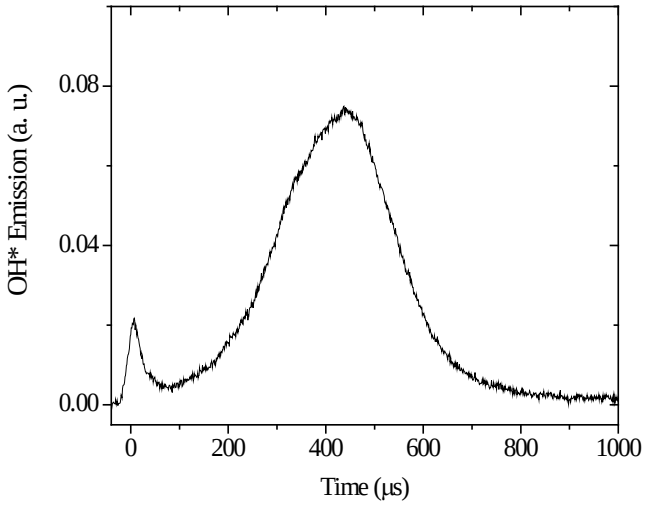

1426: T = 1555 K, P = 1.53 atm, $\tau_{Ignition}$ = 181 μs, $\tau_{Peak - Ignition}$ = 301 μs.

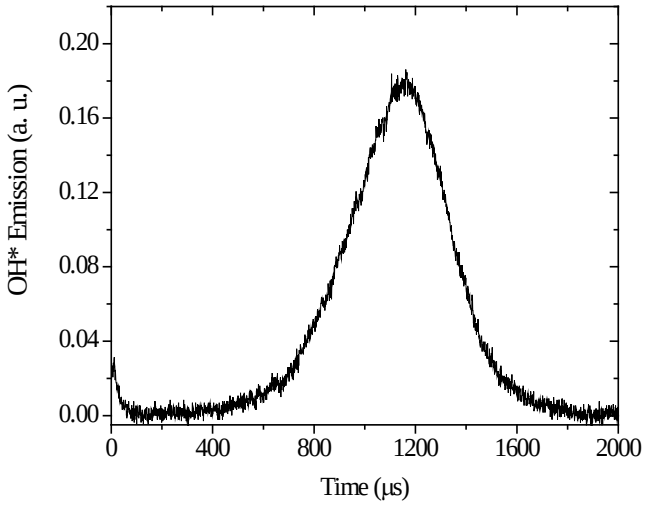

1427: T = 1460 K, P = 1.49 atm, $\tau_{Ignition}$ = 707 μs, $\tau_{Peak-Ignition}$ = 494 μs.

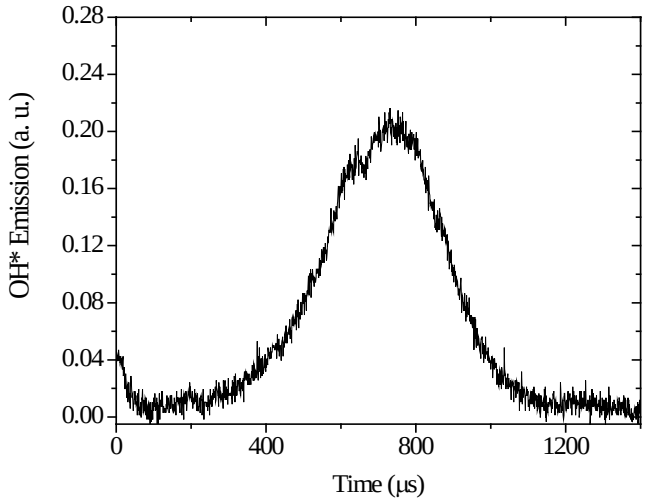

1428: T = 1508 K, P = 1.47 atm, $\tau_{Ignition}$ = 403 μs, $\tau_{Peak-Ignition}$ = 370 μs.

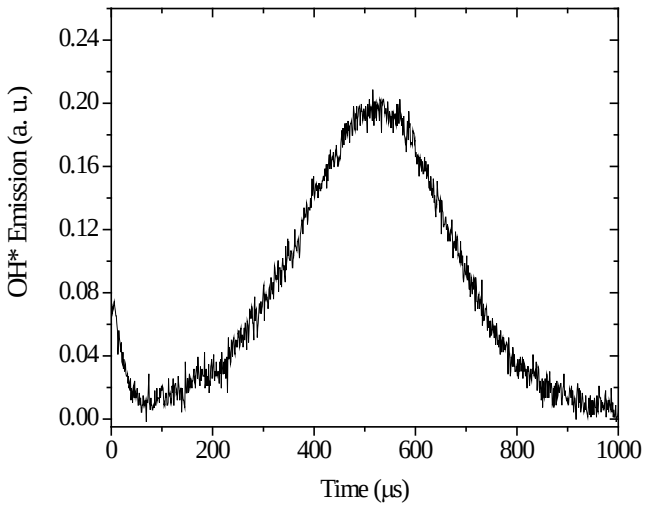

1429: T = 1543 K, P = 1.46 atm, $\tau_{Ignition}$ = 195 μs, $\tau_{Peak-Ignition}$ = 371 μs.

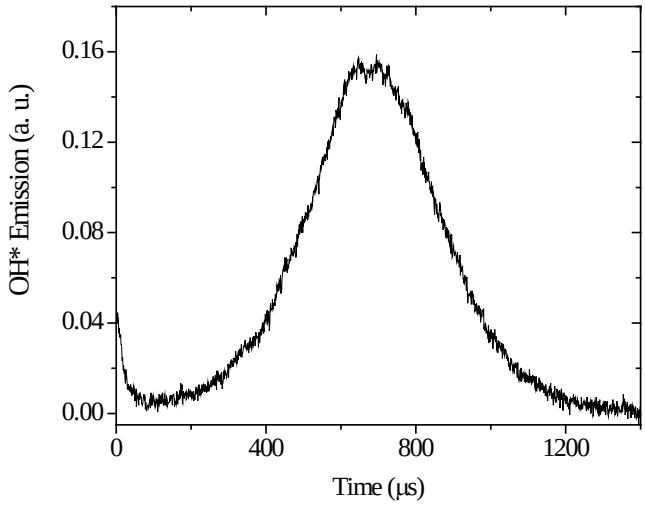

1430: T = 1515 K, P = 1.52 atm, $\tau_{Ignition}$ = 333 μs, $\tau_{Peak-Ignition}$ = 363 μs.

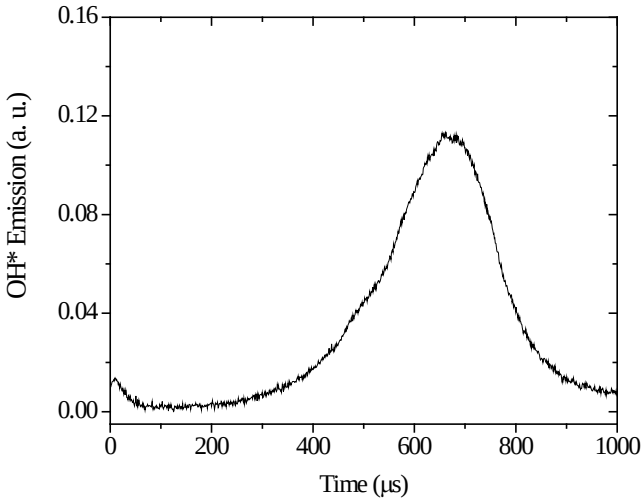

1464: T = 1462 K, P = 1.47 atm, $\tau_{Ignition}$ = 441 μs, $\tau_{Peak-Ignition}$ = 267 μs.

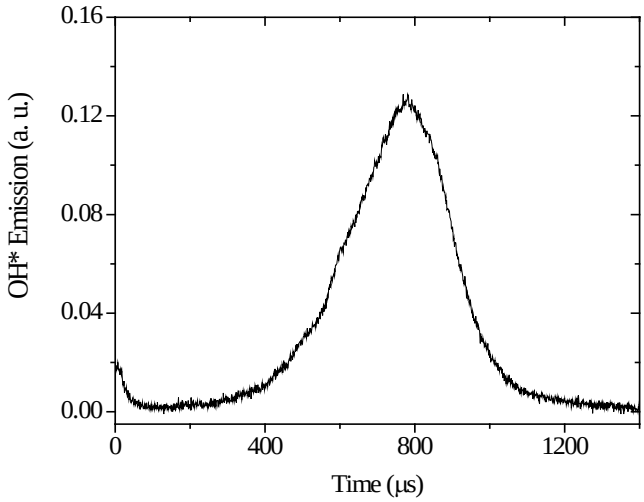

1465: T = 1477 K, P = 1.49 atm, $\tau_{Ignition}$ = 490 μs, $\tau_{Peak-Ignition}$ = 331 μs.

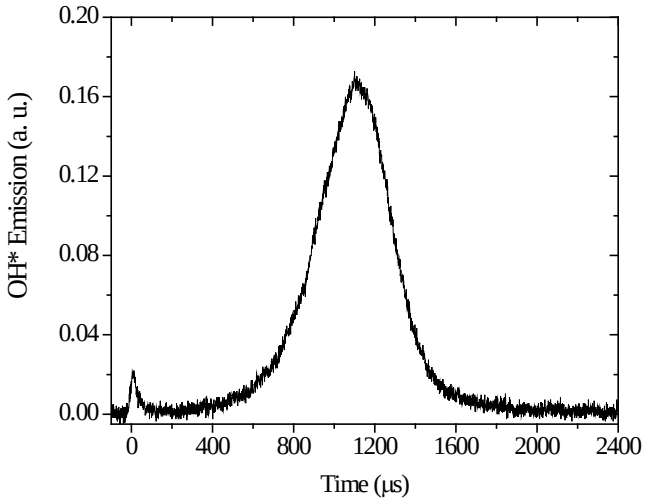

1466: T = 1443 K, P = 1.43 atm, $\tau_{Ignition}$ = 761 μs, $\tau_{Peak-Ignition}$ = 393 μs.

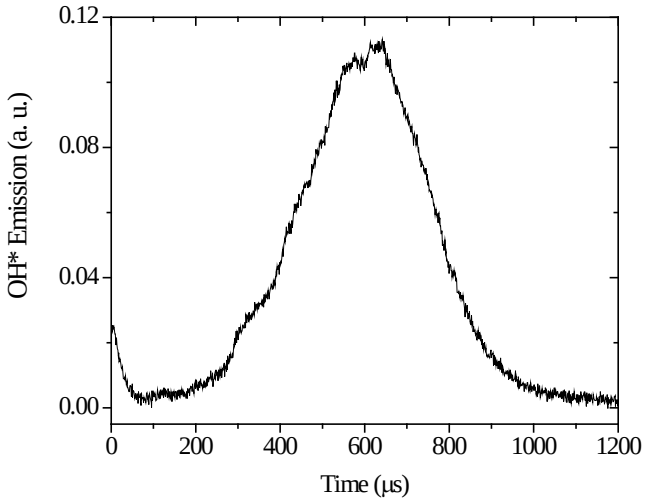

1467: T = 1523 K, P = 1.43 atm, $\tau_{Ignition}$ = 296 μs, $\tau_{Peak-Ignition}$ = 363 μs.

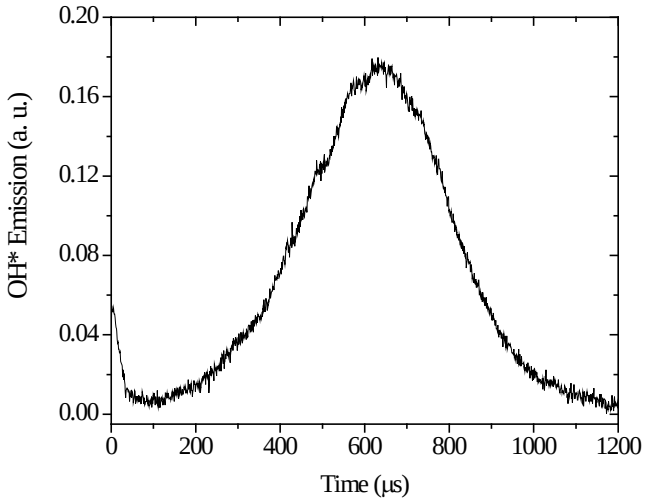

1468: T = 1529 K, P = 1.44 atm, $\tau_{Ignition}$ = 280 μs, $\tau_{Peak - Ignition}$ = 403 μs.

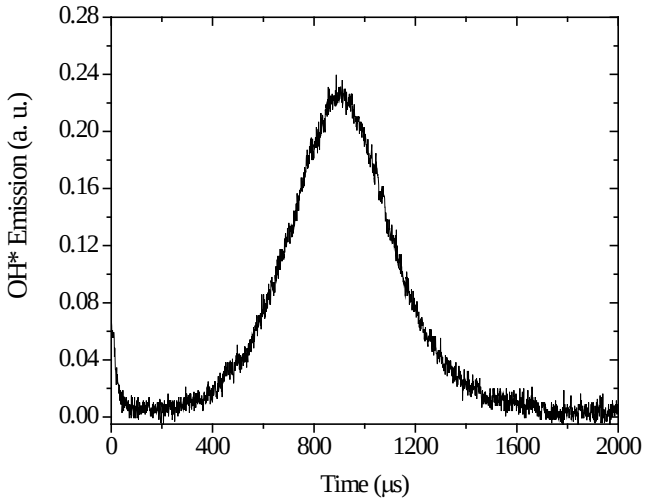

1470: T = 1454 K, P = 1.47 atm, $\tau_{Ignition}$ = 800 μs, $\tau_{Peak - Ignition}$ = 145 μs.

APPENDIX E

CALCULATIONS ON PRE-IGNITION OH* PHENOMENA

Table E–1: Pre-Ignition Peak Calculations

Run	Temperature (K)	Pressure (atm)	Signal%$_{OH^*, t = 1\ ms}$
1452	1478	1.54	2.2
1456	1458	1.51	3.2
1457	1457	1.51	3.8
1454	1425	1.49	2.8
1453	1420	1.48	3.4
1420	1411	1.53	5.6
1418	1403	1.52	12.2
1449	1400	1.48	8.1
1421	1399	1.49	3.5
1419	1391	1.54	1.9
1442	1391	1.50	7.0
1450	1381	1.63	4.4
1422	1366	1.63	3.8
1446	1360	1.62	4.1
1414	1352	1.49	8.0
1415	1351	1.60	13.3
1451	1349	1.58	6.0
1445	1349	1.60	4.7
1448	1346	1.59	6.1
1447	1345	1.59	5.0
1444	1343	1.58	6.7

APPENDIX F

PERCENT TRANSMISSION CURVES FOR OPTICAL FILTERS

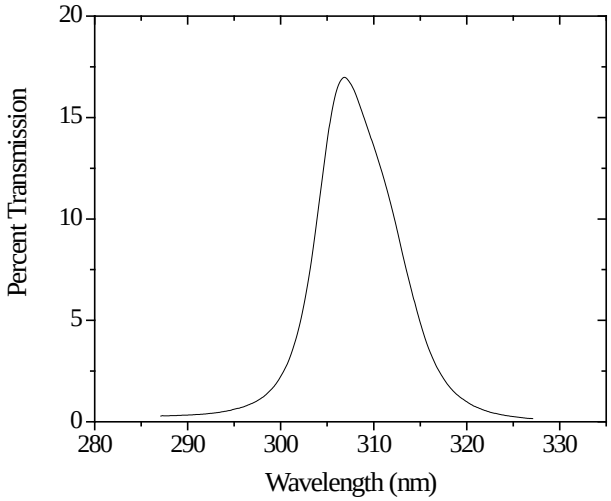

Transmission profile for optical filter used to measure OH* species (Andover Corporation).

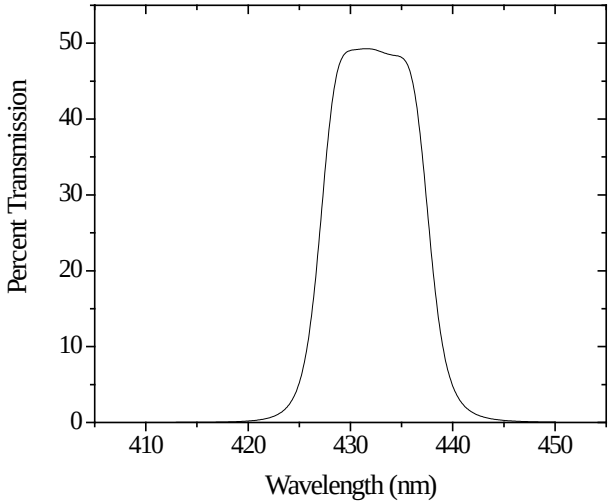

Transmission profile for optical filter used to measure CH* species (Andover Corporation).

VITA

Name: Brandon Michael Rotavera

Address: 3123 TAMU | Department of Mechanical Engineering | College Station, TX 77840

Email: Rotavera@tamu.edu

Educational Background:

M.S., Mechanical Engineering, Texas A&M University, 2009

B.S., Mechanical Engineering, University of Central Florida, 2006

Experience:

Researcher, Combustion and Chemical Kinetics Group – P.I. Dr. Eric Petersen, Turbomachinery Laboratory, *Texas A&M University*, 2008 – Present.

Visiting Researcher, Institut de Combustion Aérothermique Réactivité et Environnement (ICARE) – P. I. Dr. Philippe Dagaut, *Centre for National Scientific Research (CNRS)*, Orléans, France, 2009.

Researcher, Gas Dynamics Laboratory – P.I. Dr. Eric Petersen, University of Central Florida, 2005 – 2008.

Licensed Engineer in Training (EIT) from Fundamentals of Engineering (FE) Exam, April 2005 (Florida), March 2009 (Texas).

Selected Publications:

1. **Rotavera, B.**, Dievart, P., Togbé, C., Dagaut, P., and Petersen, E. L., "Kinetics of n-Nonane Combustion: Measurements and Modeling of Radical-Species Time-Histories and Product Concentrations," *In preparation for submission to the 32nd International Symposium on Combustion*.

2. **Rotavera, B.**, Polley, N., Petersen, E. L., Scheu, K., Crofton, M., and Bourque, G., "Ignition and Combustion of Heavy Hydrocarbons using an Aerosol Shock-Tube Approach," *In preparation for submission to the 2010 ASME TurboExpo.*

3. **Rotavera, B.**, Kumar, A., Seal, S., and Petersen, E. L., "Effect of Ceria Nanoparticles on Soot Inception and Growth in Toluene-Oxygen-Argon Mixtures," *Proceedings of The Combustion Institute*, Vol. 32, 2009, pp. 811 – 819.

4. **Rotavera, B.**, and Petersen, E., "Atomized Fuel Combustion in the Reflected-Shock Region," *Proceedings of the 26th International Symposium on Shock Waves*, 2007, Göttingen, Germany, pp. 141 – 146.